UNIVERSITÀ
DEGLI STUDI
DI PADOVA

Sede Amministrativa: Università degli Studi di Padova

Centro di Ateneo di Studi e Attività Spaziali ‘‘Giuseppe Colombo’’ (CISAS)

SCUOLA DI DOTTORATO DI RICERCA IN : Scienze Tecnologie e Misure Spaziali
INDIRIZZO: Astronautica e Scienze da Satellite
CICLO XXVI

Impact Behaviour of Multifunctional Panels: Experiments and Simulations

Direttore della Scuola: Ch.mo Prof. Giampiero Naletto
Coordinatore d’indirizzo: Ch.mo Prof. Giampiero Naletto
Supervisore: Ch.mo Prof. Ugo Galvanetto
Co-Supervisore: Ch.mo Prof. Alessandro Francesconi

Dottorando : Teo Mudrić

Summary

The objective of this study was to investigate a multifunctional system under high- to hyper-velocity impact loading. This multifunctional system is a plate structure that, in addition to its load bearing function, has the ability of self-repairing holes generated by impacts. In order to achieve multiple functionality the panel consists of several different layers, each having a specific task, and thus primary contributing to a specific function of the entire multifunctional structure system. From a structural point of view this multifunctional system can be considered as a multilayer plate. From a functional perspective the panel layers can be divided in two groups: structural layer and self-healing layer. Each layer can occur once or more in a panel configuration. The performance of the multifunctional structure depends on the number of layers, the mechanical and physical properties of the individual layers, layer thickness and on the arrangement of the various layers in a multifunctional structure.

The multifunctional system investigated in this work consists of one self-healing layer and one or two structural layers. To provide the structural system with the ability to seal holes generated by perforating impacts a layer of ethylene-co-methacrylic acid ionomer was used in a multifunctional system. These ionomers have been observed to self-heal following ballistic puncture and such a response is an inherent behaviour of those materials, therefore no external intervention is necessary in the self-healing process. For the structural layers, plates made of composite materials were used. Two slightly different structural layers were investigated. One is a laminate made entirely of carbon fibre reinforced plastics, while the other is a carbon fibre laminate with aramid fabric/epoxy resin composite layers attached to its front and back face. These two structural layers and the ionomer layer were combined to form several configurations of multifunctional panels. The different configurations, including also the individual layers alone, were tested under impact loading.

Tests on the ionomer alone were performed to study its protection capability for bumper applications. For this purpose tests on aluminium plates were also performed and the results were compared to those of the ionomer. The protection capability was evaluated by studying the damage on witness plates and the momentum transferred to them.

The composite structural layers for the multifunctional structure were tested individually and their behaviour was compared with that of the ionomer self-healing layer. Multifunctional panel configurations consisting of two and three layers were also tested. The impact behaviour and the comparison of the various configurations were characterized through the momentum transfer to the witness plate, the fragments velocities in the debris cloud, the damage in the layers, in certain cases the damage on the witness plate was also used. Several instruments were used to measure the

relevant quantities. A ballistic pendulum was used to estimate the momentum of the debris cloud. A high-speed video camera was employed to film the impact tests, which enabled the measurement of fragments velocities by a dedicated software. An ultrasound flaw detector was applied for delamination damage detection in the composite material. Superficial damage was inspected visually. Learning how to use the ultrasound flaw detector and the high-speed video camera was an integral part of the PhD work that required a considerable amount of time.

The self-healing of the ionomer was checked for all tests by visually examining the ionomer samples.

The experiments were conducted at the CISAS impact facility, using a two stage light gas gun. The impact velocities in the experimental tests ranged from ~1.0 to ~4.0 km/s. Aluminium spherical projectiles were used, and ranged in diameter from 1.5 to 5.6 mm.

Numerical simulations of the experimental tests on the individual layers were performed and the results were compared. The numerical simulations were performed with the commercially available 'hydrocode' Ansys Autodyn.

Sommario

L'obiettivo di questa tesi era di studiare un sistema multifunzionale soggetto a impatti ad alta- e iper-velocità. Questo sistema multifunzionale è un pannello che, oltre alla sua funzione portante, ha la capacità di autoripararsi cioè di chiudere i fori causati da impatti. Al fine di ottenere la multifunzionalità il pannello è costituito da diversi strati, ciascuno avente un compito specifico, contribuendo così ad una funzione specifica dell'intero sistema struttura multifunzionale. Dal punto di vista strutturale questo sistema multifunzionale può essere considerato come una piastra multistrato. Dal punto di vista funzionale gli strati del pannello possono essere suddivisi in due gruppi: strato strutturale e strato auto-riparante. Ogni strato può essere presente una o più volte nella configurazione del pannello. Le prestazioni della struttura multifunzionale dipendono dal numero di strati, dalle proprietà meccaniche e fisiche degli strati individuali, dallo spessore degli strati e della disposizione dei vari strati nella struttura multifunzionale.

Il sistema multifunzionale studiato in questo lavoro è costituito da un strato auto-riparante e uno o due strati strutturali. Per fornire al sistema strutturale la capacità di richiudere i fori generati da impatti perforanti, uno strato di ionomero con capacità auto-riparanti è stato applicato nel sistema multifunzionale. Si è osservato che questi ionomeri sono in grado di richiudere i fori causati da impatti balistici. Inoltre questa proprietà è un comportamento intrinseco di questi materiali, quindi non è necessario un intervento esterno nel processo di auto-riparazione. Per gli strati strutturali, sono state usate lastre in materiale composito. Due strati strutturali leggermente diversi sono stati studiati. Uno è un laminato realizzato interamente in fibra di carbonio e resina, mentre l'altro è un laminato misto con due strati di fibra aramidica in resina epossidica sulle superfici estreme e una parte centrale in laminato di fibre di carbonio. Questi due strati strutturali e lo strato di ionomero sono stati combinati tra di loro per formare diverse configurazioni di pannelli multifunzionali. Le diverse configurazioni, tra cui gli strati singoli, sono stati testati in casi di impatto.

Prove sul solo ionomero sono state eseguite per studiare la sua capacità di protezione nei confronti di impatti. Per questo scopo anche dei test d’impatto su lastre di alluminio sono stati effetuati e i risultati sono stati confrontati con quelli dello ionomero. La capacità di protezione è stata valutata attraverso lo studio del danno su witness plates e la quantità di moto ad esse trasferita.

Gli strati strutturali in materiale composito per la struttura multifunzionale sono stati testati singolarmente e i relativi risultati sono stati confrontati tra loro e con quelli dello strato auto-riparante in ionomero. Inoltre si sono testate e valutate configurazioni di pannelli multifunzionali composte anche da due o tre strati. Il comportamento sotto impatto e il confronto delle configurazioni è stato caratterizzato attraverso:

- la valutazione del trasferimento della quantità di moto alla witness plate,
- la velocità dei frammenti nella nuvola di detriti,
- il danno negli strati e, in certi casi, il danno sulla witness plate.

Diversi strumenti sono stati utilizzati per misurare tali quantità:

- un pendolo balistico per stimare la quantità di moto della nube di detriti;
- una videocamera ad alta velocità per filmare le prove d'impatto, il che ha consentito la misurazione della velocità dei frammenti;
- un rilevatore di difetti ad ultrasuoni per il rilevamento della delaminazione nel materiale composito.

Il danno superficiale è stato ispezionato visivamente così come l'auto-riparazione dello ionomero che è stata valutata per tutti i test esaminando visivamente i campioni di ionomero.

L'apprendimento dell'utilizzo di strumenti sofisticati quali il rivelatore ad ultrasuoni e la videocamera ad alta velocità è stata parte integrante del lavoro di dottorato che ha richiesto una considerevole quantità di tempo.

Gli esperimenti sono stati condotti presso il laboratorio di impatti del CISAS, utilizzando il cannone a doppio stadio e a gas leggero. Le velocità d'impatto nelle prove sperimentali variavano fra ~ 1.0 e ~ 4.0 km/s. Sono state utilizzate come proiettili delle sfere in alluminio, il cui diametro variava fra 1.5 mm e 5.6 mm.

Infine sono state effettuate delle simulazioni numeriche delle prove sperimentali sui singoli strati ed i risultati sono stati confrontati con quelli sperimentali. Le simulazioni numeriche sono state effettuate utilizzando l'hydrocode commerciale Ansys AUTODYN.

Acknowledgements

I would like to express my sincere gratitude to my supervisor Professor Ugo Galvanetto for giving me the opportunity to do this research, as well as for his supervision, guidance and support during my research. It was a pleasure to work with him and to know him as a person.

I am deeply grateful to my co-supervisor Professor Alessandro Francesconi for his support, suggestions and advices for my PhD study, which I've always found very useful and precise.

Special thanks to Dr. Cinzia Giacomuzzo for her numerous advices and for all the useful constant discussions on the encountered problems in my research, which helped me a lot to carry on my research work. I thank her also for helping me in the process of learning how to use the ultrasound flaw detector.

I am very grateful to Professor Gordan Jelenić for putting me in contact with Professor Ugo Galvanetto.

I would like to acknowledge Dr. Mirco Zaccariotto for managing the acquisition of the damage detection instrument and organising the courses for its application.

I would like to thank Francesco Babolin for the help during experimental set-up mounting.

I would like to thank all my colleagues Marco, Daniele, Giuseppe, Riccardo, Alessandro, Nicolò, Gianluca, Giovanna, Beatrice, Mattia and Marco, for filling the everyday work atmosphere with more joy.

Above all, I would like to thank my mother, father and brother for their endless love, support, encouragement and advices throughout my entire life.

Table of Contents

List of figures

List of tables

1. Introduction

1.1. Introduction and motivation

This thesis was part of a research project called IMBEMUS (IMpact BEhaviour of MUltifunctional materialS). IMBEMUS was started by a group of researchers at the University of Padua in Italy. The aim of IMBEMUS was to develop a multifunctional panel that is able to perform the following tasks: a) act as a load bearing structure, b) repair holes generated by impacts, and c) detect perforation of the panel and its location. This would lead to a structural element with the addition of two more functions: sealing of holes caused by impacts and monitoring the occurrence of impact perforation. Such a panel falls in the category of multifunctional systems. Namely, multifunctional materials systems can perform more than one function simultaneously or sequentially in time and seek to achieve overall system performance enhancement. The objective of this thesis was to study the impact behaviour of a multifunctional system having a structural and self-healing function. Therefore, the sensor layer was not the object of the present study. Several multifunctional panels configurations were tested experimentally under high- and hyper-velocity impacts in order to characterize their impact behaviour. Numerical simulations of several tests were also carried out.

In aerospace and military engineering one of the most critical issues is represented by high and hyper velocity impacts, due to meteoroids or space debris in the first case and to projectiles or ejecta in the second case. Impacts of micrometeoroids and space debris on vehicles moving in space are a recognized threat to space missions. The consequences of meteoroid and debris impacts on a spacecraft can vary widely, from small surface indentation to clear hole perforations that can lead to the penetration of the impacting object in a spacecraft. Close to the earth surface, where much man-made debris is present, the probability of impacts with debris is particularly high. Even if the structural integrity is not fully compromised clear hole penetrations could be extremely damaging if they affect tanks containing gases which are necessary to complete long lasting missions, even more so when human beings are on board. Therefore there is the clear need of self-healing materials capable of immediately closing holes generated by impacts. In general, systems capable to close holes generated by impacts could find large applications for anti-leakage purposes in environments where leakage could occur due to an impact event that would perforate the structural element. Since the aerospace and military field are two examples of environments where perforating impacts represent a possible loading condition, a structural element with the ability to close holes generated by an impact could be applied in those two fields primary to fuel storage tanks of airplanes and ground vehicles, where even a small perforation can have catastrophic consequences due to leakage of the fuel.

1.2. Organization of the thesis

This thesis is organized in six chapters. After the present first chapter which gives a brief introduction and motivation for this research, in chapter two the basic theory of stress waves propagation in solids is presented. In chapter three the multifunctional panel structure is described in detail. Both the structural and self-healing layers are described. The configurations consisting of a self-healing and/or structural layers which were experimentally tested are given. The experimental investigation and results are described in chapter four. The chapter begins with an overview of the used instrumentation and then details about the experimental set-up are provided. This is followed by a presentation and discussion of the experimental results. In chapter five the numerical approach and models are described. Further, the obtained results are compared with the experimental ones. In chapter six the conclusions derived from this work are summarized.

2. Wave propagation in solids

In high- to hyper-velocity impacts (0.5 – 3 km/s) a high intensity load is generated in the impact area during a short time interval (on the order of microseconds). In such situation the response becomes highly localized and affected by the material behaviour in the vicinity of load application. A description of the phenomena in terms of wave propagation is appropriate. The influence of velocity, geometry, material constitution, strain rate, localized plastic flow, and failure are manifest at various stages of the impact process [1].

The theory of waves is treated in [[1]-[6]]. In this chapter a basic presentation of elastic and shock waves in solids is given.

2.1. Elastic waves

Let's consider a situation depicted in Figure 2.1, in which a bar impacting a long cylindrical bar is shown.

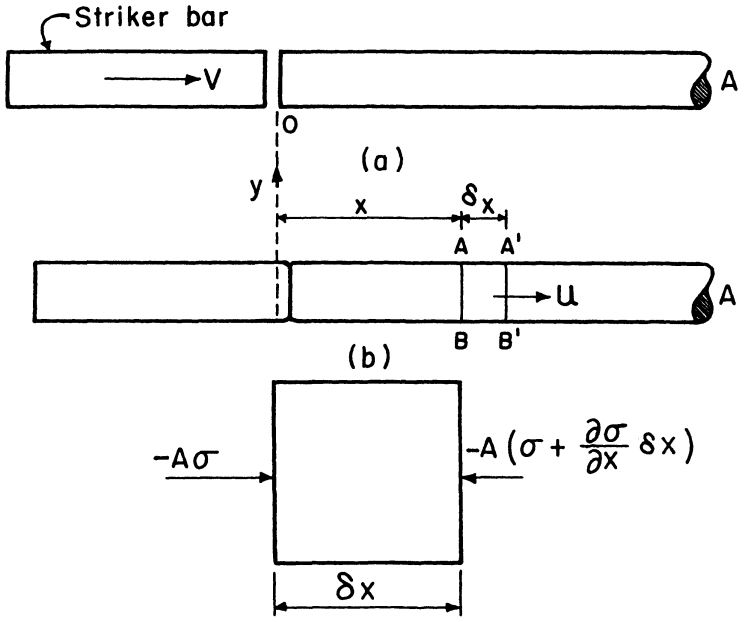

Figure 2.1 Wave propagation in a bar, (a) prior to impact and (b) after impact [5].

Upon impact a compressive stress wave is generated that propagates in the impacting bars. If we limit the analysis to one-dimensional wave propagation (therefore neglecting the strains and inertia along the direction transverse to the bar) and by applying Newton's second law to *AA'B'B* we obtain:

$$F = ma \tag{2.1}$$

$$-\left[A\sigma - A\left(\sigma + \frac{\partial \sigma}{\partial x}\delta x \right) \right] = A\rho\delta x \frac{\partial^2 u}{\partial t^2} \tag{2.2}$$

$$\frac{\partial \sigma}{\partial x} = \rho \frac{\partial^2 u}{\partial t^2} \tag{2.3}$$

Where σ is the stress in the impacted bar, and ρ is the density of the bar's material. Replacing the stresses with the strains (ε) through the application of Hooke's law:

$$\sigma = E\varepsilon \tag{2.4}$$

Where E is Young's modulus, and the strain ε is defined as:

$$\varepsilon = \frac{\partial u}{\partial x} \tag{2.5}$$

We obtain the differential equation describing the wave (wave equation) for a one-dimensional case

$$\frac{\partial^2 u}{\partial t^2} = \frac{E}{\rho}\frac{\partial^2 u}{\partial x^2} \tag{2.6}$$

The velocity of this wave is given as

$$C_0 = \sqrt{\frac{E}{\rho}} \tag{2.7}$$

A general form of the equation of wave motion is given as:

$$\frac{\partial^2 \psi}{\partial t^2} = c^2 \frac{\partial^2 \psi}{\partial x_i \partial x_i} \tag{2.8}$$

In the above equation the indicial notation has been used, therefore when a subscript is repeated in the same term it denotes that summation with respect to this subscript occurs. In equation (2.8) $\psi(x_i,t)$ is the dependent variable and is a measure of some property of the disturbance such as displacement or velocity and c is a physical constant.

For example, the wave equation for a dilatation Δ ($\Delta=\varepsilon_{11}+\varepsilon_{22}+\varepsilon_{33}$) propagating in an elastic isotropic unbounded medium is:

$$\rho \frac{\partial^2 \Delta}{\partial t^2} = (\lambda + 2\mu) \frac{\partial^2 \Delta}{\partial x_i \partial x_i} \tag{2.9}$$

Where λ and μ are the Lame constants, and i takes on the value *1*, *2* and *3*. Equation (2.9) is known as the longitudinal wave equation. The velocity of propagation of the dilatation is:

$$V = \left(\frac{\lambda + 2\mu}{\rho} \right)^{1/2} \tag{2.10}$$

This velocity is also called ‘‘bulk sound speed’’.

The general solution of the one-dimensional wave equation (2.6) is [[5],[7]]:

$$u(x,t) = F(x - C_0 t) + G(x + C_0 t) \tag{2.11}$$

Where F and G are arbitrary functions of the arguments (x-C_0t) and (x+C_0t) respectively. In (2.11) F represents a wave moving in the positive direction along the x axis, while function G represents a wave propagating in the negative direction of the x axis, as shown in Figure 2.2. The shapes of these waves are unchanged with time and propagate at a constant velocity C_0. Therefore, the physical meaning of equation (2.11) is that we have two waves propagating at constant velocity along the x axis, and one of the two waves is travelling in the positive direction, while the other is moving in the negative direction.

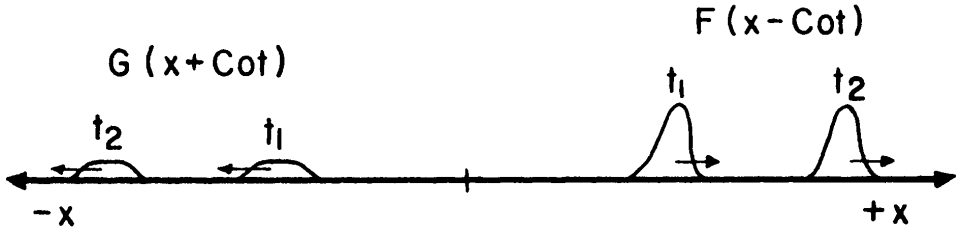

Figure 2.2 General solution for wave equation in uniaxial stress [5].

When a disturbance propagates in a material it causes motion of the material points as it passes across them. The velocity with which a point in the material moves as the wave moves across it is called the particle velocity (U_p).

Depending on the boundary conditions and on the relation of particles motion to the wave direction of propagation, various wave types can propagate in solids. The most common types of elastic waves in solids are [5]:

1. Longitudinal (or irrotational) waves; in infinite and semi-infinite media they are known as ‘‘dilatational’’ waves. In these waves the particles are moving along the direction normal to the wave front (i.e. parallel to the direction of propagation of the wave). For a compressive wave, the particle and wave motion have the same sense, and for a tensile wave, they have opposite senses.
2. Distortional (shear, transverse, equivoluminal) waves. In distortional waves the material particles are moving in the direction perpendicular to the direction of propagation of the wave. The density of the material remains unchanged, and all longitudinal strains (ε_{11}, ε_{22}, ε_{33}) are zero.
3. Surface (Rayleigh) waves. In these waves the particles move along elliptical trajectories. This type of waves is restricted to the region adjacent to the surface, and they decay exponentially with depth from the surface to the medium interior.
4. Interfacial (Stoneley) waves. When two semi-infinite media with different properties are in contact, special waves form at their interface [5].
5. Waves in layered media (Love waves). This is another type of surface wave confined to a relatively shallow surface zone. Love waves can emerge in a situation where layers of materials with different properties lay on each other.
6. Bending (flexural) waves (in bars and plates). The propagation of flexure in a one dimensional (bar) or two dimensional configuration is referred to as a bending wave.

2.1.2. Intensity of the propagated stress

The relationship between the longitudinal stress (σ) in a body and the longitudinal particle velocity can be obtained from Newton’s second law:

$$Fdt = d\left(mU_p\right) \tag{2.12}$$

where F is the longitudinal force acting on a given cross section, dt is the time the force acts, m is the mass it acts against, and U_p is the velocity imparted to m by F. The stress and mass can be expressed as:

$$\sigma = \frac{F}{A} \tag{2.13}$$

$$m = \rho A dx \tag{2.14}$$

Where A is the cross section on which the force F acts, ρ is the material density, and dx is the distance the pulse has moved in time dt. Inserting these equations in (2.12) we obtain:

$$\sigma A dt = \rho A dx dU_p \tag{2.15}$$

$$\sigma = \rho \frac{dx}{dt} dU_p \tag{2.16}$$

Since dx/dt is the propagation velocity of the pulse C, we obtain the following equation for the longitudinal stress:

$$\sigma = \rho C\left(\Delta U_p\right) \tag{2.17}$$

where ΔU_P is the change in particle velocity.

2.1.3. Wave reflection and transmission at a boundary

When a wave encounters a boundary between two media with different sonic impedance, it will reflect and refract (transmit), see Figure 2.3. The sonic impedance of a medium is defined as the product of the medium density by its sound wave velocity.

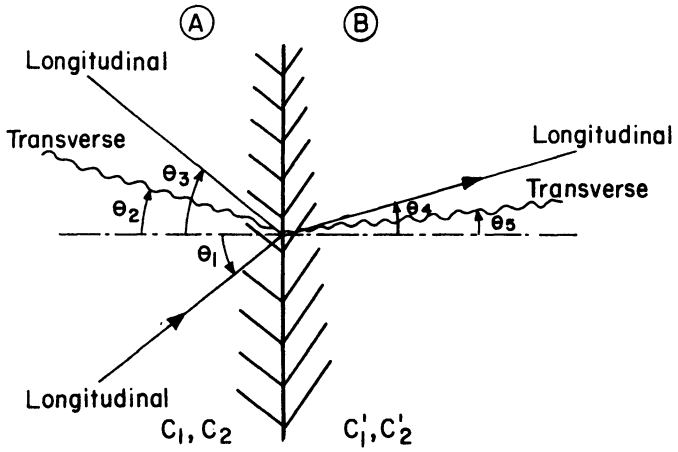

Figure 2.3 Longitudinal elastic wave encounter with a boundary between media A and B [5].

In Figure 2.3 a longitudinal wave hitting a boundary between media *A* and *B* is shown. As can be seen, it reflects and refracts as a longitudinal wave, and also two transverse waves are generated at the interface. The reflection and refraction angles shown in Figure 2.3 are given by the following relationship:

$$\frac{\sin\theta_1}{C_1} = \frac{\sin\theta_2}{C_2} = \frac{\sin\theta_3}{C_1} = \frac{\sin\theta_4}{C_1'} = \frac{\sin\theta_5}{C_2'} \tag{2.18}$$

where C_1 and C_2 are the longitudinal and shear wave velocity in medium *A*, C_1' and C_2' are the longitudinal and shear velocity in medium *B*.

2.1.3.1. Bar with a continuous cross section

In Figure 2.4 a longitudinal wave is propagating from left to right in a bar, and strikes normally on a boundary *A-B* between medium *A* and medium *B*. Before it encounters the boundary the wave is moving in bar *A* at velocity C_A. The particle velocity is U_p and the stress is σ. Since the incidence is normal to the boundary, the incident longitudinal wave will transmit (refract) and reflect longitudinal waves (Figure 2.4 (b) and (c)). The forces caused by the incident, reflected and transmitted wave are plotted in Figure 2.4 (b), while the particle velocities for the incident, reflected and transmitted wave are shown in Figure 2.4 (c).

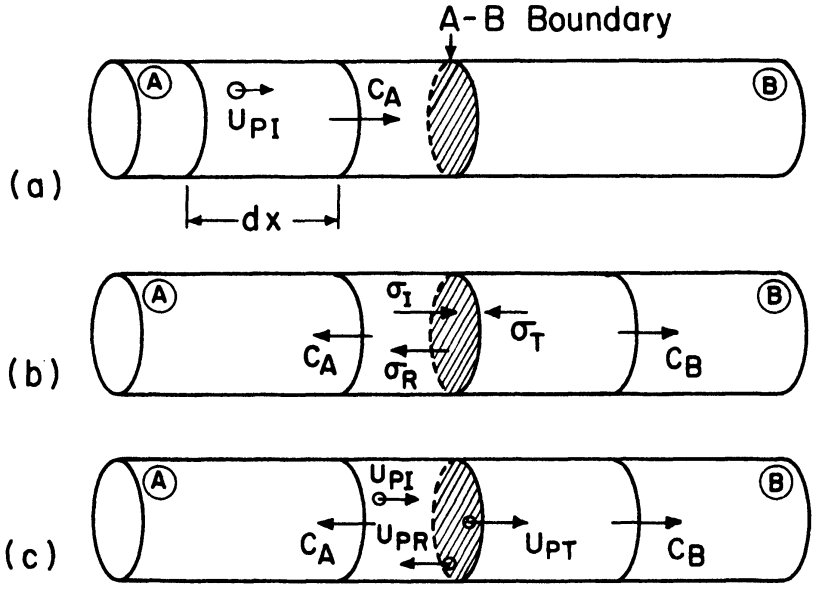

Figure 2.4 Longitudinal wave in a bar striking normally on boundary between media A and B: (a) prior to encounter with boundary, (b) forces exerted on boundary (equilibrium condition), (c) particle velocities (continuity) [5].

The signs of the stress and particle correspond to a situation where medium *A* has a higher impedance than medium *B*. At the interface (boundary *A-B*) two conditions must be fulfilled:

1) The forces in both bars at the interface must be equal (equilibrium)
2) Particle velocities at the interface must be continuous

From condition *1* we have:

$$\sigma_I + \sigma_R = \sigma_T \tag{2.19}$$

Condition *2* gives:

$$U_{pI} + U_{pR} = U_{pT} \tag{2.20}$$

From (2.17) we can express the particle velocities as:

$$U_{pI} = \frac{\sigma_I}{\rho_A C_A} \tag{2.21}$$

$$U_{pT} = \frac{\sigma_T}{\rho_B C_B} \tag{2.22}$$

$$U_{pR} = \frac{-\sigma_R}{\rho_A C_A} \tag{2.23}$$

Substituting these velocities into (2.20) we have:

$$\frac{\sigma_I}{\rho_A C_A} - \frac{\sigma_R}{\rho_A C_A} = \frac{\sigma_T}{\rho_B C_B} \tag{2.24}$$

From equations (2.19) and (2.24) we obtain the following expressions:

$$\frac{\sigma_T}{\sigma_I} = \frac{2\rho_B C_B}{\rho_B C_B + \rho_A C_A} \tag{2.25}$$

$$\frac{\sigma_R}{\sigma_I} = \frac{\rho_B C_B - \rho_A C_A}{\rho_B C_B + \rho_A C_A} \tag{2.26}$$

It can be seen from the above equations that the amplitude of the transmitted and reflected waves depends on the sonic impedance of the materials. We can also see from (2.25) that the ratio σ_T/σ_I cannot be negative, therefore tension will be transmitted as tension and compression as compression. From the ratio σ_R/σ_I in (2.26) we can see that if $\rho_A C_A > \rho_B C_B$ an incident compressional stress will be reflected as a tensile stress and vice versa, while if $\rho_A C_A < \rho_B C_B$ a compressive stress will be reflected as a compressive stress.

Using equations (2.19), (2.21), (2.22), and (2.23) we can arrive at the expressions for the transmitted and reflected particle velocities:

$$\frac{U_{pR}}{U_{pI}} = \frac{\rho_A C_A - \rho_B C_B}{\rho_A C_A + \rho_B C_B} \tag{2.27}$$

$$\frac{U_{pT}}{U_{pI}} = \frac{2\rho_A C_A}{\rho_A C_A + \rho_B C_B} \tag{2.28}$$

The following expressions are obtained for σ_T/σ_I and σ_R/σ_I for the limiting cases when a stress wave encounters a free surface or a rigid boundary:

- for a free surface we have that $\rho_B C_B = 0$, therefore:

$$\frac{\sigma_T}{\sigma_I} = 0$$

$$\frac{\sigma_R}{\sigma_I} = -1$$

- for a rigid boundary ($E = \infty \rightarrow C = \infty$), by rearranging equations (2.25) and (2.26), we obtain:

$$\frac{\sigma_T}{\sigma_I} = \frac{2}{1 + \frac{\rho_A C_A}{\rho_B C_B}} \simeq 2$$

$$\frac{\sigma_R}{\sigma_I} = \frac{1 - \frac{\rho_A C_A}{\rho_B C_B}}{1 + \frac{\rho_A C_A}{\rho_B C_B}} \simeq 1$$

For the particle velocities the following relations are valid:

- free surface:

$$\frac{U_{pT}}{U_{pI}} = 2$$

$$\frac{U_{pR}}{U_{pI}} = 1$$

- rigid boundary:

$$\frac{U_{pT}}{U_{pI}} = 0$$

$$\frac{U_{pR}}{U_{pI}} = \frac{\frac{\rho_A C_A}{\rho_B C_B} - 1}{\frac{\rho_A C_A}{\rho_B C_B} + 1} = -1$$

2.1.3.2. Bar with a discontinuous cross section

A bar with discontinuous cross section made of different materials is shown in Figure 2.5.

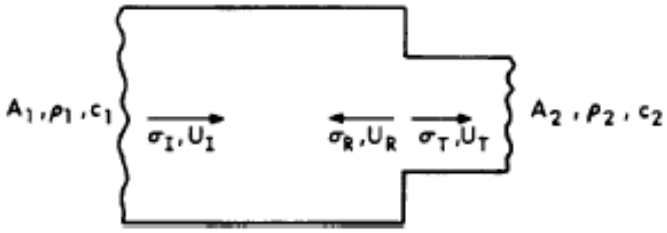

Figure 2.5 Wave reflection and transmission at changes in cross section [1].

Following the same procedure as in section 2.1.3.1., i.e. satisfying the conditions of forces equality in both bars at the interface and continuity of particle velocity at the interface, the following expressions are obtained:

$$\sigma_T = \frac{2A_1\rho_2C_2}{A_1\rho_1C_1 + A_2\rho_2C_2}\sigma_I \tag{2.29}$$

$$\sigma_R = \frac{A_2\rho_2C_2 - A_1\rho_1C_1}{A_1\rho_1C_1 + A_2\rho_2C_2}\sigma_I \tag{2.30}$$

When both bars are made of the same material, then $\rho_1 = \rho_2$ and $C_1 = C_2$, and we have:

$$\sigma_T = \frac{2A_1}{A_1 + A_2}\sigma_I \tag{2.31}$$

$$\sigma_R = \frac{A_2 - A_1}{A_1 + A_2}\sigma_I \tag{2.32}$$

Therefore, when the two materials are equal, if $A_2 > A_1$ then σ_T and σ_R will be of the same type. If $A_2 < A_1$, then σ_T and σ_R will be of opposite sign.

2.2. Shock waves

2.2.1. Uniaxial strain

When the material does not have the time to deform laterally in a high-rate phenomena, a condition of uniaxial strain occurs. As time goes on stresses decrease and a state of uniaxial stress may take place, as release waves arrive from the lateral surfaces and lateral deformation and lateral

deformation occurs. In plate impact situations a state of uniaxial strain but 3D stress is produced, thus work on shock waves has been done on plate geometries. For plate geometries it is possible to study the material behaviour at shorter times and higher load, while at the same time benefiting of a 1D analysis for uniaxial strain. In plate impact theories, effects of thermomechanical coupling are neglected. These effects can be notable at strains exceeding 30%.

In Figure 2.6 the uniaxial stress – strain curve is shown. If we consider a situation of one dimensional deformation, as is the case of plane waves propagating through a material where dimensions and constraints are such that the lateral strains are zero (Figure 2.7), the stress uniaxial stress – strain curve assumes the form shown in Figure 2.8. This leads to the conclusion that the elastic modulus, yield strength, ultimate strength and elongation related to the uniaxial stress – strain curve cannot adequately describe the behaviour of a material subjected under shock loading.

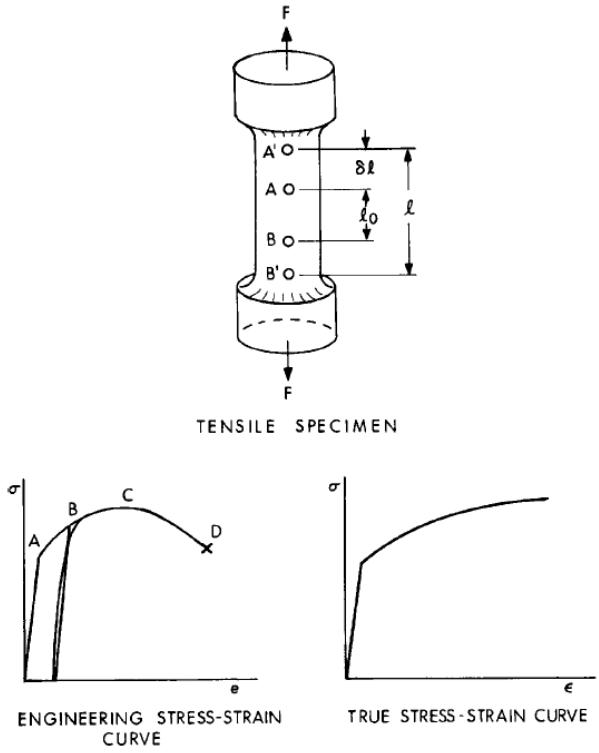

Figure 2.6 Test specimen and typical stress – strain curves for uniaxial stress states [8].

The stresses and strains that occur in one dimension deformation for an isotropic material will be considered in order to comprehend the change from Figure 2.6 to Figure 2.8. Strains must be less than 30% in the following analysis, otherwise a more complex analysis would be needed due to thermomechanical coupling.

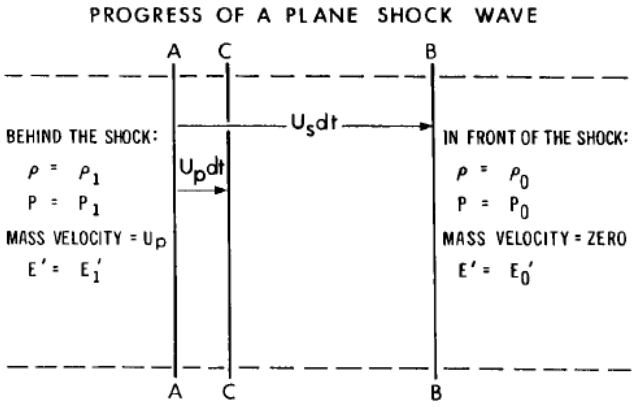

Figure 2.7 Detail of plane shock wave propagating in a solid [8].

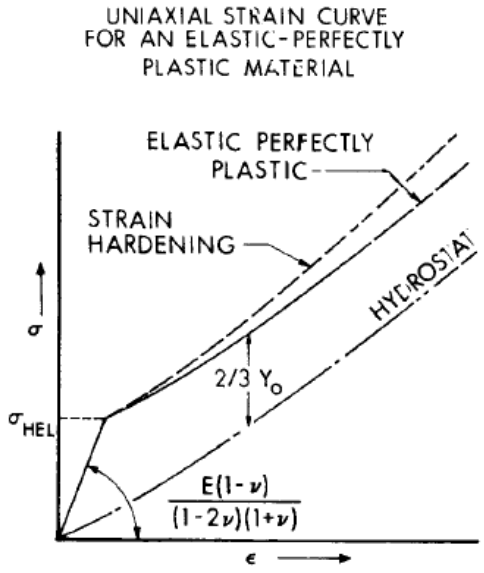

Figure 2.8 Stress-strain curve for uniaxial strain states [1].

Dividing the three principal strains into elastic and plastic components yields:

$$\varepsilon_1 = \varepsilon_1^e + \varepsilon_1^p \tag{2.33}$$

$$\varepsilon_2 = \varepsilon_2^e + \varepsilon_2^p \tag{2.34}$$

$$\varepsilon_3 = \varepsilon_3^e + \varepsilon_3^p \tag{2.35}$$

The subscripts (*1*, *2*, and *3*) indicate the three principal directions, while the superscript *e* refers to elastic and *p* to plastic.

For 1D deformation

$$\varepsilon_2 = \varepsilon_3 = 0 \tag{2.36}$$

It follows that:

$$\varepsilon_2^p = -\varepsilon_2^e \tag{2.37}$$

$$\varepsilon_3^p = -\varepsilon_3^e \tag{2.38}$$

The plastic portion of the strain is taken to be incompressible, so that

$$\varepsilon_1^p + \varepsilon_2^p + \varepsilon_3^p = 0 \tag{2.39}$$

Due to symmetry ($\varepsilon_2^p = \varepsilon_3^p$) we get

$$\varepsilon_1^p = -\varepsilon_2^p - \varepsilon_3^p = -2\varepsilon_2^p \tag{2.40}$$

Therefore

$$\varepsilon_1^p = 2\varepsilon_2^e \tag{2.41}$$

$$\varepsilon_1 = \varepsilon_1^e + \varepsilon_1^p = \varepsilon_1^e + 2\varepsilon_2^e \tag{2.42}$$

The elastic strain may be written in the terms of the stresses and elastic constants as

$$\varepsilon_1^e = \frac{\sigma_1}{E} - \frac{\nu}{E}(\sigma_2 + \sigma_3) = \frac{\sigma_1}{E} - \frac{2\nu}{E}\sigma_2 \tag{2.43}$$

$$\varepsilon_2^e = \frac{\sigma_2}{E} - \frac{\nu}{E}(\sigma_1 + \sigma_3) = \frac{1-\nu}{E}\sigma_2 - \frac{\nu}{E}\sigma_1 \tag{2.44}$$

$$\varepsilon_3^e = \frac{\sigma_3}{E} - \frac{\nu}{E}(\sigma_1 + \sigma_2) = \frac{1-\nu}{E}\sigma_3 - \frac{\nu}{E}\sigma_1 \tag{2.45}$$

Combining equation (2.42) and the above equations, the following expression for ε_1 is obtained

$$\varepsilon_1 = \frac{\sigma_1(1-2\nu)}{E} + \frac{2\sigma_2(1-2\nu)}{E} \tag{2.46}$$

The plasticity condition for either the Tresca or von Mises conditions for this case is

$$\sigma_1 - \sigma_2 = Y_0 \tag{2.47}$$

Expressing σ_2 from (2.47) and inserting it into (2.46) gives

$$\sigma_1 = \frac{E}{3(1-2\nu)}\varepsilon_1 + \frac{2}{3}Y_0 = K\varepsilon_1 + \frac{2}{3}Y_0 \tag{2.48}$$

Where $K = E/3(1-2\nu)$ is the bulk modulus.

Solving the above equations for stress in terms of pressure (*P*), we obtain

$$\sigma_1 = P + \frac{2}{3}Y_0 \tag{2.49}$$

Equation (2.49) is the stress – strain relation for the case of uniaxial strain. Recalling the expression for uniaxial stress $\sigma = E\varepsilon$, we can see that the bulk compressibility represents the most significant difference between uniaxial stress and uniaxial strain. For the state of uniaxial strain the stress continues to increase regardless of the yield stress or strain hardening.

For the special case of elastic 1D strain

$$\varepsilon_1 = \varepsilon_1^e \tag{2.50}$$

$$\varepsilon_2 = \varepsilon_2^e = \varepsilon_3 = \varepsilon_3^e = 0 \tag{2.51}$$

$$\varepsilon_1^p = \varepsilon_2^p = \varepsilon_3^p = 0 \tag{2.52}$$

Therefore,

$$\varepsilon_2^e = 0 = \frac{1-\nu}{E}\sigma_2 - \frac{\nu}{E}\sigma_1 \tag{2.53}$$

$$\sigma_2 = \left(\frac{\nu}{1-\nu}\right)\sigma_1 \tag{2.54}$$

Which leads to

$$\varepsilon_1 = \frac{\sigma_1}{E} - 2\nu^2\frac{\sigma_1}{E(1-\nu)} \tag{2.55}$$

or

$$\sigma_1 = \frac{(1-\nu)}{(1-2\nu)(1+\nu)}E\varepsilon_1 \tag{2.56}$$

Figure 2.8 shows the stress-strain curve for the case of uniaxial strain. We can see from Figure 2.8 that the modulus for the uniaxial strain curve increases by a factor of $(1-\nu)/[(1-2\nu)(1+\nu)]$ with respect to the uniaxial stress – strain case. The yield point for uniaxial strain is referred to as the Hugoniot Elastic Limit (σ_{HEL}) and it corresponds to the maximum stress for 1D elastic wave propagation in plate geometries. The curve labeled "hydrostat" in Figure 2.8 is also known as the Hugoniot curve. This is the curve that a material would follow if it were strengthless. There is a constant deviation from the Hugoniot curve of the stress σ by $2Y_0/3$ where Y_0 is the static yield strength. If the yield strength changes in a strain-hardening material, so will the difference between the σ and P curves.

Figure 2.9 shows a typical loading cycle in uniaxial strain for an elastic – perfectly plastic material. Observe that at point *C* reverse yielding occurs. By assuming that tensile and compressive yield strengths are equal, then when reverse loading occurs (e.g. stress wave reflections from a free surface) the line segment *CD* extends to the negative (tension) region, but still different by $2Y_0/3$ from the hydrostat.

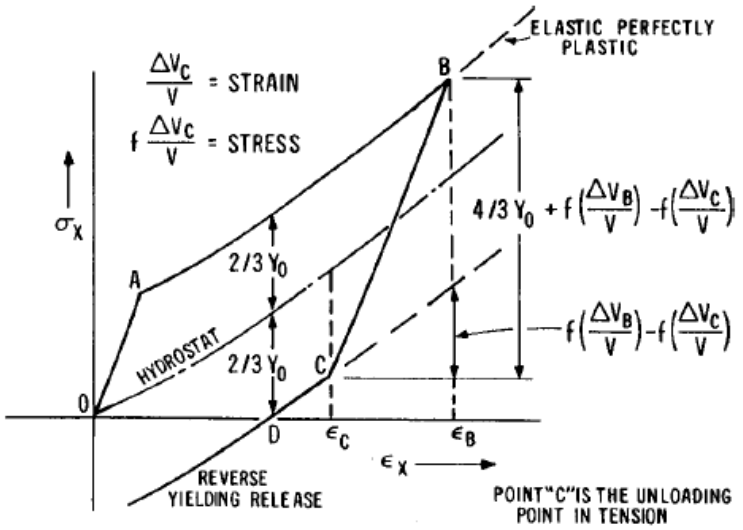

Figure 2.9 Loading-unloading cycle in uniaxial strain [1].

2.2.2. Wave propagation

The uniaxial strain stress-strain curve taken to much higher load levels is depicted in Figure 2.10.

A single elastic wave will propagate in the material when the stress is less or equal to the Hugoniot elastic limit. For a situation when the applied stress exceeds σ_{HEL}, an elastic wave followed by a plastic wave will propagate through the material. The propagation velocity of the elastic wave is

$$C_E^2 = \frac{E(1-\nu)}{\rho_0(1-2\nu)(1+\nu)} \tag{2.57}$$

For a plastic wave the propagation velocity is a function of the slope of the stress – strain curve at a given value of strain. It is given by the following expression

$$c_p = \sqrt{\frac{1}{\rho_0}\frac{d\sigma}{d\varepsilon}} \tag{2.58}$$

Multiple plastic waves can propagate through the material, and each one is a function of a particular value of plastic strain.

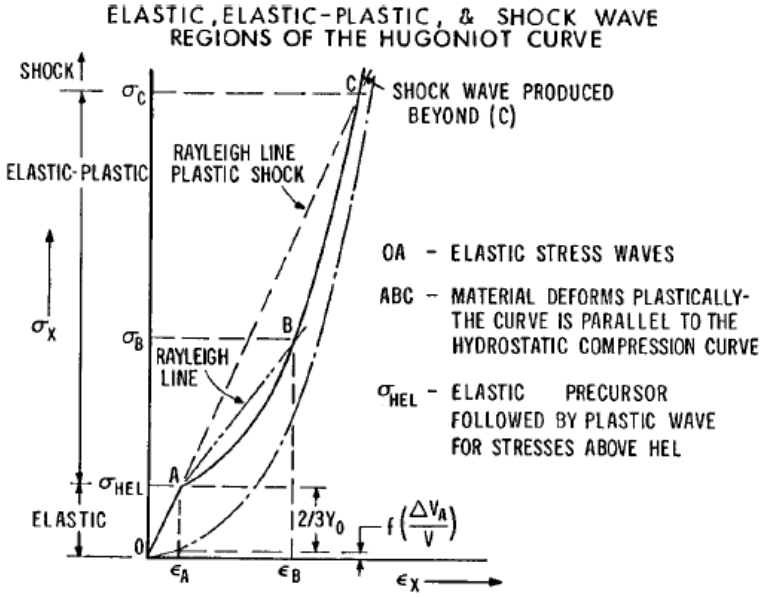

Figure 2.10 Regions of elastic, elasto-plastic and shock wave propagation [1].

For stresses above σ_c (Figure 2.10) the material will behave plastically and shows characteristics similar to a fluid. In Figure 2.10 a domain of strong shock waves is present above the value of σ_c. A single steepfronted shock wave propagates in this region. The propagating velocity of a shock wave is determined through an equation of state (EOS), and is usually labelled as *U*.

Next, the formation of a shock wave is briefly presented. In general, sound velocity is proportional to the ratio of the change in pressure with a change in density

$$c = \frac{dP}{d\rho} \tag{2.59}$$

Since the relation of pressure and density is linear in the elastic region, the sound velocity in this region is constant. Beyond the elastic region the relation P/ρ is not anymore linear and the wave velocity increases with pressure or density. Therefore, as the stress pressure increases, the same occurs with the wave speed.

A portion of a pressure wave moving to the right is shown in Figure 2.11. In this wave the pressure magnitude is low at point *A*, as a consequence also the particle velocity is quite low. This in turn results in low velocity if the pressure wave. If we move to point *B*, where stress is above the elastic limit, the wave velocity will increase with increasing pressure. Therefore, the wave velocity at point *B* is than at point *A*. In the same way at point *C* the wave velocity gets still higher than at point *B*. Hence, this leads to the increase of the wave steepness until it becomes a straight vertical line, as shown in Figure 2.12. When the wave assumes this vertical front it is called a shock wave. Now there is a discontinuity between the shocked material behind the wave and the unshocked material in front of the wave, i.e. there is no smooth transition of matter in front of the wave to matter behind the wave.

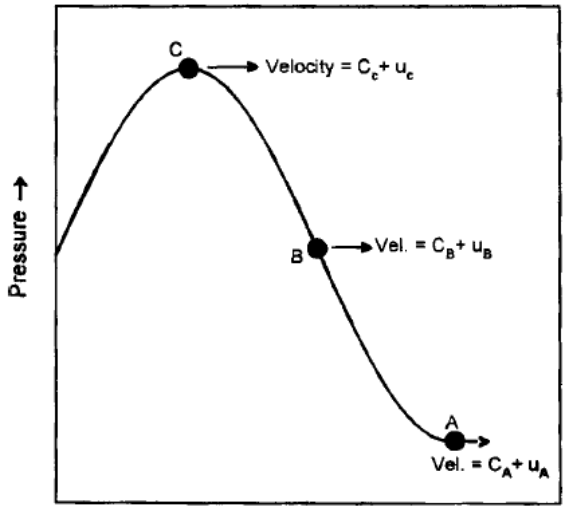

Figure 2.11 Propagating high-pressure wave [9].

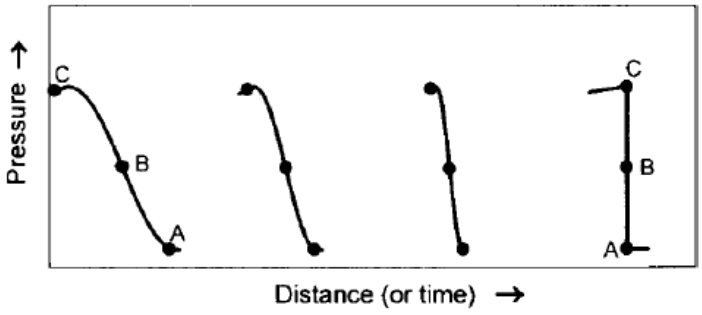

Figure 2.12 Buildup of a pressure wave to a shock wave [9].

For the applied load of finite duration an elastic unloading wave is generated upon the removal of the load (Figure 2.13). The unloading wave moves faster than the compressive wave. For a pulse of short duration the compressive amplitude may be attenuated by unloading from the rear. The catch – up distance is the point at which the unloading occurs.

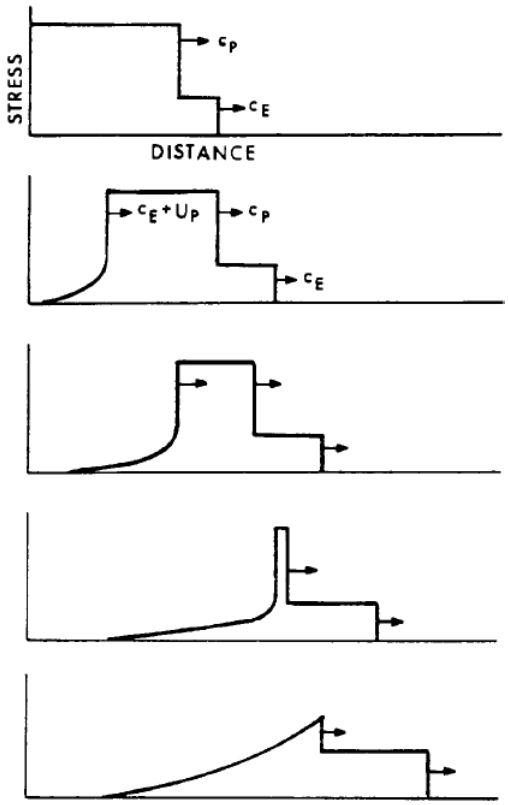

Figure 2.13 Decay of a shock wave due to rarefaction wave catching up from the rear [8].

2.2.3. Conservation equations for a shock wave

As seen in the previous section, a shock wave has a steep front and requires a state of uniaxial strain in which the hydrostatic component of stress increases to high levels. When a shock wave is created, the pressure in a solid can exceed material strength by factors of 10 – 100, hence the solid can be considered as behaving like a compressible fluid.

The following basic assumptions are made [5]:

- A shock is a discontinuous surface and has no apparent thickness.
- The shear modulus of the material is assumed to be zero, such that it responds to the wave as a fluid; hence the theory is restricted to higher pressures.
- Body forces (such as gravitational) and heat conduction at the shock front are negligible.
- There is no elastoplastic behaviour
- Material does not undergo phase transformations.

Let's consider Figure 2.14, in which is depicted a cylinder of unit-cross sectional area onto which a piston penetrates. Initially, the piston is at rest, and the material is at pressure P_0 and has a density ρ_0. Then the piston is pushed with the velocity U_p into the compressible material. The pressure pulse propagates ahead of the piston with velocity U_s. After a time t_1, the highly compressed region ahead of the piston has moved forward by a distance equal to $U_s t_1$, while the piston has moved by a distance equal to $U_p t_1$. At this point the material in the compressed region has a pressure P and density ρ. A shock front can be thought of as a plane separating ''moving'' from ''stationary'' fluid in a cylinder with a moving piston. The velocity of the front is U_s, while the particles (or atoms) at the shock front and behind it are moving at a velocity U_p. The pressure buildup is caused by this particle displacement. Ahead of the front the particles are stationary. The shock wave moves at a velocity higher than the piston velocity. The distance that the piston and the shock wave have travelled in time t_1 is $U_p t_1$ and $U_s t_1$, respectively.

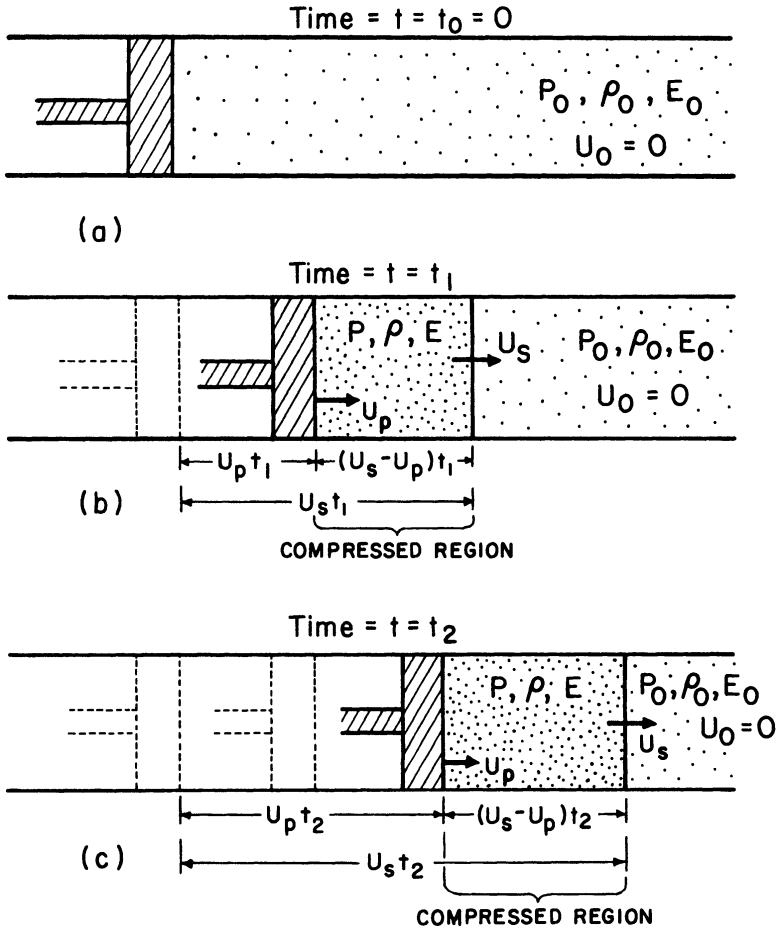

Figure 2.14 Successive positions of an idealized piston moving into a cylinder with compressible fluid [5].

Conservation of mass. The mass moving toward the front can be expressed as $A\rho_0(U_s - U_0)dt$, while the mass moving away from the front equals $A\rho(U_s - U_p)dt$. By equating the mass that comes in with the mass that goes out per unit area, we obtain:

$$A\rho_0(U_s - U_0)dt = A\rho(U_s - U_p)dt \tag{2.60}$$

or, if $U_0 = 0$ we have,

$$\rho_0 U_s = \rho(U_s - U_p) \tag{2.61}$$

Equation (2.61) is the equation for the conservation of mass.

Conservation of momentum. The conservation of momentum can be expressed by equating the change in momentum with the impulse per unit cross-sectional area

$$A\rho(U_s - U_p)U_p dt - A\rho_0(U_s - U_0)U_0 dt = (P - P_0)Adt \tag{2.62}$$

$$\rho_0(U_s - U_0)(U_p - U_0) = P - P_0 \tag{2.63}$$

For $U_0 = 0$

$$(P - P_0) = \rho_0 U_s U_p \tag{2.64}$$

This is the equation for the conservation of momentum. The quantity $\rho_0 U_s$ is often called the shock impedance.

Conservation of energy. The conservation of energy is obtained by equating the difference of the work done by P and P_0 to the change in total energy (kinetic plus internal) between the two sides of the front:

$$\begin{aligned} PAU_p dt - P_0 AU_0 dt = {} & \frac{1}{2}\left[\rho A(U_s - U_p)dt\right]U_p^2 + EA\rho(U_s - U_p)dt \\ & - \left\{\frac{1}{2}\left[\rho_0 A(U_s - U_0)dt\right]U_0^2 + E_0 A\rho(U_s - U_0)dt\right\} \end{aligned} \tag{2.65}$$

For U_0=0

$$PU_p = \frac{1}{2}\rho(U_s - U_p)U_p^2 - E_0\rho_0 U_s + E\rho(U_s - U_p) \tag{2.66}$$

And by substituting (2.61) in the above equation, we obtain

$$PU_p = \frac{1}{2}\rho_0 U_s U_p^2 + \rho_0 U_s \left(E - E_0\right) \tag{2.67}$$

Here E_0 and E are the specific internal energy in front and behind the shock front, respectively.
Eliminating U_s and U_p from (2.67) gives the Rankine-Hugoniot relation (also called the "Hugoniot")

$$E - E_0 = \frac{1}{2}\left(P + P_0\right)\left(\frac{1}{\rho_0} - \frac{1}{\rho}\right) = \frac{1}{2}\left(P + P_0\right)\left(V_0 - V\right) \tag{2.68}$$

Where $V_0=1/\rho_0$ and $V=1/\rho$ are the specific volumes.
Equations (2.61), (2.64), and (2.67) (or (2.68)) are called the Rankine-Hugoniot jump conditions.
In the above conservation equations, there are five variables: pressure (P), particle velocity (U_p), shock velocity (U_s), specific volume (V) (or density (ρ)), and energy (E). One more equation is needed to express all parameters as a function of one of them. Usually this additional equation is the experimentally determined relationship between shock and particle velocity. An empirical relationship between U_s and U_p is given by the following polynomial equation with parameters C_0, S_1, S_2, S_3,…:

$$U_s = C_0 + S_1 U_p + S_2 U_p^2 + \cdots \tag{2.69}$$

Equation (2.69) is called the equation of state (EOS) of a material and is a fundamental equation for modelling the material behaviour in impact simulations in chapter 5. In this equation C_0 is the sound velocity in the material at zero pressure and S_1 and S_2 are empirical parameters.
The Rankine-Hugoniot equation gives a relation between P and ρ immediately behind the shock. A Hugoniot is plotted in Figure 2.15 as a P-V curve. Each point on the Hugoniot corresponds all shocked states in a material, therefore, the Hugoniot identifies all shocked states in a material and describes the material properties. The straight line joining (P_0, V_0) and (P_1, V_1) is known as the Rayleigh line and refers to the shock state at P_1. If there is a shock pulse of amplitude P_1, it does not reach this point by following the Hugoniot line. Rather, it changes discontinuously from its initial value P_0 to its value P_1. This discontinuity is explained by the slope of the Rayleigh line (Figure 2.15) that is proportional to the square of the shock wave velocity U_s, and is equal to:

$$\frac{P - P_0}{V - V_0} = -\rho_0^2 U_s^2 \tag{2.70}$$

From the above equation can be observed that when pressure increases, the magnitude of the slope and velocity of the wave also increases.

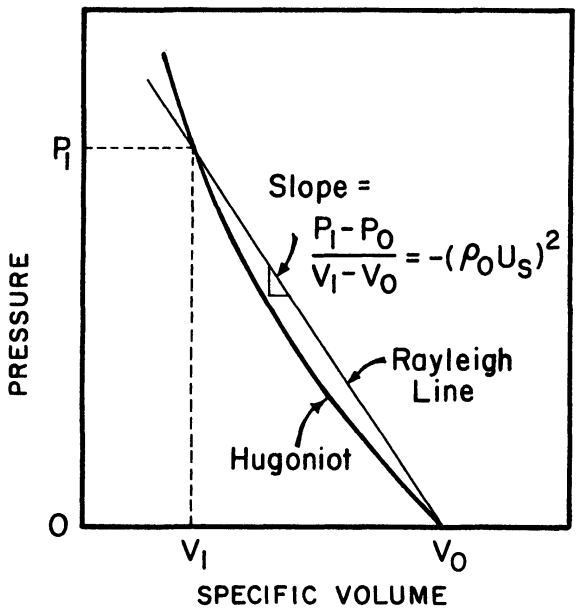

Figure 2.15 Characteristic Hugoniot (*P*-*V*) curve showing Rayleigh line [5].

3. Multifunctional panels structure

3.1. Introduction

Multifunctional structural materials or systems possess the basic strength and stiffness dictated by loads acting on them and have additional functions beyond the structural one. The objectives and motivation for the development of materials/systems of this kind is to improve efficiency, safety, versatility and reduce size, weight, cost, power consumption, and so on, of the multifunctional systems with respect to the traditional approach where different functions are performed by different and independent (non-integrated) units. The functionalities of multifunctional material systems can include integrated structural, electromagnetic, self-healing, energy storage, energy harvesting, thermal, sensing and actuation, and other capabilities [[10],[11]]. Since almost every object around us has a structure, whether to support forces acting on it or to support its sub-components, most of the multifunctional concepts have been developed by exploiting the structure, thereby combining it with some additional function into a multifunctional structure, as the name itself says. A large number of multifunctional material systems has been proposed so far, where in a material that is capable of bearing mechanical loads and serves as structural element, one or more structural or non-structural functions have been integrated [[10]-[15]]. Aerospace and military fields are currently the main application areas of multifunctional materials and structures.

In this work a multifunctional structure that, besides being a structural element with the function of supporting loads acting on the structure, is able to seal holes following an impact event is presented. This multifunctional structure is investigated under hyper velocity impacts. In the multifunctional structure presented herein the multiple functionality is achieved by combining different materials for different functions in one multilayer configuration, where each layer performs a specific function. In this way a plate element with the structural and self-healing functions is obtained. The self-healing in this panel refers to the sealing of the hole caused by a perforating impact, and not to the restoration of mechanical strength in the hole zone.

3.2. Self-healing materials

In [16] self-healing is defined as ‘‘the ability of a material to heal (recover/repair) damages automatically and autonomously, that is, without any external intervention’’. Despite of this definition, often an external trigger is needed to generate the self-healing process in manmade materials. This leads to the following two types of self-healing mechanisms:

- autonomic (without any intervention)

- nonautonomic (needs human intervention/external triggering)

Another classification of self-healing materials according to the healing agent is appropriate. When the repairing agent is different from the structural material and is incorporated into the main matrix as a discrete entity, the self-healing is classified as extrinsic. On the contrary, when the repairing capability is contained in the structural material itself (no additional healing substance), this is classified as intrinsic self-healing. In extrinsic self-healing systems the healing agent is stored in microcapsules [17], hollow fibres [[18],[19]], or microvascular systems [[20],[21]], which are embedded in the system during the manufacturing process. When a crack forms and propagates it breaks the reservoir and the healing agent leaks into the crack due to capillary forces, thus filling the crack. This process is also autonomic as there is no need for external or manual intervention. In intrinsic healing systems the polymer matrix gains temporary mobility when an external or internal trigger is applied, such as thermal, photo, or chemical activation. Since a trigger is needed to activate the reparation process those systems are considered as nonautonomic. Some examples of intrinsic self-healing are reversible covalent bonds [[22],[23]], supramolecular interactions [24], shape memory polymers [25], and polymer blends [26]. An advantage of intrinsic healing systems is the capability of performing multiple healing events at single damage site. A review of recent developments in self-healing polymeric materials is presented in [27].

3.3. Multifunctional panel concept

As part of a project named IMBEMUS (Impact Behaviour of Multifunctional Materials), a group of researchers at the University of Padua have started working on the development of a multifunctional structure system. The idea of this multifunctional system is a panel that can perform the following three functions:

1) act as a structural element
2) close holes caused by a perforating impact
3) detect the occurrence and location of a perforating impact on the panel

All three of the above functions would be incorporated in one panel, which would result in a multifunctional panel. To achieve the multiple functions listed above, the panel is conceived as a multilayer plate consisting of several different layers, where each layer in the assembly has a specific task. So, according to the functions of the multifunctional panel, there are three different types of layers:

a) structural layer
b) self-healing layer
c) sensor layer

The structural layer provides to the panel the ability to support loads acting on it, the self-healing layer is used to provide the self-repairing of the hole caused by a perforating impact event, and the sensor layer provides a mean to detect where and if a perforating impact happened. A sketch of a possible multifunctional panel cross section configuration is depicted in Figure 3.1, where the different layers are combined in one panel assembly (Figure 3.1 (a)). After a perforating impact, all the layers, except for the self-healing one, remain perforated. The self-healing layer on the other hand should be able to close the hole (Figure 3.1 (b)) automatically and immediately after the impact, without the need of external intervention. Each layer can occur once or more in the multifunctional panel configuration. The occurrence frequency of each type of layer and their relative positions in the panel configuration affect directly the multifunctional panel performance under impact. The configuration, dimensions and materials of the structural layers can be selected according to the forces expected to act on the panel. Therefore, this concept presents an adaptable solution from the structural perspective.

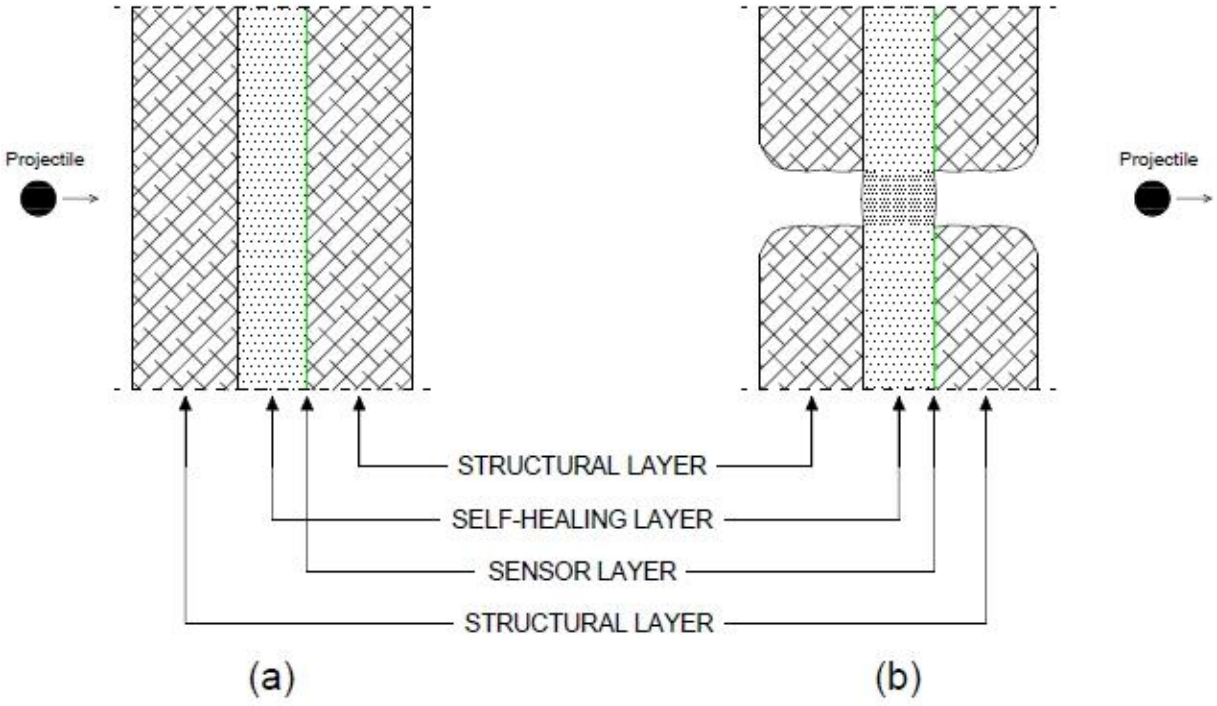

Figure 3.1 Multifunctional panel structure concept: (a) before impact and (b) after impact.

In this thesis the impact behaviour of several multifunctional panel configurations is investigated. To this end, two slightly different structural layers and a self-healing layer were studied under hyper-velocity impact loading, which is presented in the next chapter. Since the sensor layer thickness should be a fraction of a millimetre, its structural (mechanical) contribution to the impact response of the panel assembly can be considered as negligible. Therefore, the sensor layer has not

been considered in this work. While there is plenty of choice for the materials to be applied in the structural layers, this is certainly not the case for the self-healing layer. An ionomeric polymer with the trade name Surlyn® 8940 has been chosen for the self-healing layer. This ionomer is known for its characteristic to self-repair a hole following an impact caused perforation [[28],[29],[30]]. For the structural layers composite materials were used. Therefore, in order to obtain a multifunctional panel with the aforementioned capabilities, a composite and ionomer panel/layer are joined together in a multilayer plate assembly. An example of such panel is shown in Figure 3.2, it consists of one structural (composite material) and one self-healing (ionomer) layer. Although the ionomer layer principal function is to give self-healing property to the panel, its presence and location could affect the panel response to impact. Similarly the composite structural layer could affect the self-healing function of the panel, since it is not the same if the ionomer is alone or it is incorporated in a multilayer assembly when impacted. Therefore, the structural and self-healing layers were investigated under impact loading for several different configurations and also each part has been investigated independently.

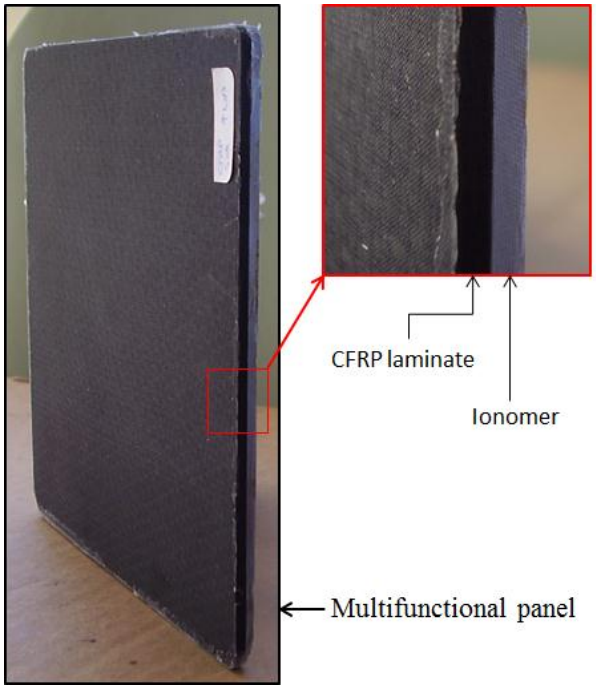

Figure 3.2 Multifunctional panel consisting of a CFRP laminate layer and an ionomer layer.

When a structural element is perforated, and if the hole isn't too big with respect to the structure, it can still sustain most of the loads acting on it. If the structure at the same time is also a barrier between two media and its preventing their mixing, then a hole would make the structure useless once perforated, because leakage through the structure in the hole area would start. For this reason the idea for the panel presented herein is to apply the self-healing ionomer layer as a prevention for

leaking, and therefore making the multifunctional system ‘‘less’’ vulnerable to impacts then the structural system alone. In this way the structural layers could be less concerned with the local effect of the impact loads, and their dimensions could be tailored according to other loads present in the environment. A natural and obvious application for this multifunctional panel would be for anti-leakage purposes of fluid-containing structures that can be exposed to perforating impacts (e.g. fuel or chemical storage).

3.4. Structural layers

Two structural layers have been used in the largest part of the experimental campaign. Both structural layers for the multifunctional panel investigated in this work are made of fibre reinforced polymers. The choice of a composite material for the structural part of the panel is motivated by its high strength to weight and stiffness to weight ratios. Because the panel’s multiple functionality is obtained at the cost of mass increase, since different layers had to be incorporated in one assembly, the application of composite materials for the structural parts somewhat alleviates the mass increment caused by the addition of various layers in one panel with respect to more traditional materials (e.g. metal alloys). In applications where weight reduction is an important issue (e. g. aerospace field) composite materials represent an attractive choice.

One of the layers is made of carbon fibre reinforced plastics (CFRP). This layer has a thickness of 3.6 millimetres. It consists of 12 unidirectional laminas, each thick 0.3 millimetres. The stacking sequence of the laminas in the laminate is $[0/90/0/90/0/90]_2$. The fibres in the CFRP laminate are T600 24K, and the matrix is REM epoxy matrix. The fibre volume ratio is 60%.

The other structural layer is a CFRP laminate with woven aramid fibre / epoxy composite layers attached on its top and bottom face, as shown in Figure 3.3. The CFRP layer is made up of 8 laminas which are equal to those in the CFRP structural layer, and the stacking sequence is $[0/90/0/90]_2$. The surface layers consist of an aramid fibres fabric Twaron® in an epoxy matrix IMP503Z. The Twaron®/epoxy composite laminate is 0.47 millimetres thick. The resulting thickness of the Twaron®-CFRP-Twaron® (TCT) structural layer is 3.34 millimetres.

Six tests of the experimental campaign were also done with a woven CFRP structure. This structure is composed of carbon-fabric/epoxy composite laminas. Three samples are 1.1 millimetres thick with a stacking sequence [0/45/-45/0], and three samples are 2.2 millimetres thick with a stacking sequence $[0/45/-45/0]_2$.

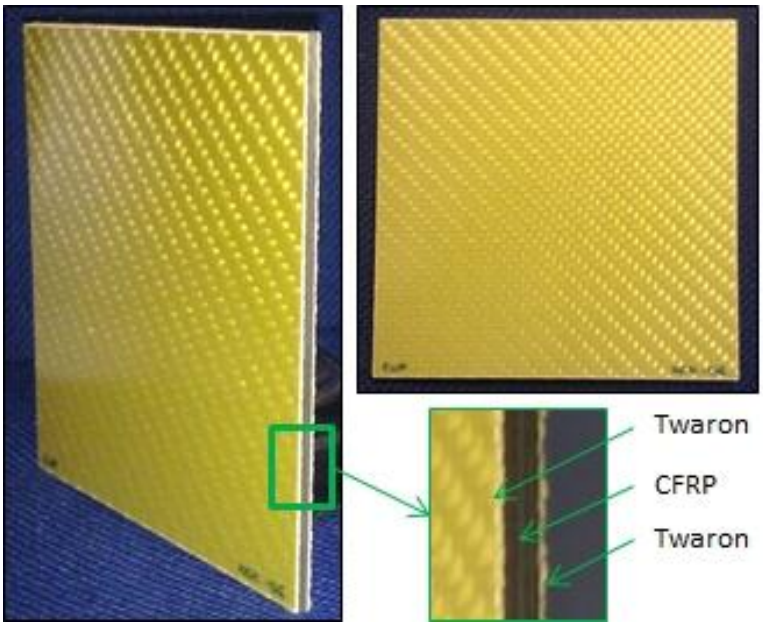

Figure 3.3 Structural layer made of Twaron® and CFRP.

3.5. Self-healing layer

The self-healing layer is made of an ionomeric polymer known commercially as Surlyn®. Surlyn® is a ionomer thermoplastic resin. Surlyn® is the DuPont trade name for the ethylene-co-methacrylic acid (EMAA) copolymer.

The EMAA ionomers have been observed to self-heal after an impact event [[28]-[31]]. This ability is an inherent material response and occurs automatically and instantaneously without the need for manual intervention. Due to this self-healing ability, the Surlyn® EMAA ionomer is chosen to comprise the self-healing layer of the multifunctional panel. The ionomer samples were produced by the Aerospace Science and Technology Department at the Politecnico di Milano, Milan, Italy.

3.5.1. Ionomers

In [32] ionomers were defined as a class of ion-containing copolymers in which the maximum ion group content is ~15 mol%. This definition was further refined, in order to distinct ionomers from polyelectrolytes. In [33] ionomers were defined as polymers whose bulk properties are governed by ionic interactions within the discrete regions within the polymer structure. Ionomers are produced by a process known as copolymer neutralization. In this process precursor copolymers containing both ionic (anionic) and non-ionic repeat groups are used to derive ionomers. The anionic acid component is neutralized forming an ionic pair with a metallic cation. This produces the ionomer with ionic groups attached along the polymer chain. The number of acid groups that is neutralized in the initial copolymer influences the amount of ionic content present in the ionomer.

The ionic pairs present in these materials group into discrete regions known as multiplets. A multiplet is an aggregate consisting of several ion pairs (inner dashed circle in Figure 3.4). According to the Eisenberg-Hird-Moore (EHM) model (Figure 3.4) [34] these ion pairs anchor their attached polymer chains to the multiplet. This causes a reduced mobility of the attached polymer chains near the multiplet. Due to this significantly reduced mobility, with respect to that of the bulk polymer, the surrounding area of the multiplet is known as the restricted mobility region (outer dashed circle in Figure 3.4). Beyond the limits of the restricted mobility region the polymer chains return to their typical bulk mobility.

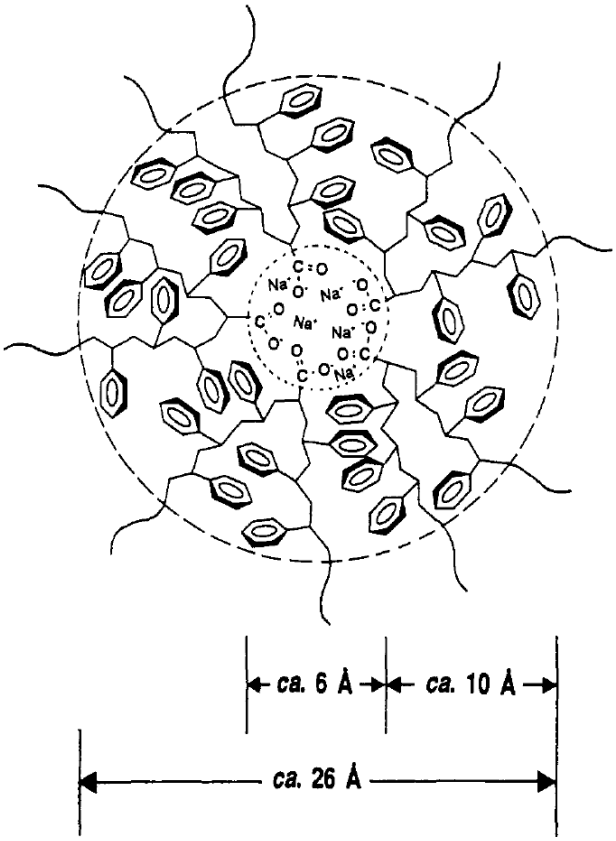

Figure 3.4 Schematic diagram of the region of restricted mobility surrounding a multiplet in a poly(styrene-co-sodium mathacrylate) ionomer [34].

An increase in ionic content is followed by a creation of numerous multiplets within the ionomer structure. The increase in number of multiplets to a certain level, causes overlapping of the restricted mobility regions of the neighbouring multiplets. This, in turn, causes the formation of a more continuous restricted region in the polymer structure (Figure 3.5), defined as the ionic cluster. The ionic cluster region has its own Tg, different from the one of the bulk properties. Figure 3.5 shows an increase in ionic content from ‘‘a’’ to ‘‘c’’, causing the formation of ionic cluster. The multiplets are shown as small circles, while the restricted mobility region is represented as a grey area.

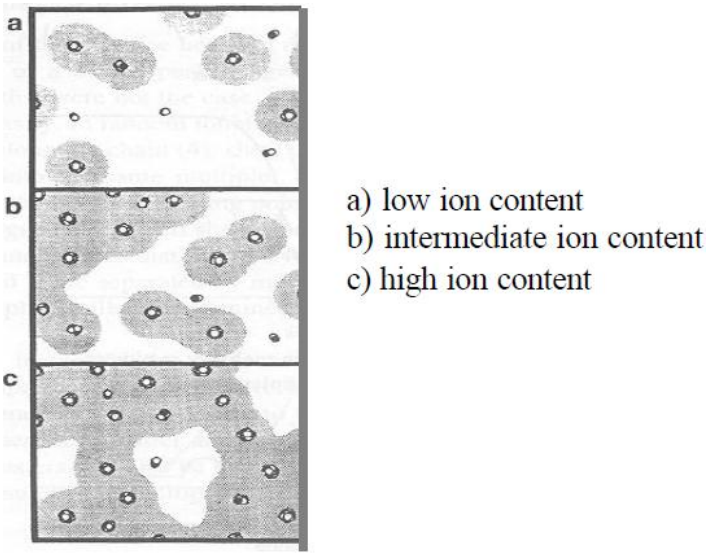

Figure 3.5 Schematic diagram showing the growth of multiplets and the formation of clusters with increases in ionic content [34].

The ionomer mechanical properties are highly affected by the amount of ionic content. An increase in ionic content is observed to cause an increase in tensile strength, modulus and toughness of the ionomer [[35],[36]]. The formation of ionic aggregates affects also the thermal characteristics of ionomers. During heating, the ionic groups transit from an ordered state to an disordered state [37], as shown in Figure 3.6 (red circles).

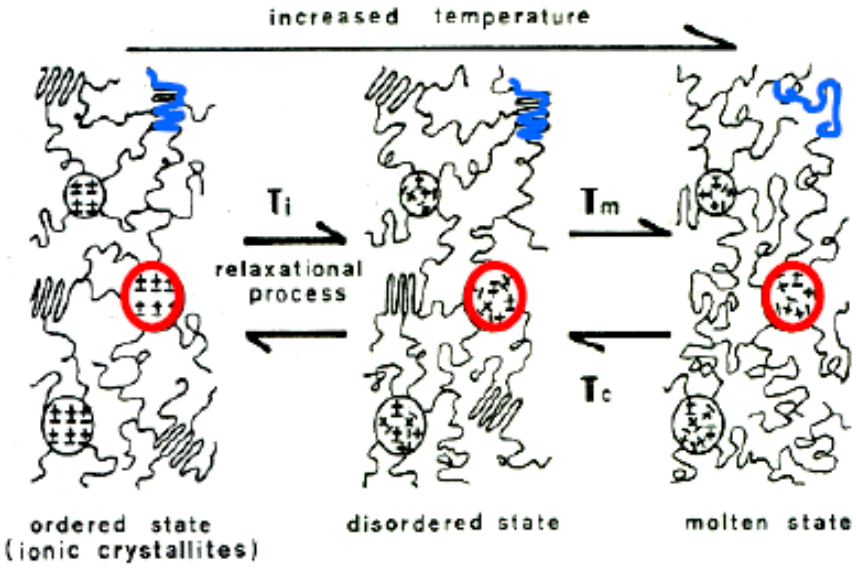

Figure 3.6 Model representing the effects of the heating/cooling cycle on ionomer order-disorder and crystallization [37].

This transition was identified as an order-disorder transition, and occurs when heating above a certain temperature T_i. This temperature T_i is lower than the melting temperature (T_m) of the crystalline regions of the polymer chain. With further heating above T_i, the polymer crystallites melt

at temperature T_m (Figure 3.6). During cooling (T_c), the polymer crystallites form rapidly, while the ionic regions remain disordered even when the room temperature is reached and they reorder through the long-time relaxation process.

3.5.2. Surlyn®

Surlyn® is an ionomer synthesized by DuPont. Surlyn® is a random copolymer consisting of poly(ethylene-co-methacrylic acid). It contains 5.4 mol% methacrylic acid (MA) groups distributed along the polymer chain, and has been neutralized with a cation (Figure 3.7). There are various types of Surlyn® produced by DuPont. In this study Surlyn® 8940 was used. Surlyn® 8940 has 30% of its MA groups neutralized with sodium cations.

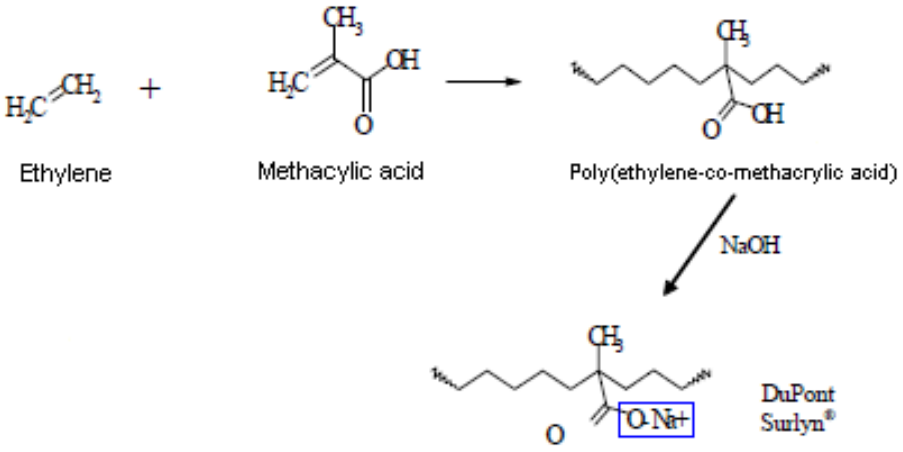

Figure 3.7 Surlyn® chemical structure [29].

3.5.3. Self-healing of the ionomer

The EMAA based ionomers have been observed to exhibit self-healing behaviour following a ballistic impact [[28]-[31]]. For a material that doesn't have the self-healing capability, the resulting damage after a perforating impact is a hole through the material, with the size of the hole being dependant on the impactor velocity, and impactor-target dimensions and materials. EMAA based ionomers self-healing capability is able to seal the hole, leaving only a ‘‘scar’’ in the impact area (Figure 3.8). This hole repair (healing) process occurs instantaneously and automatically, without any manual intervention, but it is limited to specific conditions of temperature, bullet shape and speed. As this self-healing response is an inherent EMAA ionomer property, it can be classified as intrinsic self-healing. Furthermore, the self-healing can be accomplished multiple times at the same damage site. In [28], temperature measurement by thermal IR camera evidenced a temperature increase up to the melting temperature (~98°C) during a 9 millimetres bullet impact, and a rapid decrease to room temperature with distance from the hole was observed.

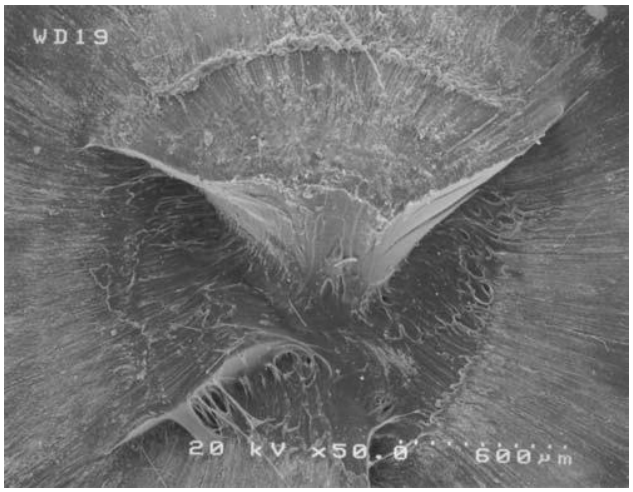

Figure 3.8 Scanning electron micrograph of healed EMAA ionomer following puncture with 4.5 mm diameter projectile [38].

In [[29],[31]] a ballistic self-healing two stage mechanism for the ionomer was proposed (Figure 3.9). As seen in Figure 3.9, in the first stage the cooler material in the impact area elastically snaps back after the projectile passage, thus closing the hole and bringing the molten material in contact. Then in stage two the molten surfaces bond together through interdiffusion, thus sealing the hole.

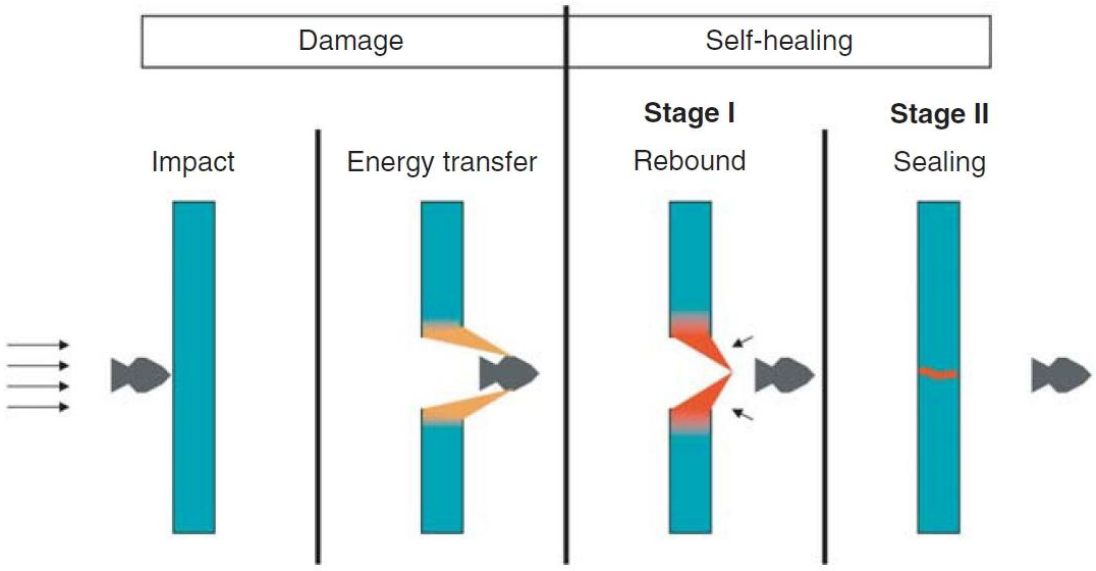

Figure 3.9 Two stage model for ballistic self-healing in EMAA based ionomer panel [38].

The study of EMAA based ionomers with different ionic and with no ionic content done in [[29],[31]], showed that ionic interaction is not the reason of the self-healing behaviour.

In [[29],[39]] tests for a range of temperatures from below to above room temperature were performed the limitations imposed on the self-healing performance of EMAA ionomers by the environment temperature. Samples tested at temperature above 60°C presented no healing, while for tests at temperatures down to -30°C most samples maintained the self-healing behaviour.

3.6. Multifunctional panels configurations

The assembly of the structural and self-healing layers can vary in the number of each layer type and their location with respect to each other. The impact behaviour of several configurations was studied. In order to facilitate the identification of various configurations, capital letters are assigned to each specific layer. Thereby, the structural layer made of CFRP is named as panel (layer) A, the structural layer made of Twaron® and CFRP is labelled as panel C, and the self-healing ionomer layer is labelled with the letter B. Furthermore the first letter in the configuration name indicates the impact side. For example, to indicate a configuration consisting of a CFRP structural layer and a ionomer self-healing layer, impacted on the ionomer side, we would use BA (B = ionomer, A = CFRP, first letter = impact side = B). The tested panels configurations were: B, A, C, AB, BA, CB, BC, ABA, ABC, CBA, and CBC. Configurations AB and CBA are shown in Figure 3.10.

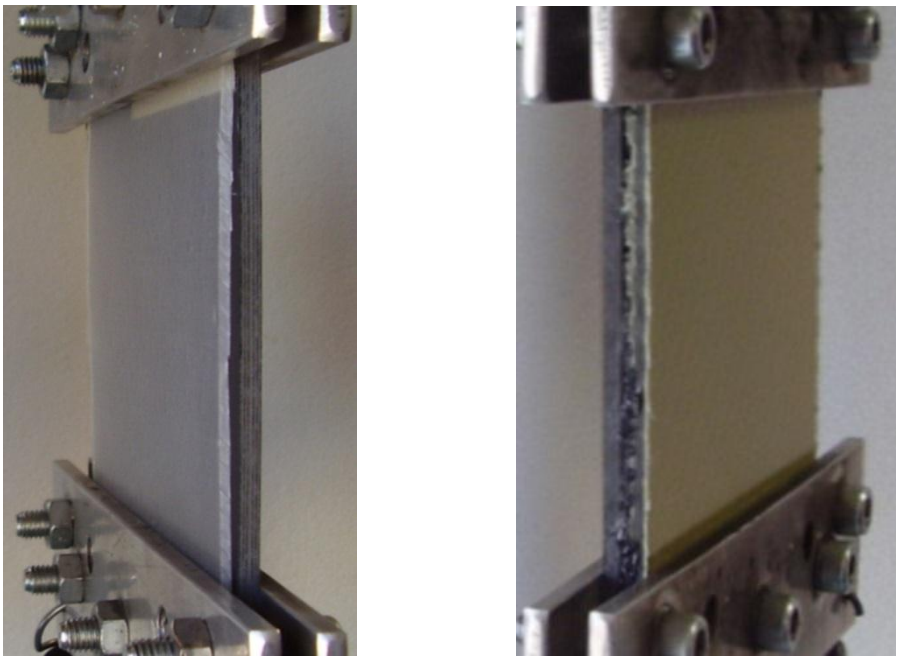

Figure 3.10 Examples of configurations AB (left) and CBA (right).

As it can be seen from the listed configurations, also the single parts were tested independently. Anyway, the ionomer itself is a multifunctional structure, because it can be used as a structural element and it possesses also the self-healing ability. But, as its mechanical properties are low for common engineering structures, coupling with a structural composite material improves that aspect. After testing the individual parts alone, the number of parts in a configuration was increased and with each increase in the number of parts all reasonable layouts of the parts (i.e. configurations) were investigated.

Almost all of the tested configurations were assembled by placing the layers in direct contact and holding them together by a frame structure (see chapter 4). This way of holding the parts together in one assembly does not resemble a real application panel, but it gave more flexibility when conducting the tests, because it was not known in advance, due to available number of individual parts and time limitations, how many tests per configuration would be executed, and therefore how many specific configurations would be needed. Few tests were also carried out on assemblies where the individual parts were glued to each other by means of adhesive.

4. Experimental investigations and results

4.1. Introduction

The panels presented in chapter 3 were investigated experimentally under high- and hyper-velocity impacts. In this chapter the experiments are described and the obtained results are given and discussed. The experimental campaign was executed at the Centre of Studies and Activities for Space (CISAS) impact laboratory.

In order to assess the panels impact behaviour under experimental testing, several measurements were performed. These include, momentum transfer from the debris cloud (which propagates from the target's back face) to structures located behind the target, debris cloud fragments velocity, and damage extension of the targets. Furthermore, the self-healing of the ionomer layers was checked, and video capturing of the tests was performed. All this provides characterization of the multifunctional panel's behaviour and properties under high velocity impact.

At the beginning of the chapter, in section 4.2, the instruments used in the experiments are presented and briefly described. Then, in the following section details about the experimental set-up together with the performed measurements are given. Finally, obtained experimental results are presented and discussed. In the experimental results a comparison of protection capability between the ionomer and aluminium plates is given in section 4.4.1. Then few preliminary tests by which the self-healing of the ionomer in a multifunctional structure is assessed are presented. In section 4.4.3. the momentum transfer and debris cloud velocity is analysed for each configuration from section 3.6., and comparison among configurations is done. Damage measurements are described and provided in section 4.4.4. Finally, in section 4.4.5., remarks on the self-healing of the impacted samples are given.

4.2. Instrumentation

Different instruments/systems were used to carry out experimental tests and investigate the samples behaviour. In this section the instrumentation or systems used for experimental investigation are presented. This includes: two-stage light-gas gun, ballistic pendulum, ultrasound flaw detector, and high-speed video camera.

4.2.1. Light-gas gun

The impact experiments were performed at the Centre of Studies and Activities for Space (CISAS) impact facility, by means of a two-stage light-gas gun (LGG) [[40], [41], [42]], shown in Figure 4.1.

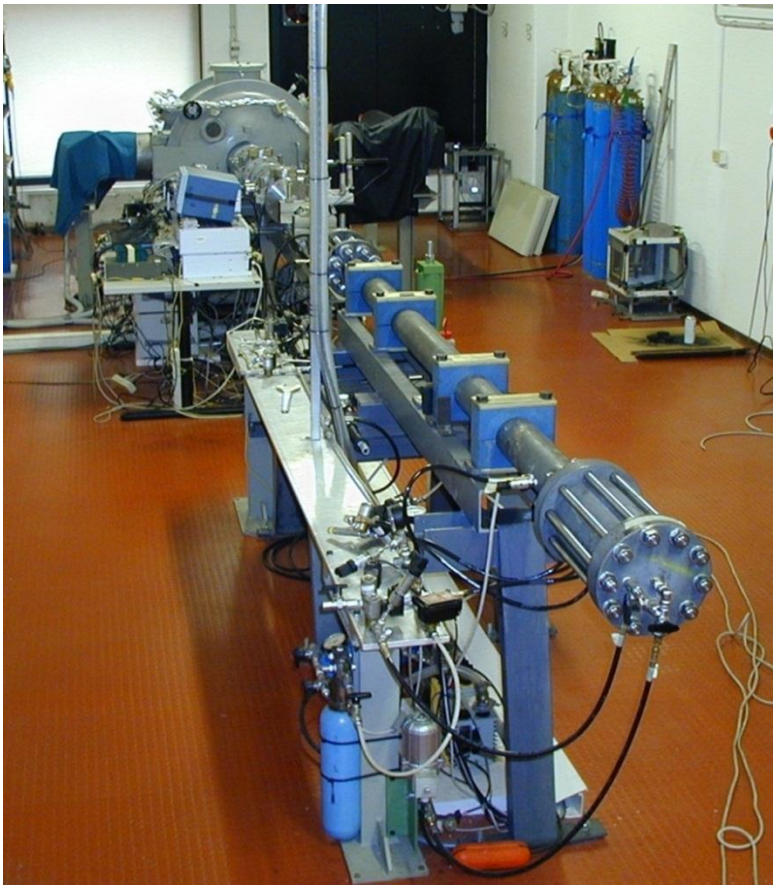

Figure 4.1 Two-stage light-gas gun at the CISAS impact facility.

With the CISAS light-gas gun projectiles up to 100 mg can be accelerated to the velocity of 6 km/s. An advantageous capability of this gun is also its high shot frequency. Namely, taking into account also the time needed for replacing the target set-up and for pumping down the vacuum chamber housing the target it can perform more than ten shots per day. This is possible through the use of a complex system, in which high pressure gas is used as a piston driver, and custom fast valves

separate the first stage from the pump tube and the pump tube from the barrel. Figure 4.2 shows the scheme of the CISAS two-stage light-gas gun.

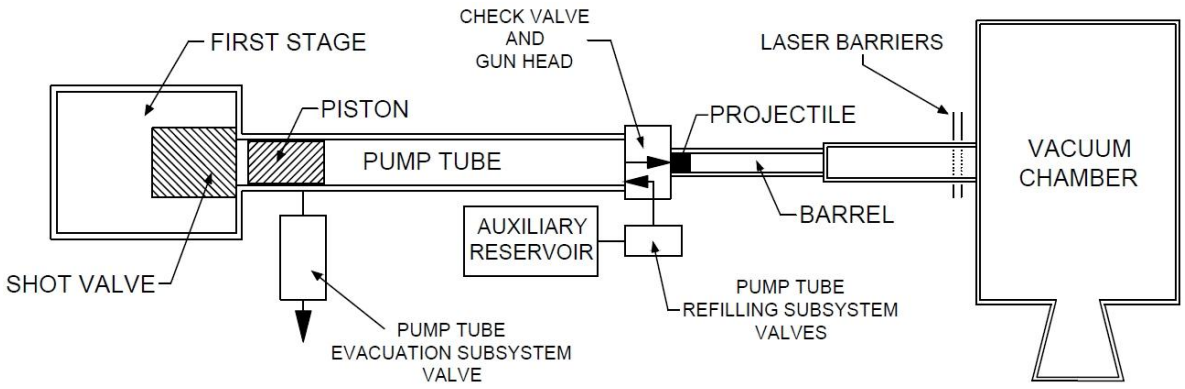

Figure 4.2 CISAS light-gas gun schematic [41].

The volume of the first stage reservoir is 3 dm^3. The second stage has a length of 3 m and its internal diameter is 35 mm. The launch tube is long 1.5 m. Launch tubes with different internal diameters can be used. In this study launch tubes with a x mm and x mm diameter were employed.

A typical shot procedure begins with high-pressure gas (200 bar) stored in a first stage reservoir of the gun. The gas from the first stage is then discharged onto the back of the piston in the second stage. This is done by the opening of a fast pneumatic valve (shot valve) between the first and second stage of the gun. Through the action of the gas from the first stage the piston is pushed along the pump tube, and it compresses the gas in the second stage. The pressure of the gas in the second stage raises from 0.3-0.4 bar to 5-6000 bar, while the temperature reaches approximately 10000 K. The hot, high-pressure gas is then canalised in the launch tube on the back of the projectile through an automatic spring valve (check valve). The piston stops few millimetres from the gun head and starts moving back toward the first stage, thus compressing the gas from the first stage. Since this compressed gas makes the piston bounce back toward the gun head and most of the gas in front of the piston is exhausted into the barrel, it becomes possible that the piston impacts the gun head. In order to avoid this from happening, an active damping process is provided by an external fast electronic device.

The damping process consists of three procedures [41]:

1) Refilling the pump tube in front of the piston with high pressure helium
2) Closing the shot valve to reduce the gas amount that pushes the piston toward the gun head
3) Evacuation of the pump tube behind the piston

This damping process prevents the piston from striking the gun head on the second coming (i.e. after the second bounce), and allows the piston to achieve its initial position at the base of the pump tube.

The shot valve is a fast depression valve, and its properties are: opening time 2 ms, gas pressure 200 bar, and flow area 35 mm^2. The check valve is an automatic spring valve, designed to open at adjustable pressure values (100-1000 bar) and to survive very high pressure (5000-6000 bar) and temperature (10000 K) [40].

The target set-up is placed in the vacuum chamber. Two optical barriers, placed in front of the vacuum chamber, detect the projectile pass before it enters the chamber and send signals to the computer, which makes possible to calculate the impact velocity. Furthermore, the vacuum chamber contains several appropriate apertures made of transparent glass to enable the use of lamps and high speed video camera.

The gun is entirely controlled by means of a PC and a dedicated electronic unit, which receives signals from four pressure transducers and controls an oscilloscope and nine electron valves [40]. A management system of the gun is completely automatic, and it is shown in Figure 4.3.

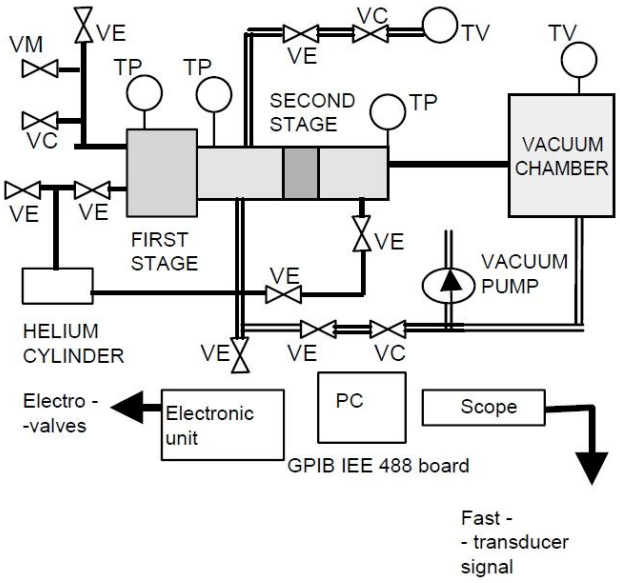

Figure 4.3 Gun management system (VE-electronic valves, VM-manual valves, VC-check valves, TP-pressure transducer, TV-vacuum transducer) [40].

4.2.2. Ballistic pendulum

In this work the ballistic pendulum was used to assess the protection capability of the impacted targets by measuring its displacement. Researchers used the ballistic pendulum to measure the momentum of the fragments and target in a ballistic or hypervelocity impact [[43]-[46]].

The ballistic pendulum is a single degree of freedom oscillating mass. It is composed of an oscillating mass suspended on flexural springs and of a ‘‘Witness plate’’ (WP) mounted on the oscillating mass (see Figure 4.4).

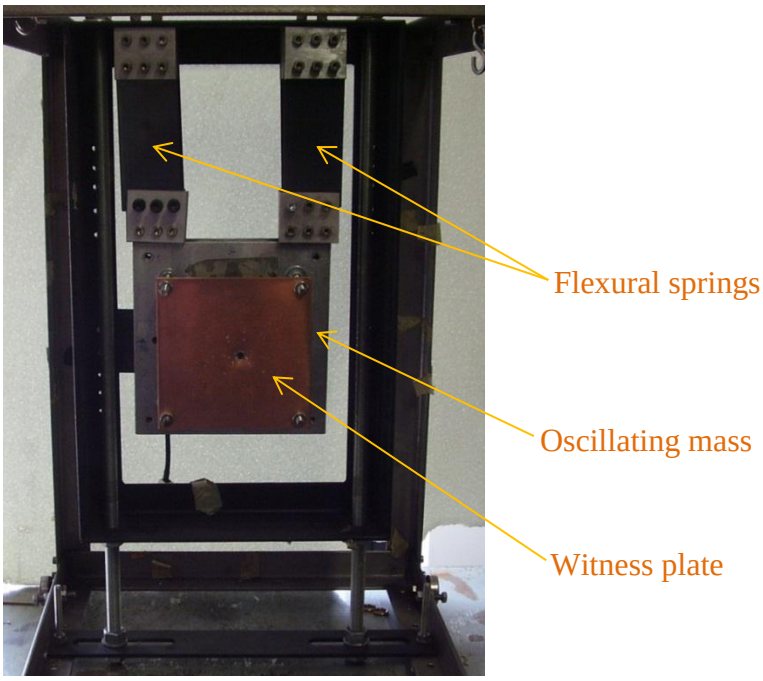

Figure 4.4 Ballistic pendulum with the witness plate.

The pendulum was placed behind the target sample at a fixed distance. When the impacting projectile has enough energy to perforate the target, a debris cloud that travels in the projectile direction is generated from the target's back face upon impact. This debris cloud then impacts on the witness plate causing the pendulum displacement in the *x* direction, according to Figure 4.5. This displacement gives indirect information on the damage potential of the fragments in the debris cloud ejected from the target's back face upon impact, which in turn provides information on the target protection capability.

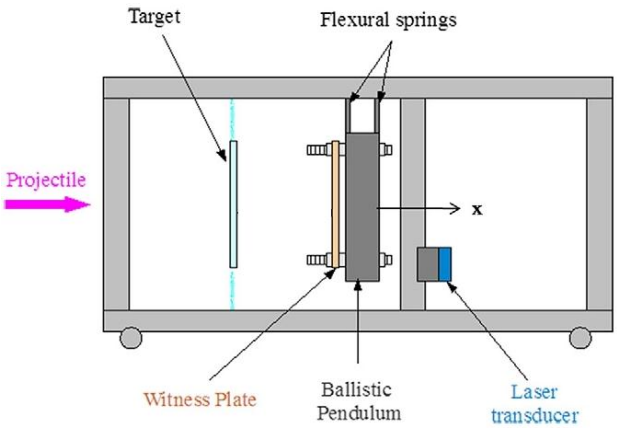

Figure 4.5 Target, witness plate and pendulum relative positions.

The pendulum used in this work was developed in [46]. The system is suspended in such a way that the first natural mode is the translation motion in the direction of the projectile path and all the other modes occur at much higher frequencies. This is achieved by hanging the oscillating mass by four

flexural (torsionless) supports (e.g. thin steel plates) in parallel connection. The displacement of the pendulum is measured by means of an optoelectronic displacement sensor.

The impact of the debris cloud on the WP causes the pendulum to gain an initial velocity in the *x* direction (Figure 4.5), and consequently, the pendulum starts moving the velocity vector direction. When the pendulum velocity is reduced to zero, due to the deformation resistance of the flexural springs, its initial kinetic energy is converted into elastic energy of the flexural springs. This can be expressed through the following energy conservation equation:

$$\frac{1}{2} m_{pend} v_{pend}^2 = \frac{1}{2} k_{pend} x_{pend}^2 \tag{4.1}$$

where m_{pend} is the pendulum mass, v_{pend} the pendulum initial velocity (acquired when the debris cloud impacts on the pendulum WP), k_{pend} the flexural stiffness of the suspension system, and x_{pend} the pendulum maximum horizontal displacement. From equation (4.1) v_{pend} can be expressed as:

$$v_{pend} = x_{pend} \sqrt{\frac{k_{pend}}{m_{pend}}} = x_{pend} \cdot 2\pi f_{pend} \tag{4.2}$$

where f_{pend} is the pendulum main oscillation frequency. Using the above equation, the momentum transferred to the pendulum (Q_{pend}) is:

$$Q_{pend} = m_{pend} v_{pend} = m_{pend} x_{pend} 2\pi f_{pend} \tag{4.3}$$

We see from equation (4.3) that the momentum transferred to the pendulum is proportional to its displacement in the *x* direction. Hence, it can be calculated from the measurement of the pendulum maximum displacement. Due to real effects occurring during hypervelocity impact testing, the pendulum behaviour can differ from the ideal one in equation (4.3). Among these effects the most interfering are the propellant gas blast and the vibration of the light-gas gun structure (recoil). These two effects were experimentally evaluated by running few light-gas gun tests in which empty sabots were launched. Since no projectile reaches the target, the resulting pendulum displacement is related only to the combined effects of gun blast and recoil. The average value of these measurements was used as light-gas gun background noise with respect to pendulum displacement measurements.

The pendulum displacement was read from the acquired signals by means of a MATLAB script file provided by [53]. The pendulum mass was equal to 3.6 kg and its frequency was 7.6 Hz. Those values were used for the calculation of the pendulum momentum, which is used for comparison purposes between different targets.

4.2.3. Ultrasound flaw detector

Phased array (PA) ultrasonic technology was used to detect delamination in the impacted samples [[47], [48], [49]]. Delamination is a damage mode characteristic to composite materials [50]. It manifests as detachment (crack) between layers in a composite laminate. Even if there is no visible damage on the external faces of the composite, delamination may be present inside the laminate, as a consequence of an load action. Because this crack cannot be seen by visual observation, phased array ultrasonic technology is used to inspect the presence and extent of delamination in impacted samples.

Phased array systems are applied for weld inspection and crack detection in a number of industries, such as aerospace, power generation, petrochemical, pipeline construction and maintenance, structural metals, and general manufacturing [47].

The main feature of phased array ultrasonic technology is the computer controlled excitation (amplitude and delay) of individual elements in a multielement probe [49]. The individual wave fronts can be delayed in time and synchronized in phase and amplitude,in such a way as to create a beam. Controllable excitation of individual elements enables beam steering and focusing, and it also improves the effective sensitivity.

Phased array probes for industrial non-destructive testing (NDT) are usually constructed around piezocomposite materials, which consist of many very small and thin rods of piezoelectric ceramic embedded in a polymer matrix. The composite strip is divided into a number of electronically separate elements by a segmented metal plating. Each separate element can be pulsed individually. The segmented element is incorporated in a probe assembly that includes a protective matching layer, a backing, cable connections and a housing, as shown in Figure 4.6 [47].

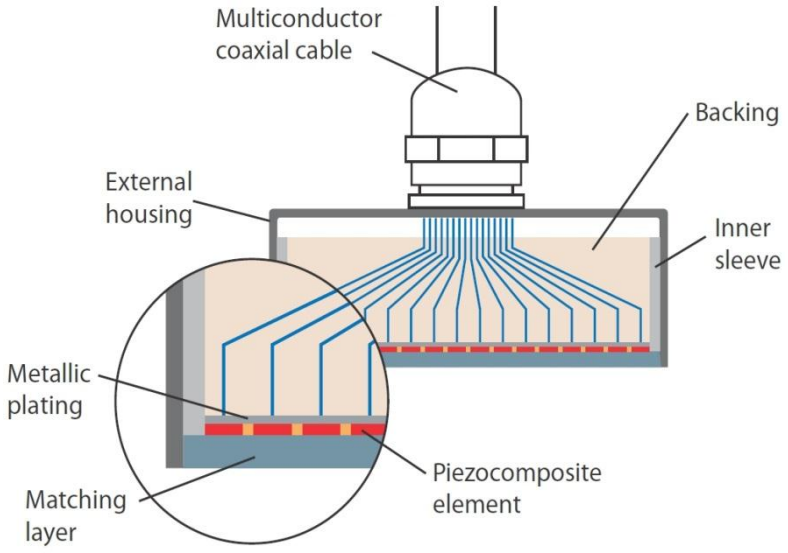

Figure 4.6 Phased array probe cross-section [47].

Figure 4.7 illustrates the working principles of the piezoelectric transducer element. The application of a voltage on the piezoelectric transducer element causes its compression in the direction perpendicular to its face. Upon voltage removal (usually less than a microsecond later) the element springs back, thus producing an ultrasonic wave. This process can go also in the opposite direction, i.e. if the element is compressed by the pressure of an arriving ultrasonic wave, voltage is produced across its face. Therefore such an element can both transmit and receive ultrasonic pulses.

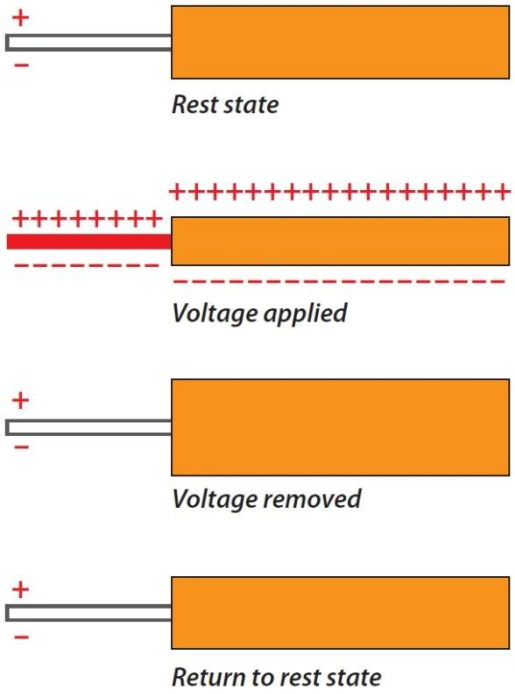

Figure 4.7 Principle of the piezoelectric transducer element [47].

The basic functional properties of phased array probes are its type, frequency, number of elements and size of elements. According to the probe type they differ in the way they are used, and can be used with a plastic wedge, in direct contact or in immersion. The transducer frequencies are usually in the range from 2 MHz to 10 MHz. Penetration increases with lower frequencies, while with higher frequencies there is an increase in resolution and sharpness. The number of elements composing a phased array probe can vary from 16 to 256. They can be arranged in various shapes, as linear array, 2D matrix, annular array, circular array, or some other shape.

As mentioned previously, the impacted targets were also inspected with the PA flaw detector for delamination detection and assessment. In order to achieve optimal conditions for sample inspection, due to the amount of damage suffered by the targets and the relatively high sound attenuation of the composite, several considerations on the inspection set-up have been made.

The tested samples exhibited detachment of the superficial layers, especially the CFRP targets, and had fibres sticking outward from the sample's hole area, which was more prominent for the

Twaron/CFRP/Twaron samples. This prevented direct contact between the probe and the samples, since adequate contact was not attainable due to damage caused irregularities on the sample's surface. For the same reasons, usage of the wedge with the probe was also discarded. Finally it was decided that the inspections would be performed in immersion, where the target and probe were immersed in water, and the probe was held at a fixed distance above the target surface.

Probes with frequency of 2.5 MHz, 5.0 MHz and 10.0 MHz were tried and compared. In practice, resolution and focal sharpness increase with higher frequency, while penetration in any test material (due to material attenuation) decreases with increase in frequency. Relatively high attenuation of the sound wave was observed for the inspected composite samples, as shown in Figure 4.8 (a), in which the target bottom is barely visible and also the delamination is difficult to detect in deeper regions. Anyway, no significant difference between the three probes due to wave attenuation was observed, while better resolution was obtained with higher frequency. Therefore, the probe of 10.0 MHz was selected for all the inspections. Even if sound attenuation in the inspected composite material is high, the similar attenuation observed between the three frequencies is probably due to the small thickness of the samples.

In order to alleviate the effects of ultrasound wave attenuation and scattering through the thickness of the samples, caused by the composite structure and material, a Time-Corrected-Gain (TCG) option available within the PA flaw detector system was used. The TCG option increases the gain linearly with increasing distance from the probe, therefore this permits improved ‘‘visibility’’ in the deeper regions from the ultrasound wave entrance surface in the target (Figure 4.8 (b)).

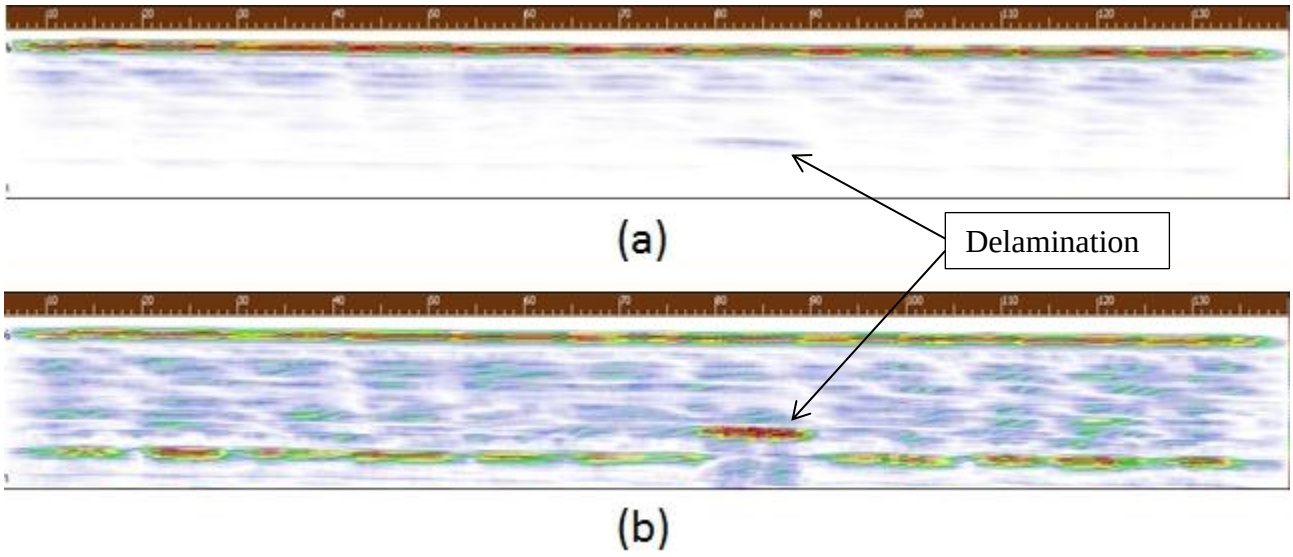

Figure 4.8 Cross-sectional view of panel C after impact: a) no TCG was not applied, and b) TCG was used.

4.2.4. High speed video camera

The Phantom high-speed video camera was used to capture the impact phenomenon in the performed tests. With the high-speed camera and the accompanying software, the velocity of the fragments in the debris cloud was measured [51]. Two velocities were measured: that of the fastest fragment moving in the horizontal direction and that of the biggest fragment (if such fragment was present) moving also in the horizontal direction, as shown in Figure 4.9. For the biggest fragment it was tried to select the remnant of the projectile if it was visible and somewhat bigger than the other fragments in the debris cloud.

The following settings for the high-speed video camera acquisition were used:

- Resolution: 256 x 152
- Sample rate (fps=frames per second): 66037 fps (Period: 15.14 μs)
- Exposure (μs): 4.0

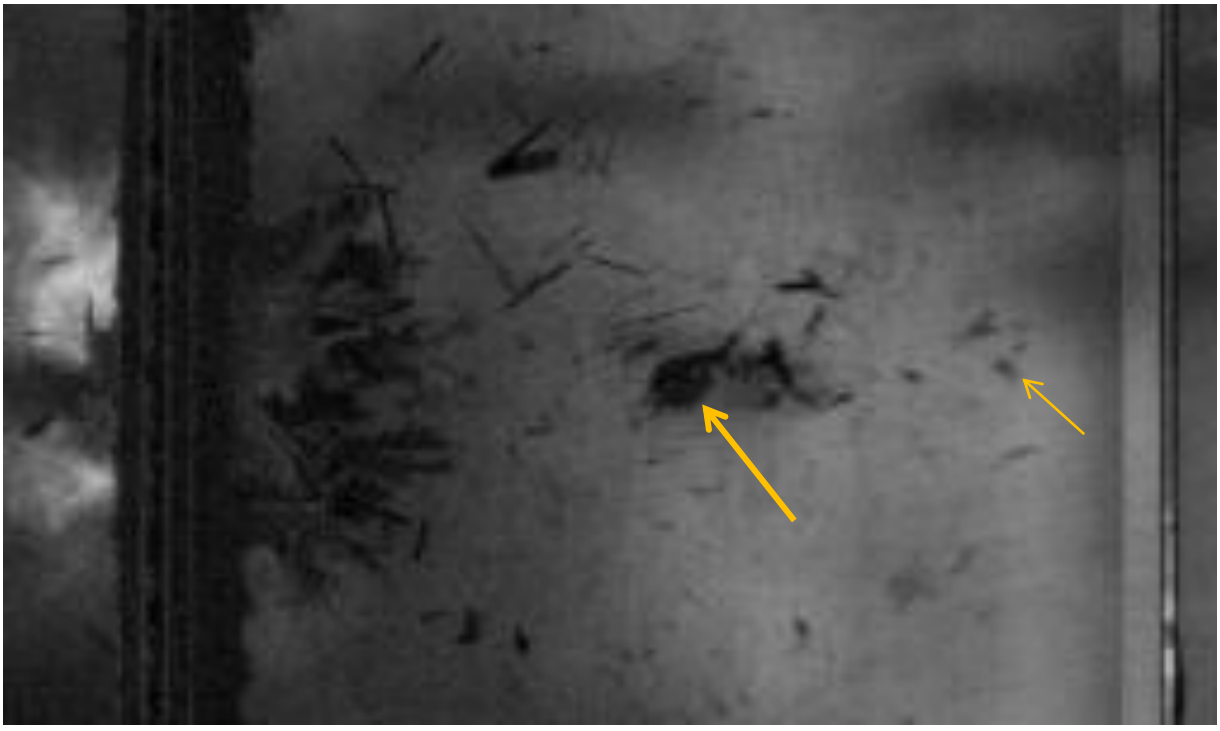

Figure 4.9 The fastest and biggest fragment in the debris cloud. The bigger arrow indicates the biggest fragment, while the smaller one indicates the fastest fragment.

4.3. Experimental set-up and measurements

All the experimental tests were carried-out at the CISAS impact facility. The impact tests were done by means of a two-stage light-gas gun. Spheres made of Aluminium 1100 were used as projectiles. Impacts with varying projectile size and velocity were performed. The impact velocity ranged from approximately 1 km/s to 4 km/s, with a majority of the tests being from 2 km/s to 2.5 km/s. The

projectile diameter was in the range from 1.5 mm to 5.6 mm. Anyway, in each section, where a specific study is presented, details about projectile speed and diameter are given. The targets were suspended by means of elastic springs which were attached to a stationary frame, as shown in Figure 4.10. The target parts were held together by aluminium support plates, see Figure 4.10. Through bolts action the supporting plates press on the target front and back face on to the upper and lower boundary, thus keeping the assembly together. Behind the target a copper witness plate mounted on the ballistic pendulum was located (Figure 4.10). A high-speed camera was also employed to capture the impact tests and to provide more insight in the tests. The high-speed camera was not available for all tests, and therefore it was not used in all of them.

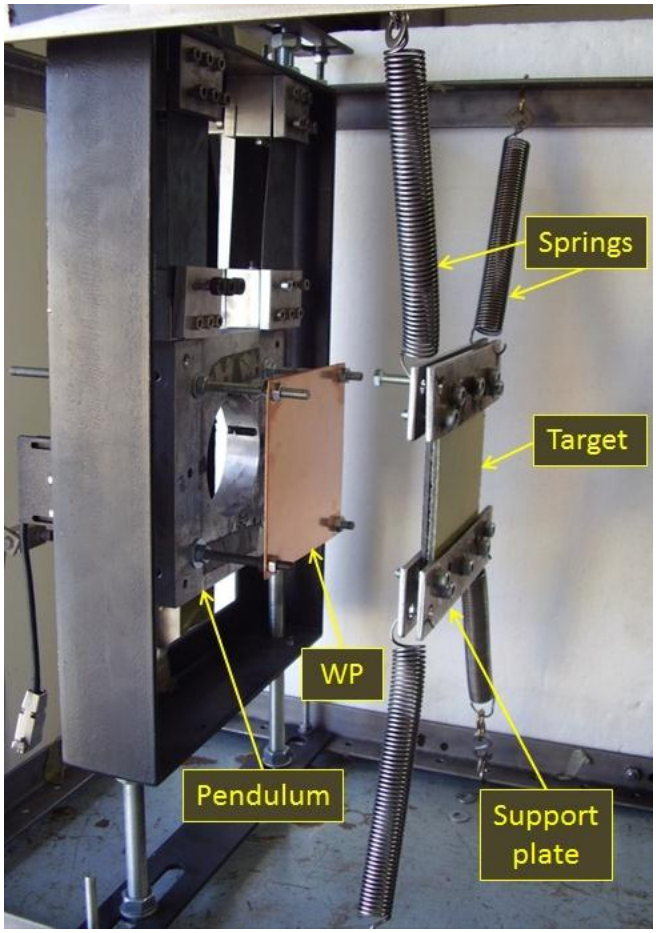

Figure 4.10 Target support, and the witness plate (WP) on a ballistic pendulum.

The following data sets related to the impact tests were collected and are presented in various sections:

- momentum transferred to the witness plate
- velocities of the fastest and biggest fragments in the debris cloud
- damage on the target samples
- damage distribution on the witness plate

- self-repair of the hole in the ionomer layer

The momentum transferred to the witness plate was determined by the displacement of the ballistic pendulum. The velocities of the biggest and fastest fragment are estimated from the videos of the high-speed camera. The damage on the targets was assessed after the impact by visual inspection and an ultrasound flaw detector. Visual inspection was concerned with the visible damage on the surface of the samples and in the hole region. The visible damage was measured with a caliper. A phased array ultrasound detector was used for the inspection of delamination in the interior of the samples. Damage on the witness plate provides indirect information on the size distribution of the fragments in the debris cloud. The self-healing of the impact caused hole in the ionomer layer was checked by visual inspection.

All of the above data characterize the sample's behaviour under impact loading. In the post impact analysis all data relative to each shot was tabulated and are presented in the following sections.

4.4. Experimental results and discussion

A vast campaign of experimental tests was performed. First the self-healing ionomer properties as a bumper were investigated and compared to that of aluminium. Then the ionomer was coupled to a structural panel to investigate its self-healing capability when applied in a multilayer assembly, and to investigate the possibility of applying it in a multifunctional system as presented in chapter 3. Thereafter, configurations of panels A, B and C (see section 3.3) were subjected to testing and the results are reported in the present section. Firstly, the single layers were tested and evaluated individually; then, two layer multifunctional configurations were tested and evaluated; and finally, several tests on three layers configurations were performed, and the results are compared to all previous configurations. The resulting damage of the panels is also discussed and quantified. Lastly, the self-healing results of the multifunctional panels are discussed.

4.4.1. Self-healing ionomer versus aluminium bumpers

The protection capability of the ionomer samples is compared to that of aluminium alloy bumpers with similar areal density. The aluminium used is Al7075-T6. The protection capability was assessed by looking at two complementary data sets regarding the witness plate, namely, the extent on the witness plate of craters produced by the impact of the debris cloud and the amount of momentum transferred to the witness plate by the debris cloud. Both aspects provide indirect information on the debris cloud potential to damage structures on its flight path. Moreover, they should decrease when the target protection capability increases.

The witness plate craters area was measured from high-resolution (600dpi) images of the witness plates by means of an image analysis code developed in MATLAB® [52], while the momentum transfer was assessed by using the ballistic pendulum.

The test matrix is reported in Table 4-1. As reported in the table, incomplete self-healing occurred only in one sample. Figure 4.11 shows test's 8813 target sample and witness plate. The crater on the witness plate indicates that the bumper was perforated, but no hole was present on the ionomer.

Table 4-1 Test summary for hypervelocity impacts on ionomer and aluminium targets.

Shot No.	Target		Projectile		Perforation (Yes/No)	Hole closure (Yes/No)
	Material	Thickness (mm)	Diameter (mm)	Velocity (km/s)		
8813	Surlyn®	2.0	1.5	1.93	Yes	**Yes**
8829	Surlyn®	3.0	1.5	1.80	Yes	**Yes**
8833	Surlyn®	5.0	1.5	1.64	No	**Yes**
8836	Surlyn®	5.0	1.5	4.10	Yes	**Yes**
8838	Surlyn®	3.0	1.5	4.00	Yes	**Yes**
8839	Surlyn®	2.0	1.5	3.90	Yes	**No**
8841	Al7075-T6/3	1.5	1.5	1.34	No	**No**
8842	Al7075-T6/3	0.8	1.5	2.64	Yes	**No**
8843	Al7075-T6/3	0.8	1.5	1.37	Yes	**No**
8844	Al7075-T6/3	1.0	1.5	1.28	Yes	**No**
8845	Al7075-T6/3	1.5	1.5	3.70	Yes	**No**
8846	Al7075-T6/3	1.0	1.5	4.05	Yes	**No**
8847	Al7075-T6/3	0.8	1.5	4.05	Yes	**No**
8848	Al7075-T6/3	1.0	1.5	2.64	Yes	**No**

In Figure 4.12 and Figure 4.13 scanning electron microscope (SEM) micrographs of the front and rear side of shots 8813 and 8839 are shown, respectively. From Figure 4.12 it can be observed that a molten circular zone with a diameter approximately equal to that of the projectile is present in the impact zone. In the damaged area around the visible hole in Figure 4.13 spallation occurred, thus damaging the material, and removing a bigger amount of material from the impact area, which presumably hindered the self-reparation of the hole.

In Figure 4.14 the ratio of the total crater area (A_{tot}) and specific area (A_{sp}) is plotted. The specific area is the bumper surface corresponding to a mass of 1 kg. The damage area A_{tot} is in fact proportional to A_{sp}, since the specific area is the inverse of the surface density and the lower the surface density the higher the amount and speed of ejecta reaching the witness plate. In Figure 4.14

the total crater area increases more than linearly with the impact speed for the aluminium and the ionomer, but the increasing slope is steeper for the aluminium. It can be also observed that at highest impact velocities the ionomer bumper seems to produce less debris. This is probably due to the fact that with increasing speed increases also the amount of the target material that goes in the debris cloud, but such material is less dangerous if it has a low density, as it is with ionomer compared to aluminium.

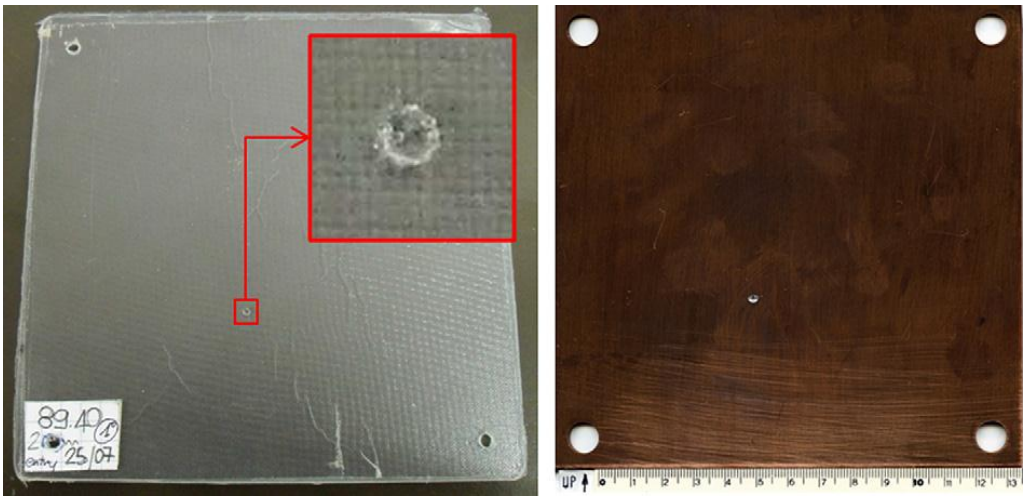

Figure 4.11 Test no. 8813: perforated and rehealed ionomer bumper (left) and witness plate craters (right).

In Figure 4.15 the momentum transferred to the pendulum (Q_{pend}) is plotted against the projectile momentum (Q_p). A tentative trend for the aluminium samples is also plotted, showing large data scattering due to the limited number of tests. The uncertainty in the momentum estimation is reported by error bars, while the horizontal line refers to the light-gas gun noise. It can be seen from the figure that, for both the ionomer and aluminium, the momentum transferred to the ballistic pendulum by the debris cloud increases more than linearly with the impact speed. The increasing trend is again steeper for aluminium than for the ionomer.

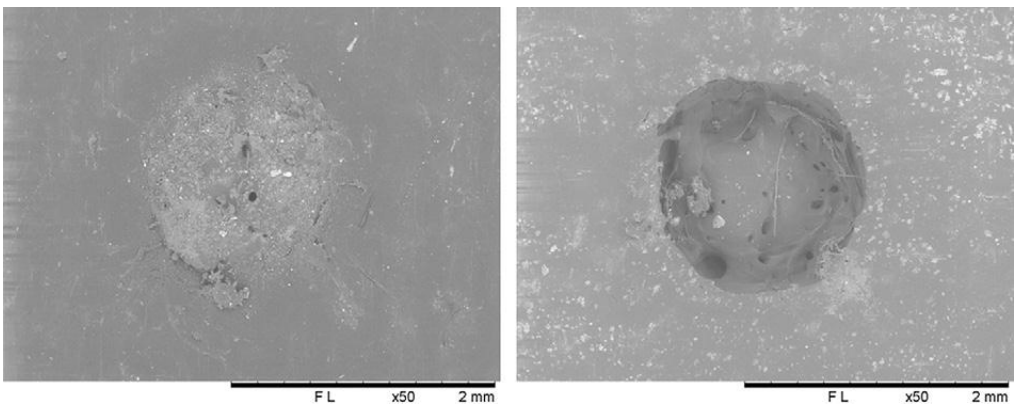

Figure 4.12 Test no. 8813: SEM micrographs of the impact zone on the target front (left) and rear (right) face [Courtesy of Politecnico di Milano].

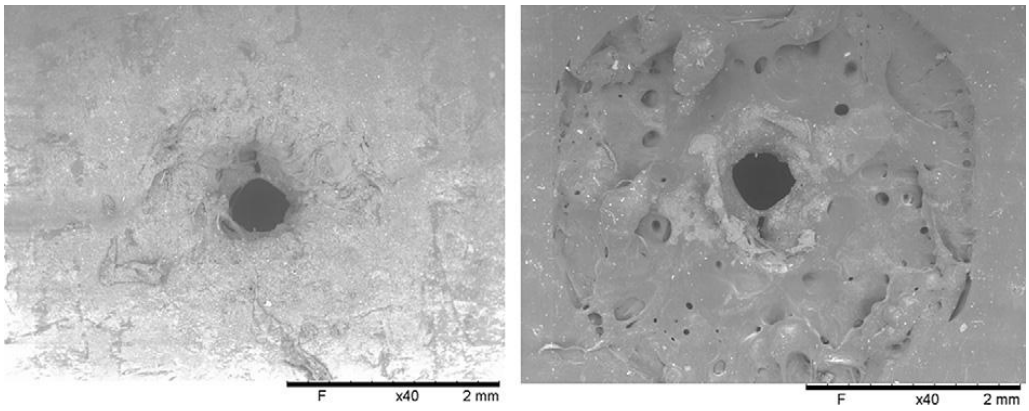

Figure 4.13 Test no.8839: SEM micrographs of the impact zone on the target front (left) and rear (right) face [Courtesy of Politecnico di Milano].

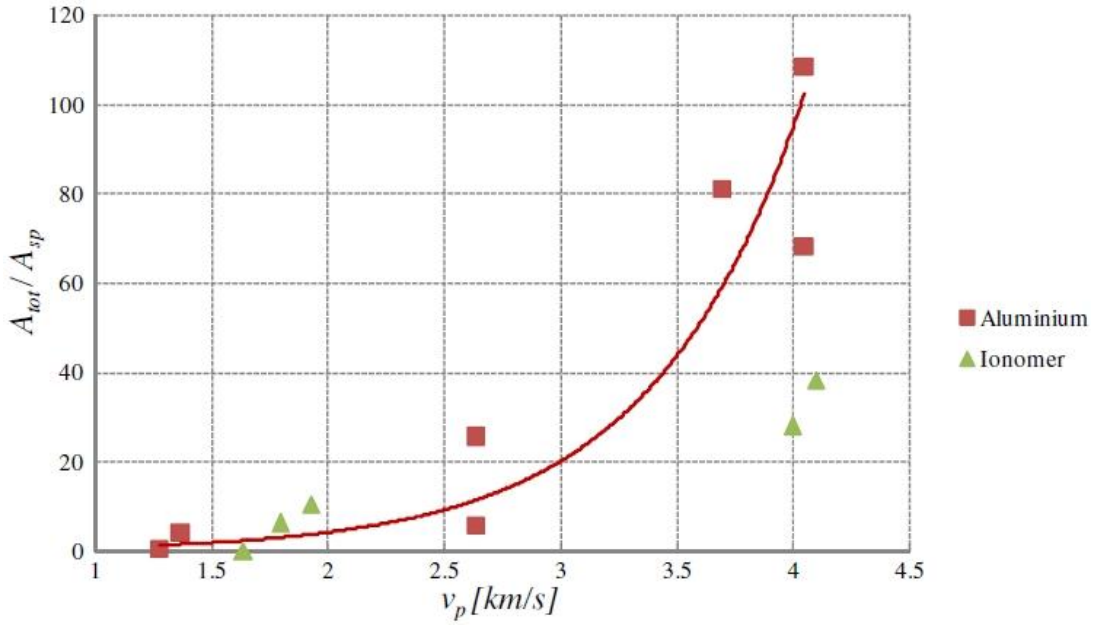

Figure 4.14 Witness plate total crater area divided by the bumper specific area [54].

Even if Figure 4.14 and Figure 4.15 indicate higher protection capability of the ionomer, it has to be considered that the damaging potential of the debris cloud is highly dependent from the size and speed of its biggest fragment. This means that a debris cloud made of one big fragment is much more dangerous than a cloud with the same total mass consisting of many tiny dispersed particles. Therefore, the area of the largest crater on the witness plate (A_{max}) divided by the specific area of the bumper is plotted in Figure 4.16. We can see that A_{max}/A_{sp} for the ionomer is increasing more than for the aluminium, with speed increase. Furthermore, for aluminium bumpers the protection capability begins to increases after approximately 3 km/s. For ionomer bumpers values of A_{max}/A_{sp} exceed those of aluminium bumpers even when the total crater area (A_{tot}/A_{sp}) is lower. This means that fragments in the debris cloud are better fragmented for aluminium bumper than for ionomer bumpers. In fact, by observing the witness plates after the tests (see Figure 4.17), it is clearly visible

that the debris in the cloud are better fragmented and dispersed after impacts on aluminium targets compared to ionomer bumpers, as indicated previously also by Figure 4.16.

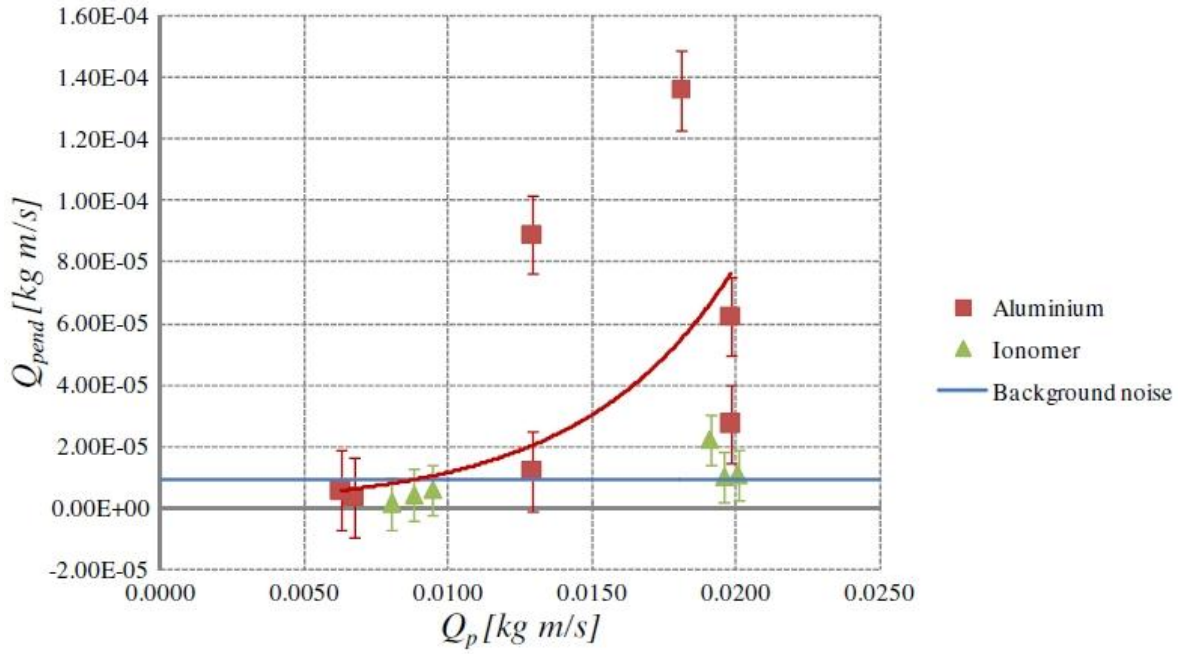

Figure 4.15 Momentum transfer to the witness plate mounted on the ballistic pendulum and located behind the target [54].

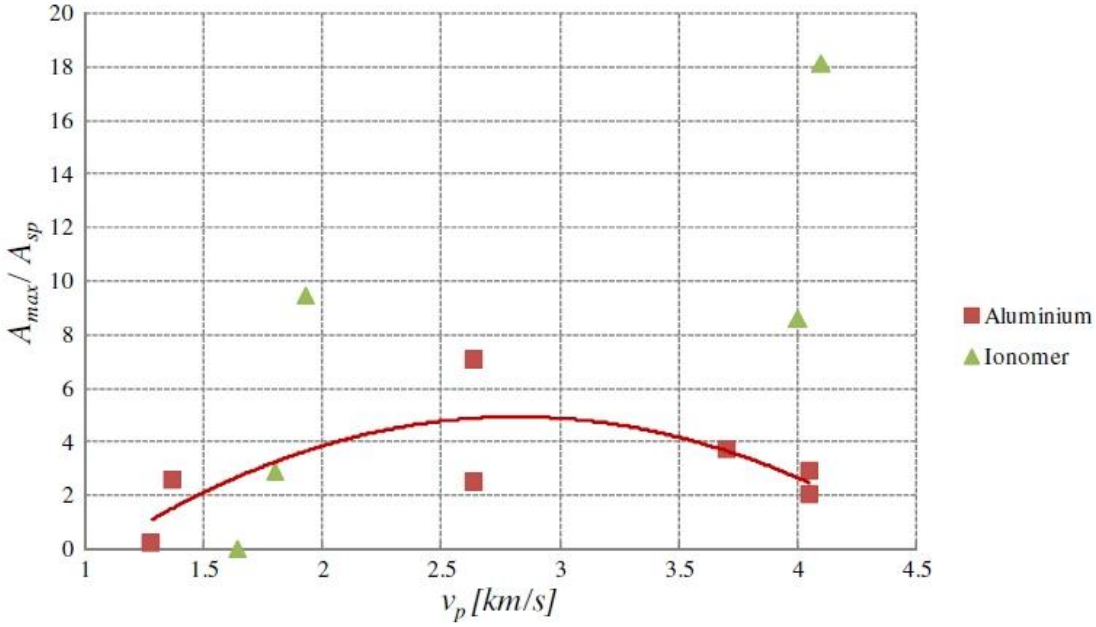

Figure 4.16 Area of the largest witness plate crater divided by the target specific area [54].

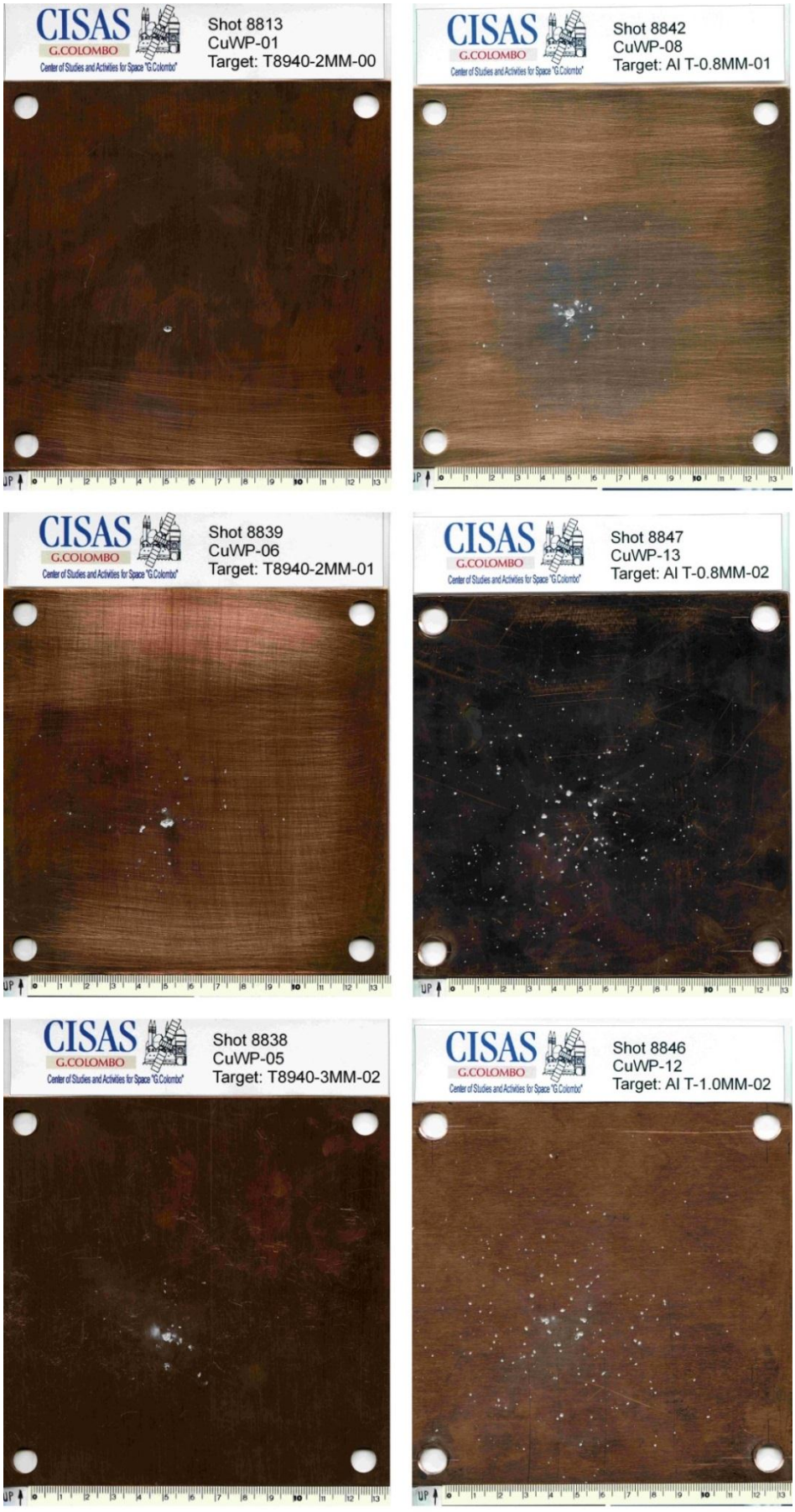

Figure 4.17 Witness plate damage comparison after tests on ionomer (3 samples on the left) and tests on aluminium (3 samples on the right). Each row of figures corresponds to similar impact conditions.

4.4.2. Preliminary multifunctional panel tests

In this part six preliminary tests, in which the self-healing of the ionomer is tested, are presented. The six samples consist of one woven CFRP structural layer attached to a self-healing ionomer layer. In three samples the CFRP layer is 1.1 mm thick, and in the other three it is 2.2 mm thick (see section 3.4.). The ionomer thickness is 2 mm in all samples. Impacts on CFRP and ionomer side were investigated. Moreover, three projectile diameters were used, namely, 2.3 mm, 3.5 mm and 5.6 mm. Impact velocities ranged from 940 m/s to 1200 m/s and are representative of ballistic impact. The test matrix is presented in Table 4-2.

Table 4-2 Test matrix. IDt is the target ID, t_{CFRP} is the thickness of CFRP layer; $t_{Ionomer}$ is the thickness of the Ionomer layer, v_p is the projectile velocity and d_p is the projectile diameter. P means complete perforation, and NP means no perforation.

Shot No.	ID_t	Target thickness		v_p (km/s)	d_p (mm)	t_t/d_p	Impact side	P/NP	Hole closure
		t_{CFRP} (mm)	$t_{Ionomer}$ (mm)						
8905	PP1	2.2	2.0	1.20	5.6	0.75	cfrp	P	**No**
8906	PP2	2.2	2.0	1.20	5.6	0.75	ionomer	P	**No**
8908	PP3	2.2	2.0	1.20	3.5	1.20	cfrp	P	**Yes**
8922	PP4	1.1	2.0	1.00	3.5	0.89	cfrp	P	**No**
8923	PP5	1.1	2.0	1.07	3.5	0.89	ionomer	P	**No**
8925	PP6	1.1	2.0	0.94	2.3	1.35	cfrp	NP	-

In Table 4-2 hole closure results are summarized, where it is reported if the impact resulted in a perforation of the panel and if complete hole closure occurred. Perforation of the target was labeled with “P”, while if no perforation occurred it was indicated with “NP”.

As reported in the table, in all impact tests except one the target was perforated by the projectile, but only in one case complete self-healing of the hole in the ionomer layer occurred. This clearly indicates that the ionomer self-healing ability is significantly reduced when used in a multilayer assembly as herein. Anyway, partial self-healing was observed in all samples. In Figure 4.18 the damage on the witness plate for shot 8908 clearly indicates that the target was perforated, but no hole was present. A scanning electron microscope image of the sealed hole is shown in Figure 4.19. A partially repaired hole for shot 8905 is shown in Figure 4.20.

Figure 4.18 Witness plate after test 8908. A black crater is visible on the WP.

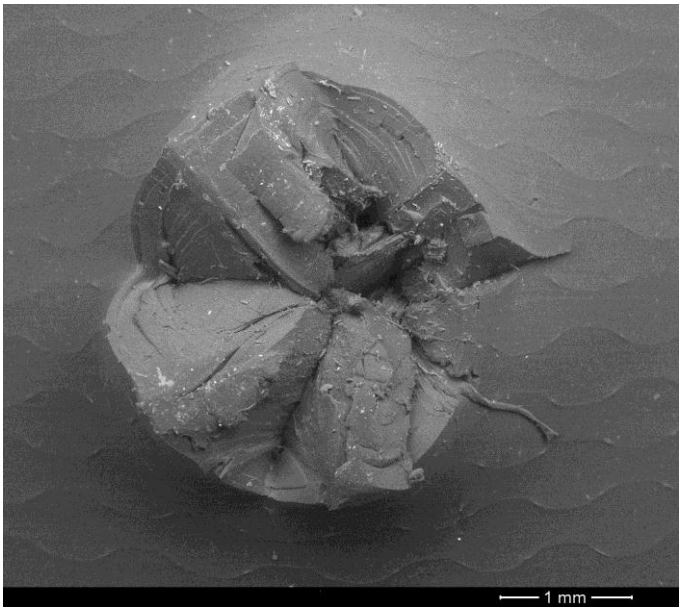

Figure 4.19 SEM micrograph of the successful self-healing of the hole in the ionomer layer after test 8908.

Figure 4.20 SEM micrograph of the un-repaired hole in the ionomer layer after test 8905.

Self-healing capability of the ionomer was further analysed by comparing the internal vs. external hole diameters on the ionomer. The external hole for the ionomer refers to the not damaged/re-solidified area limit, while the internal hole refers to the actual visible hole (see Figure 4.21). The ratio of those two diameters as a function of total target thickness and projectile diameter ratio (t_t/d_p) is plotted in Figure 4.22. The value of the ionomer internal and external hole ratio in a perforating shot can vary from 0 to 1.0, where 1 indicates no self-healing at all and 0 indicates complete hole closure. Even if sealing of the hole did not occur in most of the samples, it can be seen from Figure 4.22 that in all tests the internal hole diameter was less than 50% of the external hole diameter.

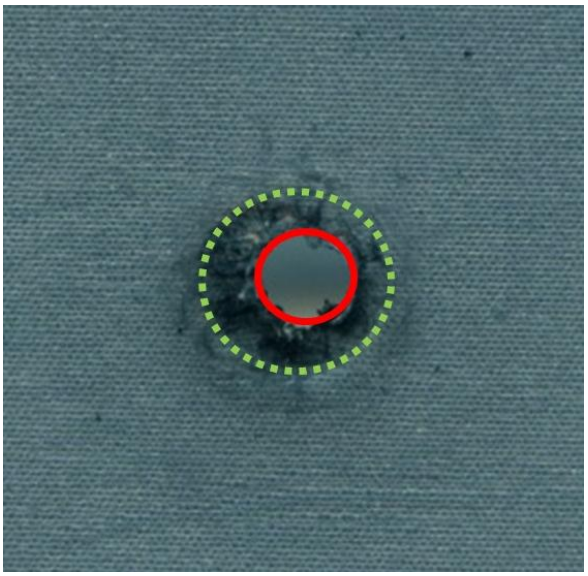

Figure 4.21 Example of ionomer internal (solid line) and external (dotted line) hole.

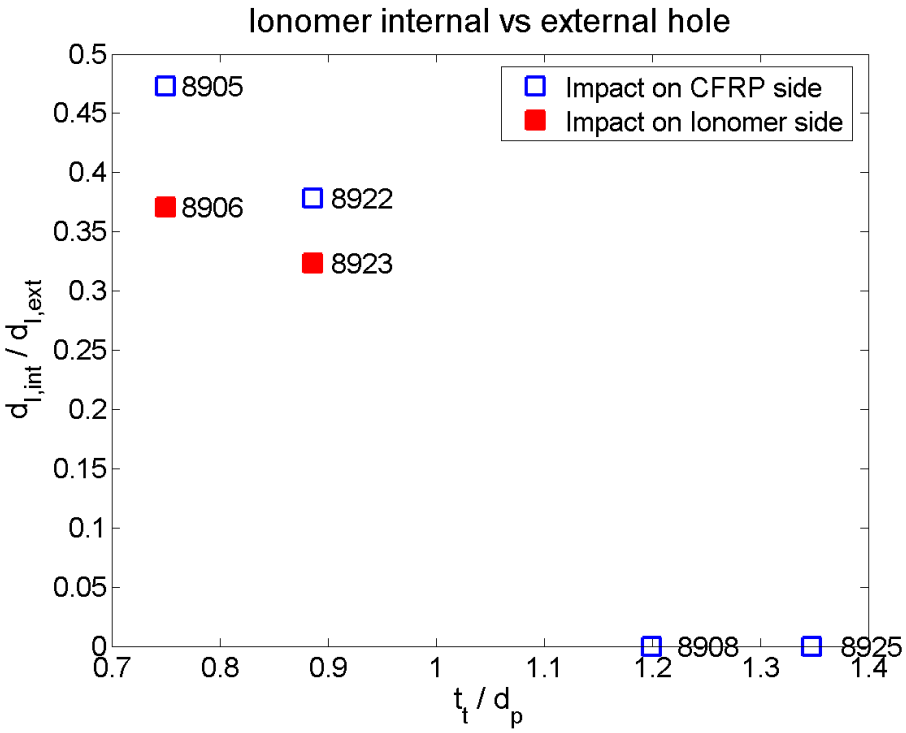

Figure 4.22 Self-healing ionomer capability investigated as a ratio between internal and external hole as a function of the target thickness to projectile diameter.

From shots 8905, 8906, 8922, and 8923 in Figure 4.22 it can be observed that the ratio of the hole diameters is slightly smaller for impacts on the ionomer side, which indicates lightly better healing ability of the ionomer when it is directly exposed to the impacting projectile. The ratio of the internal and external hole also decreased for higher t_t/d_p ratios, which is the difference between shots 8905 and 8922, and between shots 8906 and 8923. This difference is probably due to the larger percentage of ionomer in the total target thickness for the thinner target. Since the ionomer thickness is constant in all samples, it makes 50% of the thickness in the thicker sample and approximately 65% of the thickness of the thinner panel sample. This means that for higher t_t/d_p the ionomer thickness increases with respect to the projectile diameter.

It could seem contradictory to the above observations that among shots 8908, 8922 and 8923 the hole was sealed only in shot 8908. But since the impact velocity was not equal in those shots, it is believed that the increased projectile impact velocity favoured the self-healing in shot 8908, which results in 25% increase in projectile kinetic energy from shot 8923 to shot 8908.

Figure 4.22 indicates that two important parameters influencing the ionomer healing performance in the assembly are its location with respect to the impacted side and its thickness.

4.4.3. Momentum transfer and debris cloud velocity

In this section the test results regarding the momentum transfer to the witness plate, and the velocity of the fastest and biggest fragment in the debris cloud for single layers, two layers multifunctional panels, and three layers multifunctional panels are presented. First the single layer configurations were analysed, then a structural layer and the self-healing ionomer were joined together in a multifunctional assembly and impacted, and finally panels consisting of two structural and one ionomer layer were tested. Comparison among the various configurations is performed. For this purpose the measured quantities (momentum transfer, biggest fragment velocity and fastest fragment velocity) are divided with the specific area (A_{sp}) of the corresponding panel, since they are proportional to it. As mentioned previously, the specific area corresponds to the target surface with a mass of 1 kg (which is the inverse of surface density). The impact velocities in all the tests ranged approximately from 2000 m/s to 2500 m/s. Three diameters for aluminium spherical projectiles were used: 2.3 mm, 3.5 mm and 4.5 mm. All impacts were normal to the target, i.e. at 0° impact angle.

4.4.3.1. Single layers of the panel assembly

In this part results for panels A, B and C are given. Those three panels were tested individually. In Table 4-3 the performed tests are listed and the initial conditions regarding the projectile velocity and diameter are provided. The resulting momentum transfer to the pendulum and the velocity of the fastest and the biggest fragment in the debris cloud for each shot are also given in the table.

Table 4-3 Tests performed on single layer panel assemblies.

Shot number	Target	Part	Projectile diameter - d_p (mm)	Projectile velocity - v_p (m/s)	Target areal density (kg/m^2)	Fastest fragment velocity (m/s)	Biggest fragment velocity (m/s)	Transferred momentum (kg*m/s)
8980	KCK-02	C	3.5	2055	4.95	1172	1172	0.08840
8981	CFRP-01	A	3.5	2093	5.59	963	963	0.08150
8982	KCK-03	C	2.3	2151	4.95	728	668	0.02919
8983	CFRP-02	A	2.3	2102	5.59	540	442	0.02278
8984	KCK-04	C	3.5	2508	4.95	1437	1437	0.11643
8985	CFRP-03	A	3.5	2574	5.59	1293	1293	0.12616
8992	I-02	B	2.3	2109	1.90	-	-	0.02422
9044	CFRP-25	A	4.5	2254	5.59	1322	1322	0.21454
9045	KCK-22	C	4.5	2304	4.95	1526	1526	0.24033
9046	I-28	B	3.5	2382	1.90	1994	1994	0.10488
9047	I-29	B	4.5	2336	1.90	1964	1964	0.15020

In Figure 4.23 the momentum transferred to the witness plate divided by the specific area (Q_{pend}/A_{sp}) is plotted on the vertical axis for the single layers (A, B and C). On the horizontal axis values of projectile momentum (Q_p) is given. For the ionomer the momentum transferred in shot 9047 was not considered, because the projectile perforated the witness plate, thus not all the momentum is transferred to the witness plate. It can be observed that a straight line fits well the data, indicating a linear relation between the projectile momentum and the transferred momentum for the investigated range of projectile momentums. From Figure 4.23 it is also observed that for panels A and C $Q_{pendulum}/A_{sp}$ is similar. A small difference is noted between the two and it seems that with increasing projectile momentum the difference is slowly increasing. Anyway, the ionomer appears to transfer the least amount of momentum to the witness plate among the single layers.

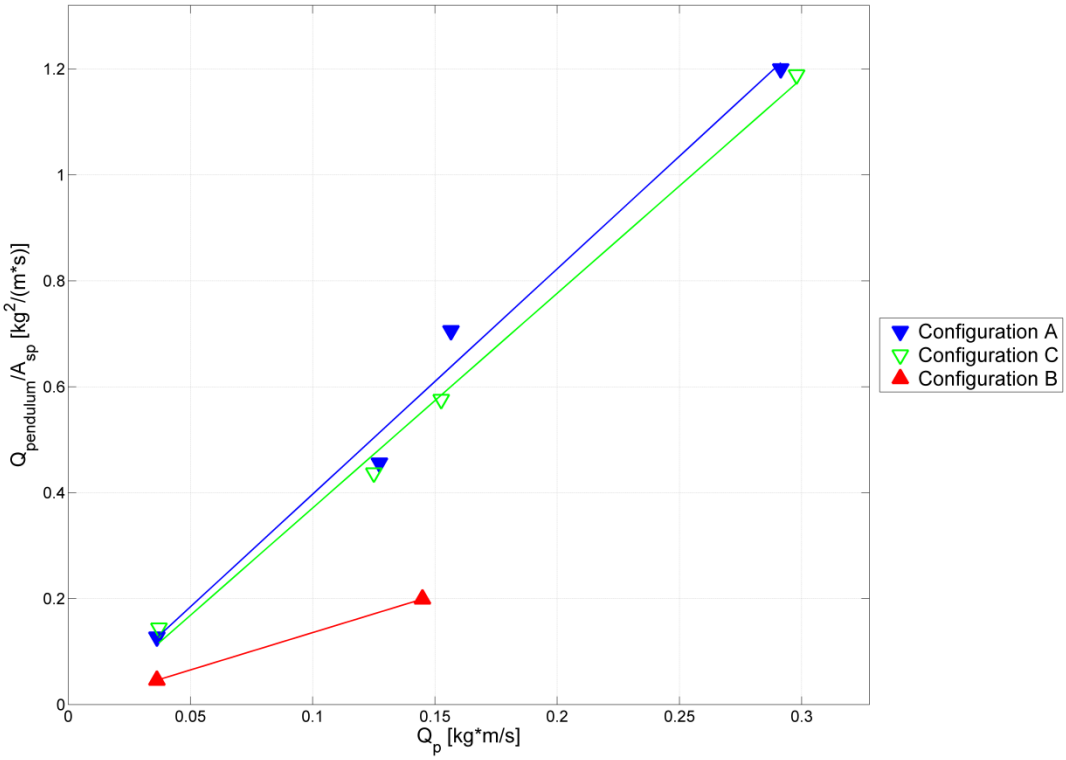

Figure 4.23 Momentum transfer to the ballistic pendulum divided by the target specific area for layers A, B and C.

In Figure 4.24 the velocity of the fastest fragment in the debris cloud (v_{ff}) divided with A_{sp} is plotted against the kinetic energy of the projectile, while the ratio of the velocity of the biggest fragment (v_{bf}) in the debris cloud and A_{sp}, as a function of projectile kinetic energy is plotted in Figure 4.25. Beside for the shots with the projectile diameter of 2 mm, the velocity of the biggest fragment is equal to the velocity of the fastest fragment (see also Table 4-3). This is because in those shots the biggest fragment is at the same time also the fastest. Therefore, there is a minor difference between

Figure 4.24 and Figure 4.25. A tentative fit to the data is plotted in the figures. From the figures a non-linear increase of the fastest and biggest fragment velocity with projectile kinetic energy is observed for panels A and C. The trend is steeper for lower energy impacts, and with increase in impact energy the steepness decreases. While for lower energies there is a little difference in v_{ff}/A_{sp} and v_{bf}/A_{sp} between panels A and C, they seem to become equal at higher impact energies. From the available data it is difficult to predict whether the velocities will remain equal or the velocities for panel C will become lower with respect to that for panel A. Only two velocities are available for the ionomer tests. For each of those tests the biggest fragment is also the fastest, and its velocity is almost equal in both tests. For the available data either v_{ff}/A_{sp} and v_{bf}/A_{sp} are much slower for panel B than for panels A and C.

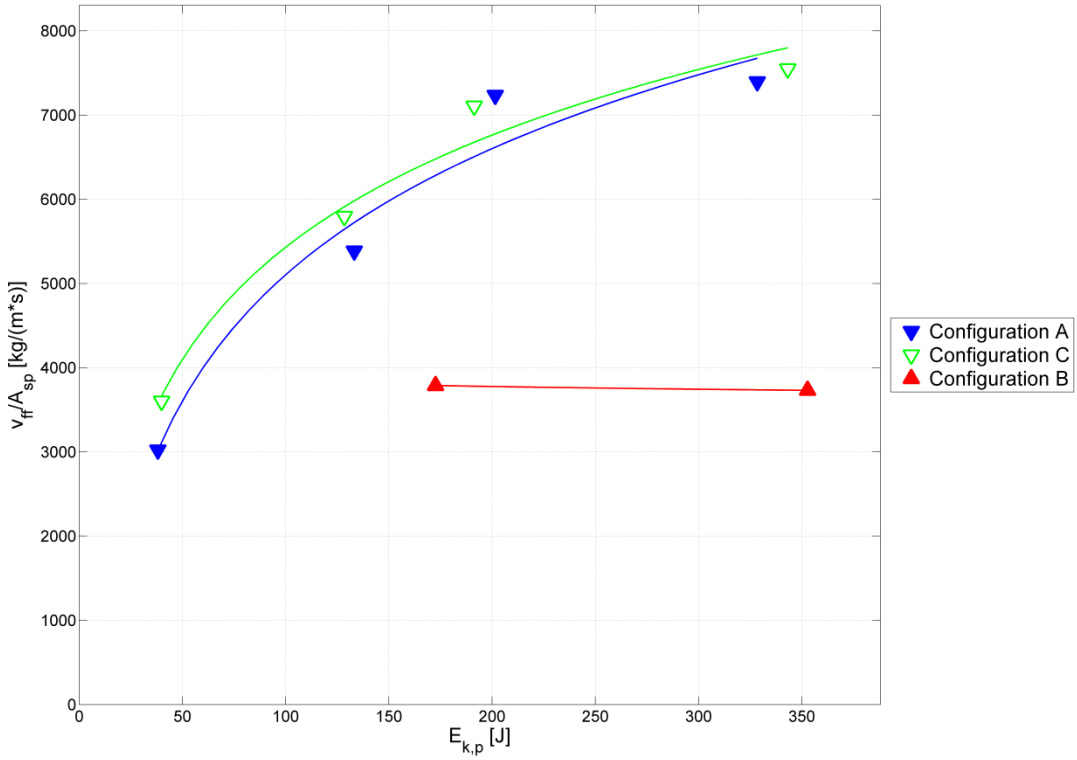

Figure 4.24 Fastest fragment velocity in the debris cloud divided by the target specific area as a function of projectile kinetic energy for layers A, B and C.

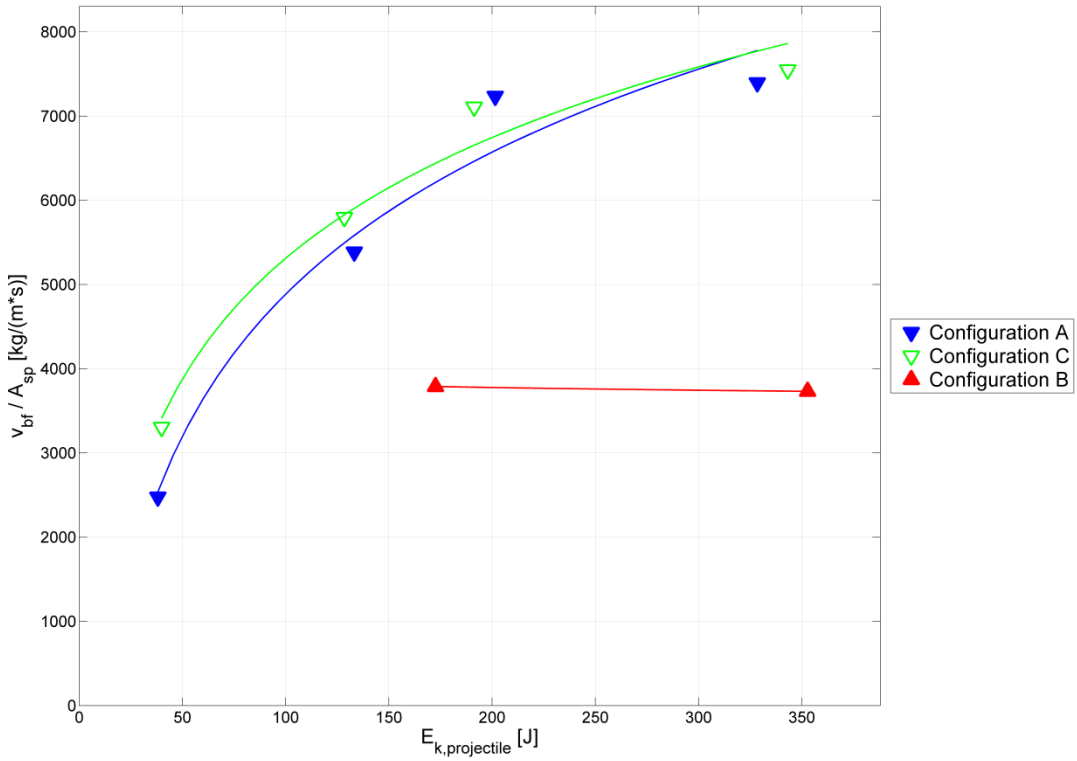

Figure 4.25 Biggest fragment velocity in the debris cloud divided by the target specific area as a function of projectile kinetic energy for layers A, B and C.

Images of the witness plates for the panels A, C and B for shots 8980, 8981 and 8992 are given in Figure 4.26. While the ionomer capability to fragment the projectile was already observed to be weak in section 4.4.1. and is confirmed again in Figure 4.26, the composite materials (panels A and C) show similar behaviour to the ionomer regarding projectile fragmentation. By looking at the witness plates it can be observed that almost no fragmentation of the projectile (or very little) occurred for impacts on panels A and C, as well as for impacts on the ionomer. While damage on the witness plate for panels A and C is more widely distributed than for panel B, it has to be noticed that it is composed of one big crater in the centre and small craters distributed around the central one. The central crater belongs to the remain of the projectile, while the smaller craters distributed all over the witness plate are caused by the material coming from the target and not by projectile fragmentation. Few smaller craters caused by projectile fragments can be found close to the big one, but they are anyway much smaller than the biggest crater. This points out that very little fragmentation of the projectile occurred also during impact on the composite panels. This is also confirmed by the high-speed video camera images shown in Figure 4.27, where a big fragment is clearly visible for all three panels.

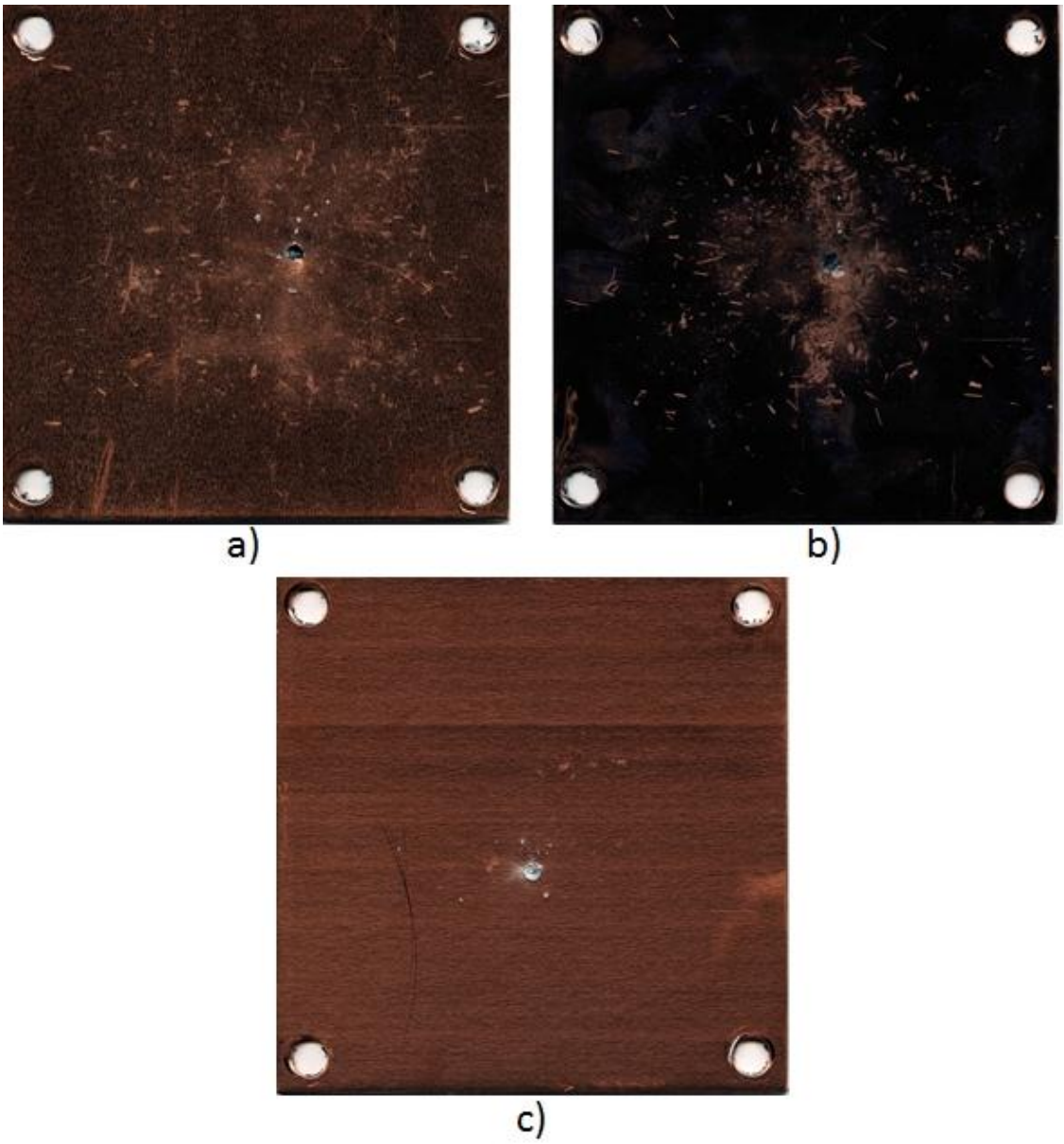

Figure 4.26 Witness plates of the following shots/panels: a) 8980/panel C, b) 8981/panel A, and c) 8992/panel B.

From the data presented above, very similar behaviour of panels A and C is found for the tests presented in Table 4-3, leading to the conclusion that the addition of aramid fibre composite fabric on the faces of the CFRP panel does not improve significantly the sample performance in terms of momentum transfer, debris cloud fragments velocity and even projectile fragmentation, under the impacts performed in this study. For the panel B it results that the momentum transfer and the velocity of the fragments in the debris cloud is less than for panels A and C. This evidences once more the CFRP weak resistance to out of plane impact loading.

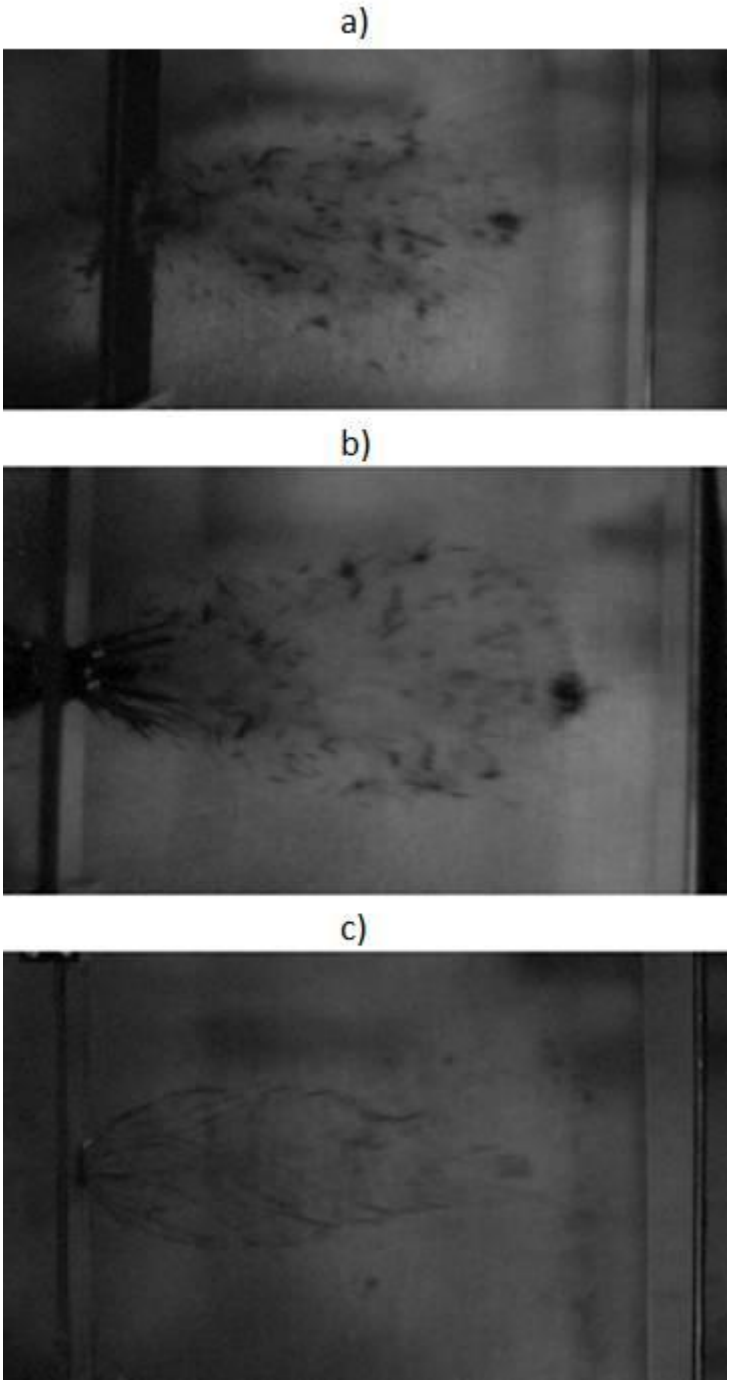

Figure 4.27 High-speed video camera images for shots on a) panel C (shot 8980), b) panel A (shot 8981) and c) panel B (shot 9046).

4.4.3.2. Two layers configurations of the multifunctional panel

In this part the experimental results for the configurations consisting of one structural layer and one self-healing layer are presented. The tested configurations are AB, BA, CB, and BC. In Table 4-4 the impact conditions and measured values are reported.

An unexpectedly low value of the transferred momentum is measured for the shot 9041. It is believed that the measure is not accurate, since high ratio of signal to noise was present in the signal

and some problems with the laser functioning occurred as well. Therefore the registered momentum of the ballistic pendulum is not taken into consideration for shot 9041.

Table 4-4 Initial impact conditions and measures of momentum transfer, biggest and fastest fragment velocities for panels AB, BA, CB and BC.

Shot number	Target	Parts	Projectile diameter - d_p (mm)	Projectile velocity - v_p (m/s)	Target areal density (kg/m^2)	Fastest fragment velocity (m/s)	Biggest fragment velocity (m/s)	Transferred momentum (kg*m/s)
8989	CFRP-05/I-01	AB	3.5	1878	7.49	447	395	0.02104
8994	I-03/CFRP-06	BA	3.5	2049	7.49	749	680	0.05113
8995	I-04/CFRP-07	BA	2.3	2085	7.49	0	0	0
8996	CFRP-08/I-05-01	AB	2.3	2170	7.49	0	0	0
8997	KCK-05/I-05-02	CB	3.5	2096	6.85	714	714	0.0437
8999	KCK-06/I-06	CB	2.3	2102	6.85	0	0	0
9000	I-08-01/KCK-07	BC	3.5	2055	6.85	753	594	0.05462
9001	I-08-02/KCK-08	BC	2.3	2096	6.85	0	0	0
9004	CFRP-09/I-09	AB	3.5	2543	7.49	760	760	0.04157
9005	I-10-01/CFRP-10	BA	3.5	2615	7.49	940	850	0.08810
9006	I-10-02/KCK-10	BC	3.5	2615	6.85	1085	907	0.09574
9007	KCK-11/I-11	CB	3.5	2615	6.85	905	905	0.06227
9040	CFRP-24/I-24	AB	4.5	2533	7.49	1102	1073	0.09422
9041	I-25/KCK-21	BC	4.5	2518	6.85	1294	1265	0.12305
9042	I-27/CFRP-26	BA	4.5	2495	7.49	1140	1140	0.2403
9043	KCK-20/I-26	CB	4.5	2304	6.85	1169	1169	0.18257

.

In Figure 4.28 the momentum transferred to the witness plate behind the target ($Q_{pendulum}$) is divided by A_{sp} and is plotted with respect to the projectile momentum. Interpolation curves are plotted to highlight the data trend and the differences between the data. Since the momentum transfer for projectile momentum of ~0.3 kg*m/s is missing for panel BC, data regarding this panel is not interpolated, instead just the data points are shown. If comparing configuration AB versus BA, and CB versus BC we see that when the ionomer is on the back of the assembly a smaller value of $Q_{pendulum}/A_{sp}$ is obtained than in a configuration with the ionomer as the front layer. This difference is more pronounced for the AB and BA configurations. Also the slope of the trends is smaller when the ionomer is on the back which suggests that the observed difference is increasing with projectile momentum increase. This underlines that the contribution of the ionomer to the two-layers panel behaviour depends on the ionomer position in the assembly. Furthermore, among all panels AB provides least momentum transfer. Except for panel AB, the slope of the curves is slightly

increasing. Above the value of approximately 0.1 kg*m/s, the data points appear to lay on a straight line, indicating a linear behaviour for higher impacting momentum.

In Figure 4.28 panels BA and BC behave similarly, while this is not true for panels AB and CB.

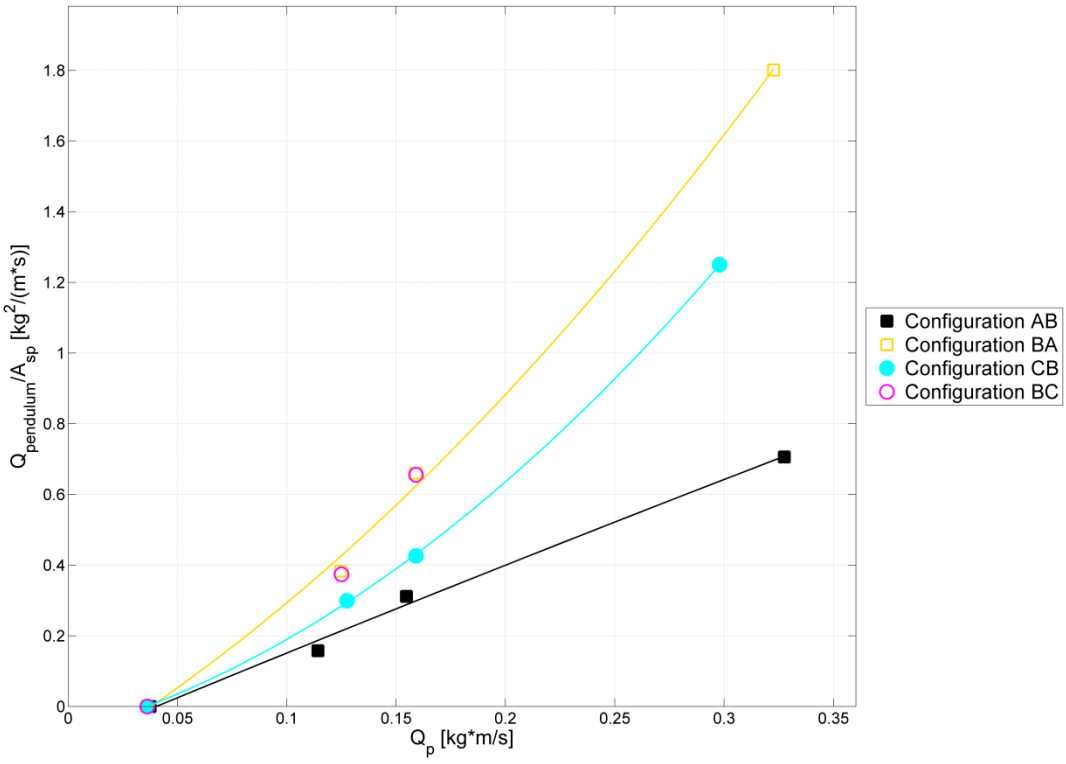

Figure 4.28 Momentum transfer to the ballistic pendulum divided by the target specific area for panels AB, BA, CB and BC.

Both the fastest fragment and the biggest fragment velocity divided by A_{sp}, shown respectively in Figure 4.29 and Figure 4.30, is very similar for all the configurations. For the range of projectile kinetic energy shown in Figure 4.29, the fastest fragment velocity if the ionomer is put on the front or on the back side varies no more than ~10% for the AB and BA comparison, or even less if considering CB and BC. Anyway, the velocity is smaller when the ionomer is on the back. The same observations are valid for the biggest fragment velocity, shown in Figure 4.30, where again a minor difference with respect to the ionomer position and between the configurations is present.

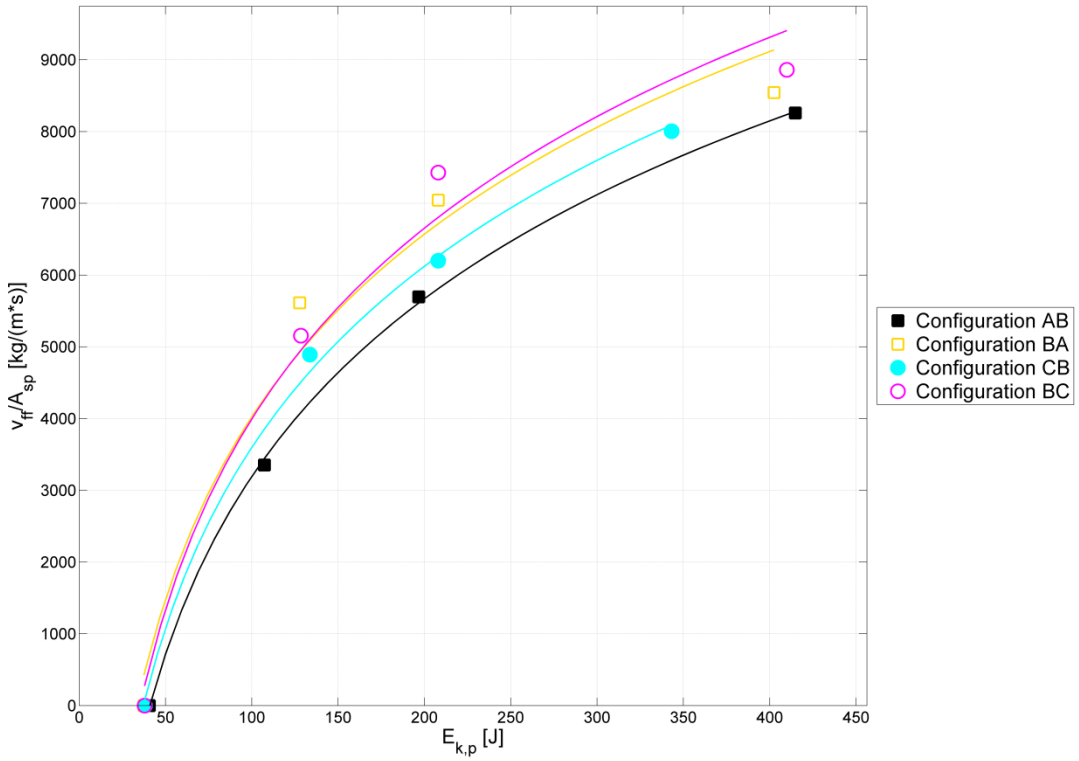

Figure 4.29 Fastest fragment velocity divided by A_{sp} for configurations AB, BA, CB and BC.

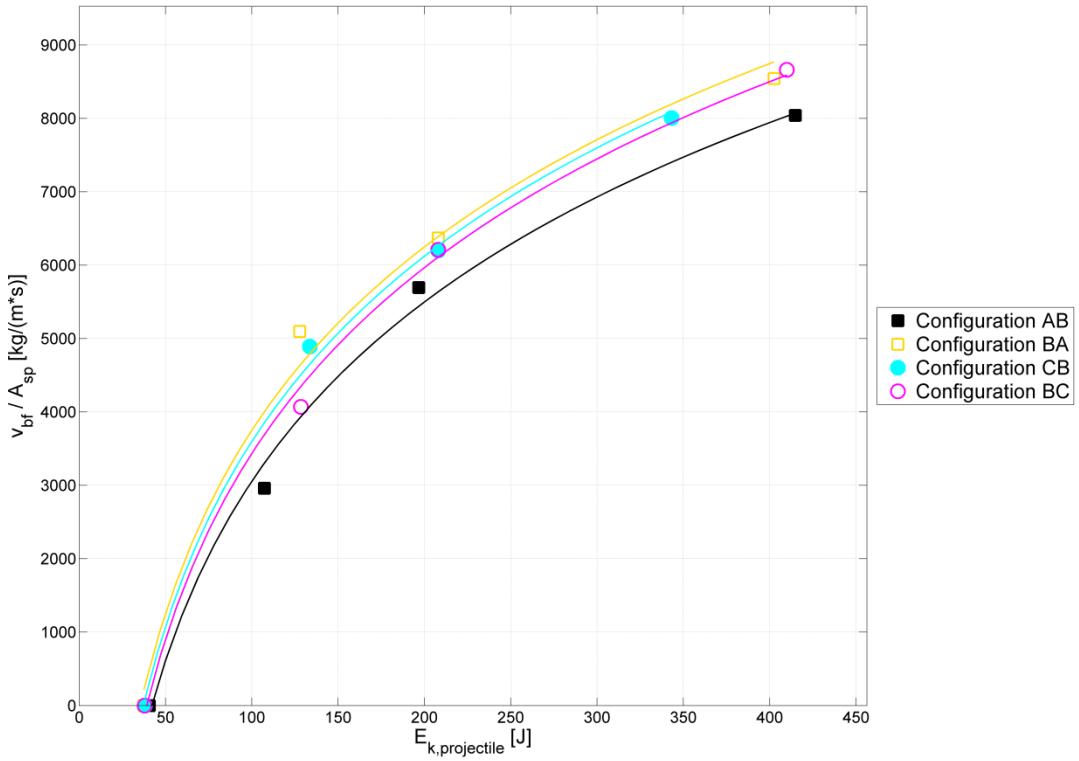

Figure 4.30 Biggest fragment velocity divided by A_{sp} for configurations AB, BA, CB and BC.

4.4.3.3. Comparison between single, double and triple layer configurations

Few tests were carried out for three-layers configurations. The tested three layer configurations consist of two structural layers and one self-healing layer. Details about the targets and projectiles, as well as the results of the tests are reported in Table 4-5.

Table 4-5 Initial impact conditions and measures of momentum transfer, biggest and fastest fragment velocities for three-layers configurations. d_p is the projectile diameter, and v_p is the projectile velocity. Glued panels are indicated with *.

Shot number	Target	Parts	d_p (mm)	v_p (m/s)	Target areal density (kg/m^2)	Fastest fragment velocity (m/s)	Biggest fragment velocity (m/s)	Transferred momentum (kg*m/s)
9008	CFRP-12/I-12/CFRP-11	ABA	3.5	2229	13.09	0	0	0
9009	CFRP-13/I-14/CFRP-14	ABA	3.5	2534	13.09	0	0	0
9010	KCK-12/I-15/CFRP-15	CBA	3.5	2569	12.44	0	0	0
9011	KCK-13/I-16/CFRP-16	CBA	3.5	1984	12.44	0	0	0
9016	KCK-16/I-19/CFRP-19	CBA	4.5	2467	12.44	519	169	0.04389
9017	CFRP-20/I-20/CFRP-21	ABA	4.5	2508	13.09	541	167	0.03969
9018	CFRP-22/I-21/KCK-17	ABC	4.5	2327	12.44	510	266	0.02694
9019	KCK-18/I-22/KCK-19	CBC	4.5	2403	11.79	551	352	0.09905
9021	KCK-I-C-01	CBA*	4.5	2446	12.44	457	252	0.03784
9032	KCK-I-C-02	ABC*	4.5	2442	12.44	423	188	0.02771
9034	KCK-I-01	CB*	3.5	2022	6,85	772	717	0.04265

It can be seen from the table that in all the samples the ionomer layer was placed in the middle, i.e. between the structural layers which were placed on the front and back sides. A test on one double layer panel is reported. The dissimilarity of this panel with the previously presented panels is only that in this panel the layers were glued together. Also in two three-layers panels the parts were glued together, as indicated in Table 4-5.

Here, the one-layer, two-layers and three-layers configurations are compared. The values of $Q_{pendulum}/A_{sp}$, v_{bf}/A_{sp}, and v_{ff}/A_{sp} for all configurations are plotted in Figure 4.31, Figure 4.32 and Figure 4.33, respectively.

In Figure 4.31 configurations BC and BA have a bigger slope than the single layers A and C. Furthermore, up to the projectile momentum of ~0.15 kg·m/s the layers A and C transfer more momentum, while over that value panels BA and BC are the ones transferring more momentum. The increase in momentum transfer with increasing projectile momentum seems to be faster also for the sample CB than for panels A and C. Nevertheless, up to the value of approximately 0.3 kg·m/s

less momentum is transferred for the configuration BC, and at this point the pendulum momentum is almost the same for A, C and BC. The trend suggests that above this value single layers should transfer less momentum. For configuration AB the pendulum momentum is less than for the samples A and C over the entire data range, and from the interpolation it seems that the difference is slowly increasing.

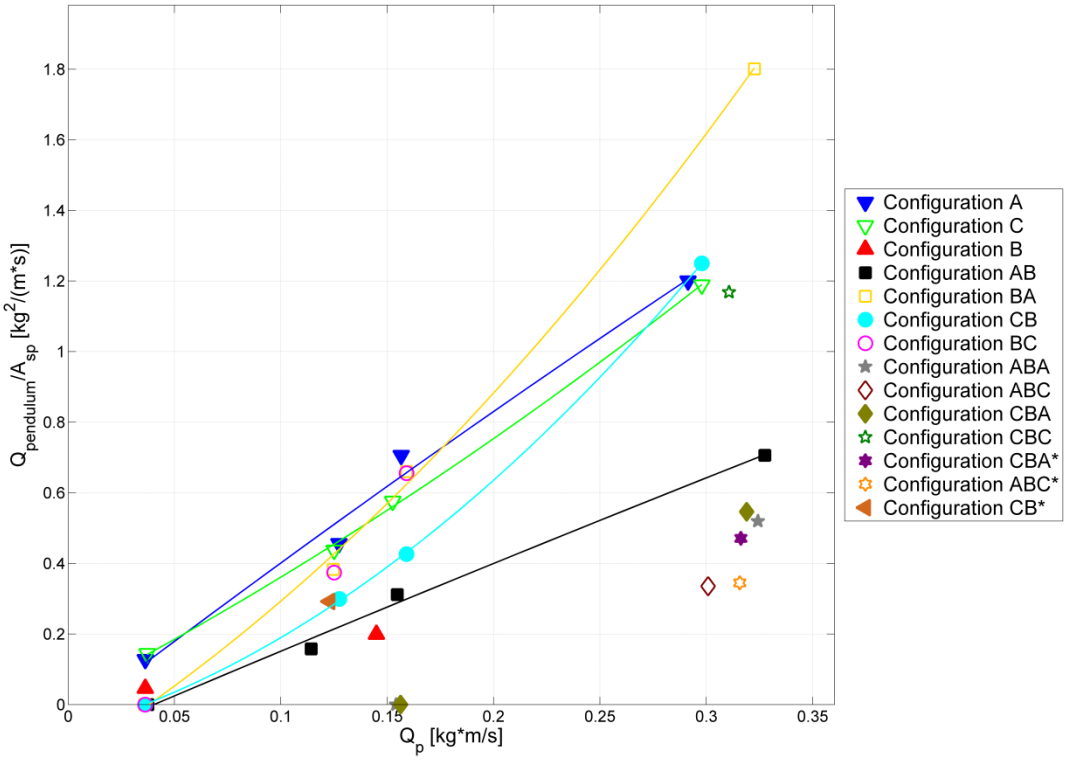

Figure 4.31 Momentum transferred to the pendulum divided by the target areal density, for all the configurations tested.

For all three-layers configurations, except for the configuration CBC, the momentum transferred to the witness plate is less than for the one-layer and two-layers configurations, at least for the impact conditions considered in this study.

Configurations CB* and ABC* are assembled by gluing the layers together. The momentum transfer is somewhat higher for ABC with respect to its glued counterpart ABC*, while CB* and CB are almost equal.

Both in Figure 4.32 and Figure 4.33 the respective velocities of the fastest and biggest fragments are little slower for configurations AB, BA, CB and BC with respect to A and C at lower impact energies, but at higher projectile kinetic energies they become very similar. From the available data it is difficult to predict the behaviour for energies above 400 J, but the trend seems to indicate perhaps slower velocities for the layers A and C.

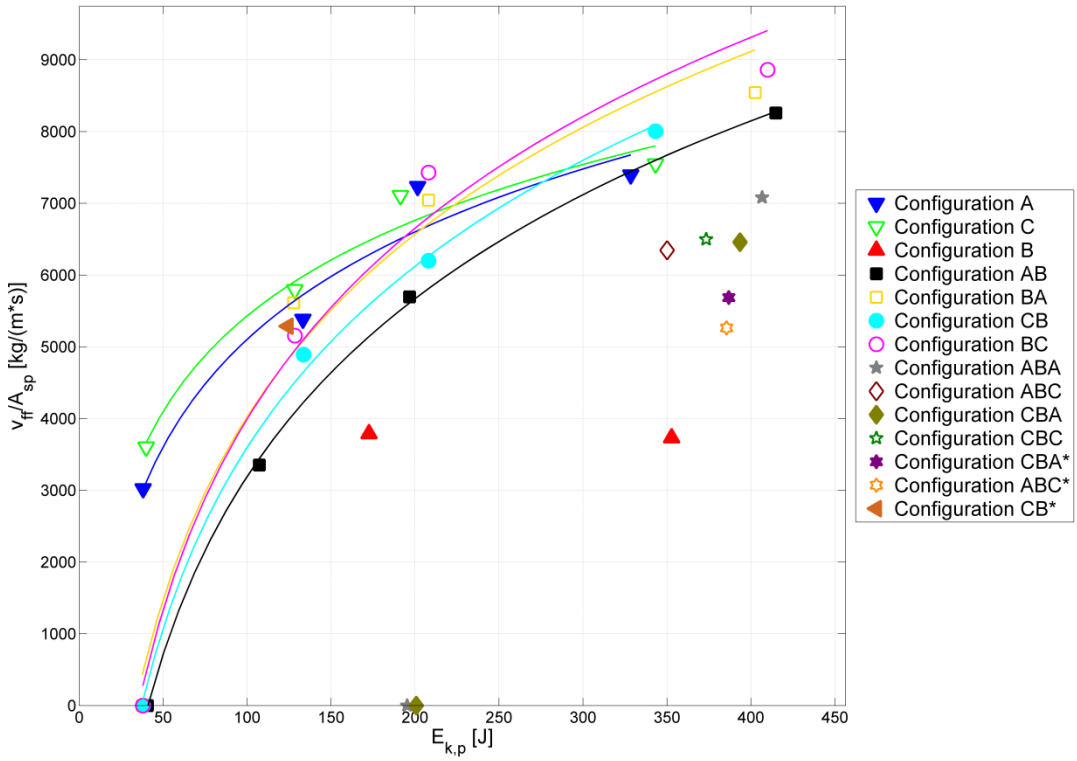

Figure 4.32 Fastest fragment velocity divided by *Asp* for all the configurations.

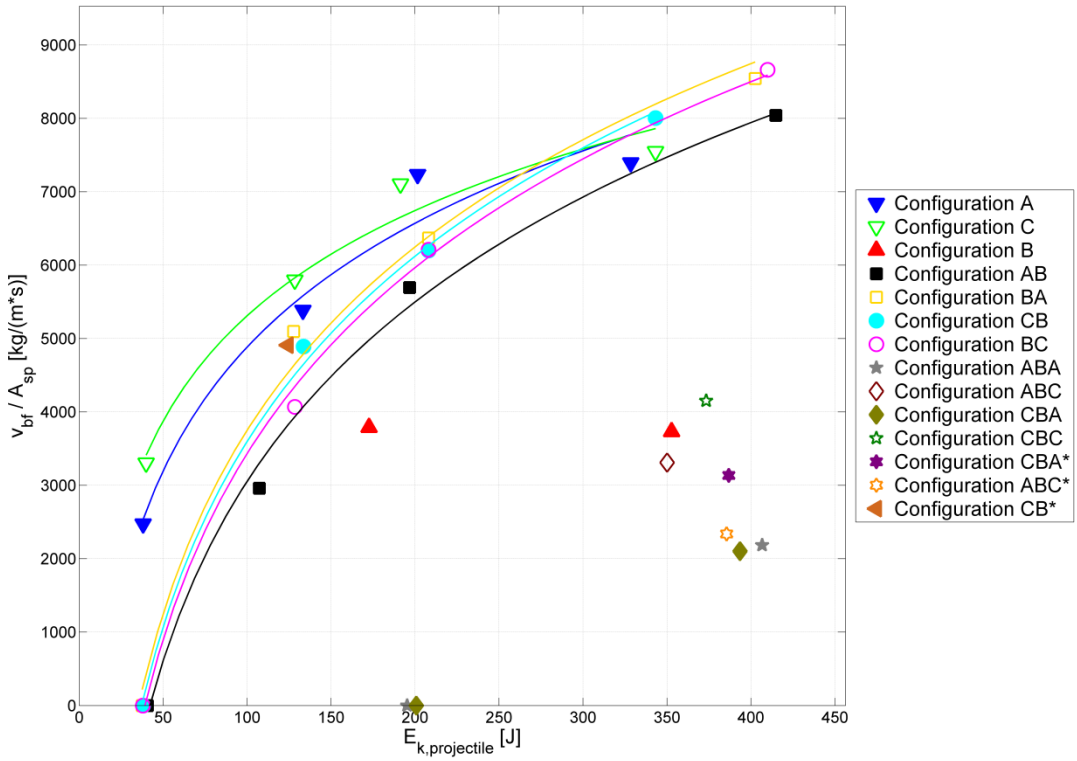

Figure 4.33 Biggest fragment velocity divided by *Asp*, for all configurations.

The velocities of the fragments for the three-layers configurations are slower than those for the other assemblies, except for the ionomer alone (panel B). The difference is more notable for the biggest fragment velocity. Similarly as in Figure 4.31, no particular difference in the glued configurations behaviour with respect to the corresponding not glued configurations is observable.

The ionomer, compared to the other configurations, shows relatively low momentum transfer and debris cloud velocities, as it can be seen in the above figures. Even if the ionomer exhibited a good performance compared to the composite panels, its main disadvantage are its mechanical properties for structural applications, which are not to the level of commonly applied materials, hence the ionomer is coupled to the composite material to obtain a multifunctional structure.

It can be concluded that the three-layer sandwich configuration among the multifunctional panel structures appear to be the optimal one in terms of fragment velocities in the debris cloud and momentum transfer of the debris cloud to the pendulum, while at the same time incorporating the structural and self-healing layers.

4.4.4. Damage of the panels

In this section the damage measures taken on the panels are defined and some comparisons based on the damage evaluation are performed.

In Figure 4.34 a sample of panel A after impact is shown. The measures taken to evaluate the damage are indicated, together with their respective labels.

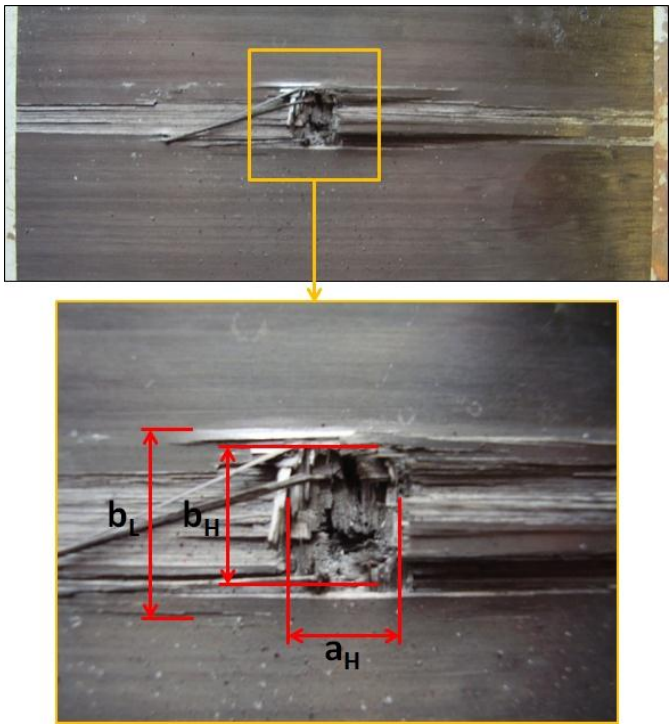

Figure 4.34 Visible damage on impact face for panel A and definition of damage measures.

Panel A exhibited most damage on the top and bottom surfaces, where stripes of fibres detach from the surface layer. Their width is similar to the hole diameter, but they extend far from the hole in the fibre direction. For almost all impacted samples this detachment was observed to extend over the entire panel width. If a layer of ionomer was placed on the surface of panel A, this prevented such a wide extension of fibre detachment. Similar damage pattern is observed on both the front and back side of the panel. Due to the structure of the CFRP it was difficult to determine the hole diameter. Anyway, labels a_h and b_h in the figure indicate the region of total material failure, in which the failed material is just holding to the less damaged surrounding material, and this region is referred to as the 'external hole'. This hole size is taken as the average of a_h and b_h and is denoted as d_h. The visible extension of cracks in the vertical direction is denoted as b_L. Measures of the quantities indicated in Figure 4.34 are taken on both the front and back of the target.

The quantities measure from panels C to quantify its damage are shown in Figure 4.35.

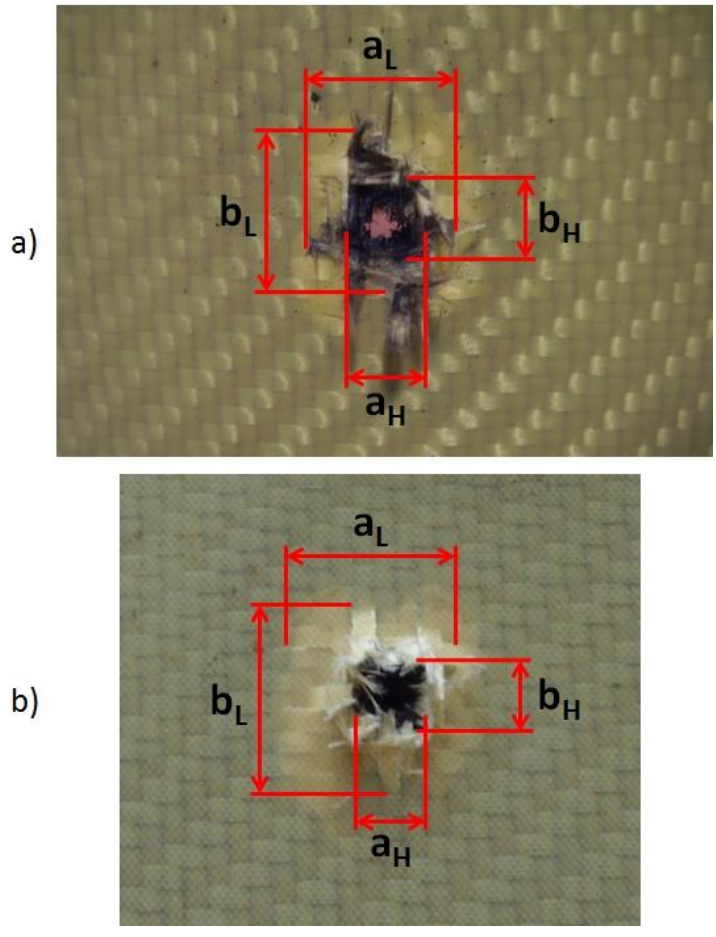

Figure 4.35 Visible damage on impact (a) and rear (b) for panel C and definition of damage measures.

The extension of cracks visible on the surface was measured for the vertical (b_L) and horizontal (a_L) directions. For panels C it was very difficult to distinguish anything around the impact point, since the panel is very damaged in that area and a lot of fibres are present even if completely damaged, as

seen in Figure 4.35. This region is denoted with a_h for its horizontal direction extension and with b_h for its vertical direction extension, and the average of the two is denoted as d_h, as it was done for panel A.

Few samples of panel A and panel C were inspected with the ultrasound flaw detector in order to check if delamination had occurred in the panels and to measure its extent. In Figure 4.36 an image of the delaminated area of a composite panel detected with the ultrasound system is shown. The extent of delamination is labelled as b_d. Those measurements were used to compare the numerical simulations with the experiments, and thus are given in the next chapter.

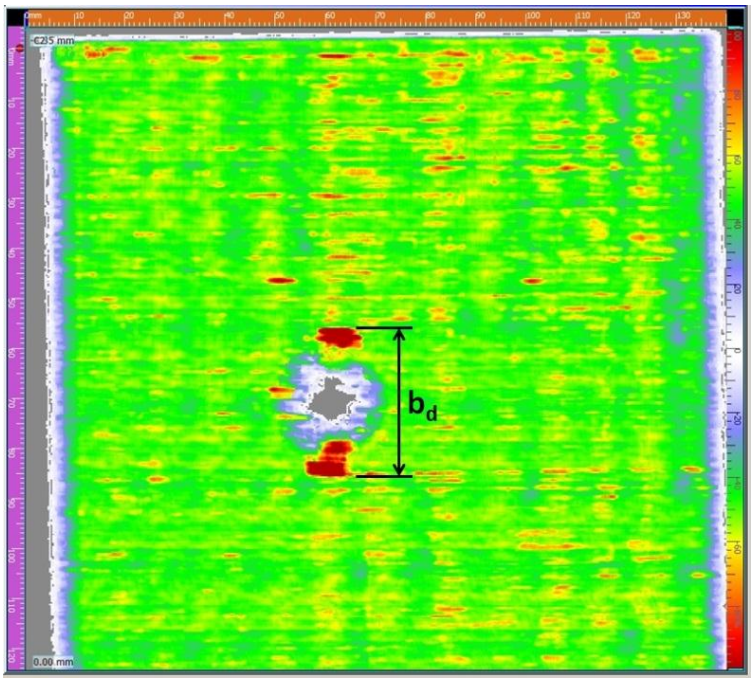

Figure 4.36 Ultrasound system damage detection (panel C example) and definition of the measure taken.

The damage on panel B is highly localized in the impact area and it was observed that the damaged area is circular and its diameter is almost equal to the projectile diameter (see for example Figure 4.12, Figure 4.13, and Figure 4.21). The diameter of the area that has undergone severe changes due to deformation or phase change (which is also referred to as the damaged area) was measured from the samples and is denoted with d_h (this is the same as the 'external hole diameter' in section 4.4.2).

In the following figures some considerations about damage are given. The measured damage values plotted in the figures are normalized with respect to the projectile diameter (d_p) and the target areal density (ρ_A).

Figure 4.37 shows the normalized value for d_h on the back of panels A. It can be seen that there is a similar distribution of the damage values between the configurations at various impact energies. The small value for shot 8995 is due to the fact that the panel was not perforated, but only some

damage caused from spallation was found. The least damage for $d_{h,back}$ is found for configuration AB, which is due to the ionomer that is slightly hindering the damage of CFRP on their interface. Panel A gets mostly damaged on the back in configuration BA, while the damage on A used alone is between the two-layer configurations.

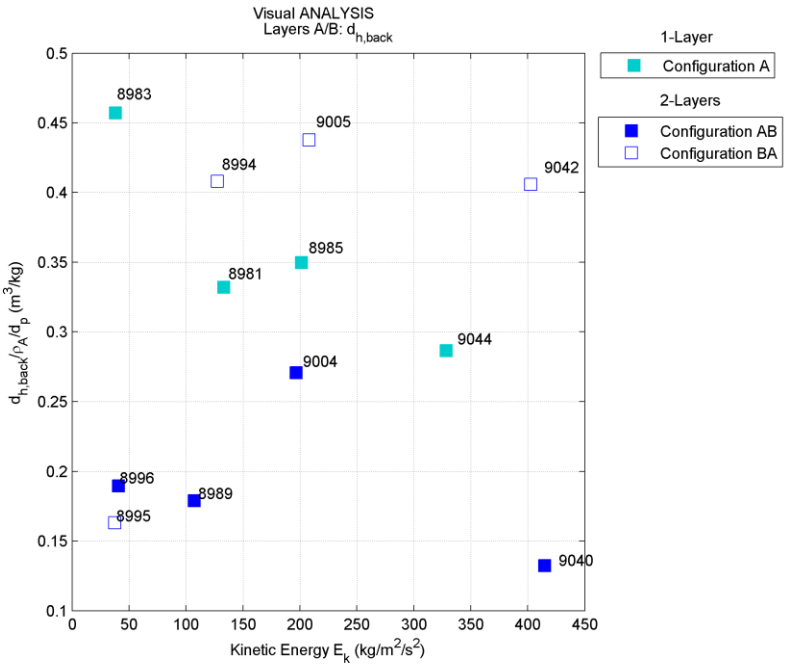

Figure 4.37 Comparison of $d_{h,front}/(d_p\rho_A)$ for panel A for one-layer and two-layer configurations.

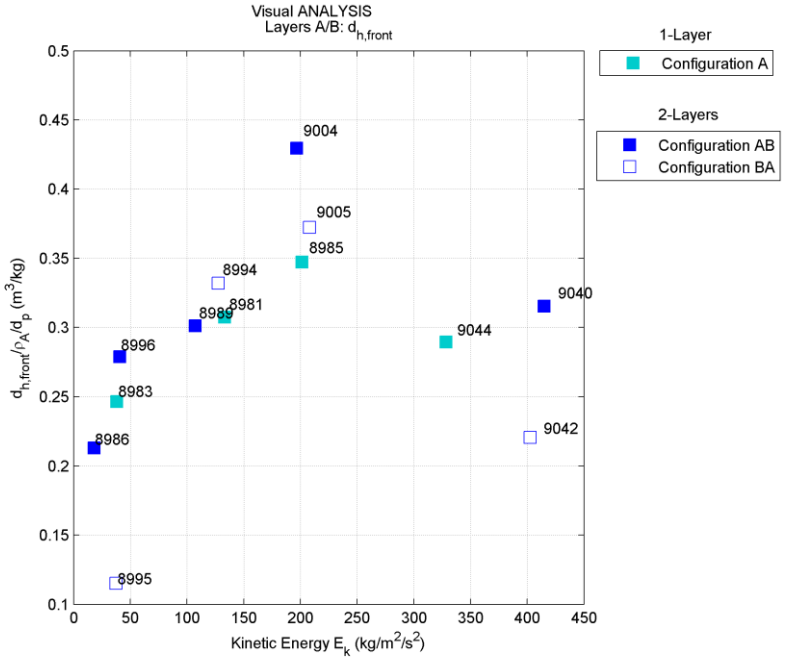

Figure 4.38 Comparison of $d_{h,back}/(d_p\rho_A)$ for panel A for one-layer and two-layer configurations.

In Figure 4.38 the value of d_h on the front of the panel A is plotted for three configuration cases. Most of the damage seems relatively similar between configurations, but no straightforward conclusions can be made.

The comparison for the value of $d_{h,front}$ divided with d_p and ρ_A for the panels A, B and C is given in Figure 4.39. For all shots least damage is observed for panel A, then comes panel C and lastly panel B. All panels exhibit a similar trend for increasing impact velocity.

Figure 4.40 shows crack extension b_L in the vertical 'b' direction on the front of the panels A and C, in several configurations. This figure indicates that the superficial crack propagation is highly dependent on the fibre direction in the superficial layer. Since panel C has fibres in both direction (vertical and horizontal, i.e. 'a' and 'b') the crack propagates more than for panel A, that has no fibres oriented in the 'b' direction in the superficial layer. But the crack propagation in the vertical direction is soon arrested by fibres oriented normally to the crack propagation direction. This results in a more equilibrated damage in both direction for panels C (Figure 4.35) than for panels A, in which we see from Figure 4.34 that the crack propagates from the hole up to the panel border side. The crack is prone to propagation in the fibre direction because this process in the fibre direction is happening mainly through matrix intralaminar and interlaminar failure. For a crack to propagate orthogonally to the fibres direction, fibres should fail, but they are much more resistant than the matrix.

Observations similar to those made for Figure 4.40 are possible also for Figure 4.41, i.e. for the crack extension on the back of the target.

The observations made in Figure 4.40 and Figure 4.41 only highlight the fibre orientation influence on the superficial damage and crack propagation. It does not mean that the CFRP exhibits better performance. Instead, for that matter the entire damaged area should be regarded, for which it is quite obvious from Figure 4.34 and Figure 4.35 that it is larger for the CFRP panels (similar behaviour was observed in all the other tests).

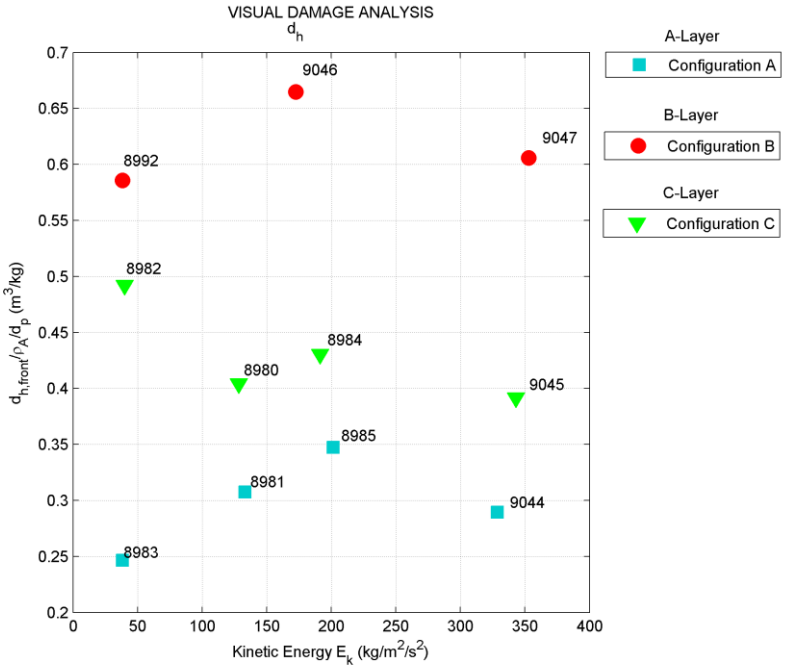

Figure 4.39 Comparison of $d_{h,front}/(d_p\rho_A)$ between panels A, B and C.

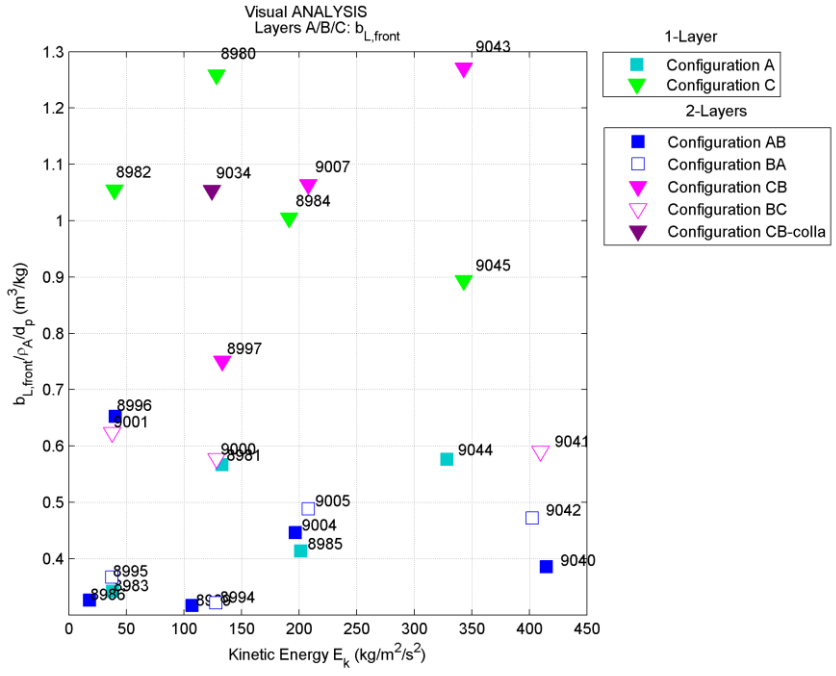

Figure 4.40 Values of $d_{b,front}/(d_p\rho_A)$ for panels A and C in one-layer and two-layer configurations.

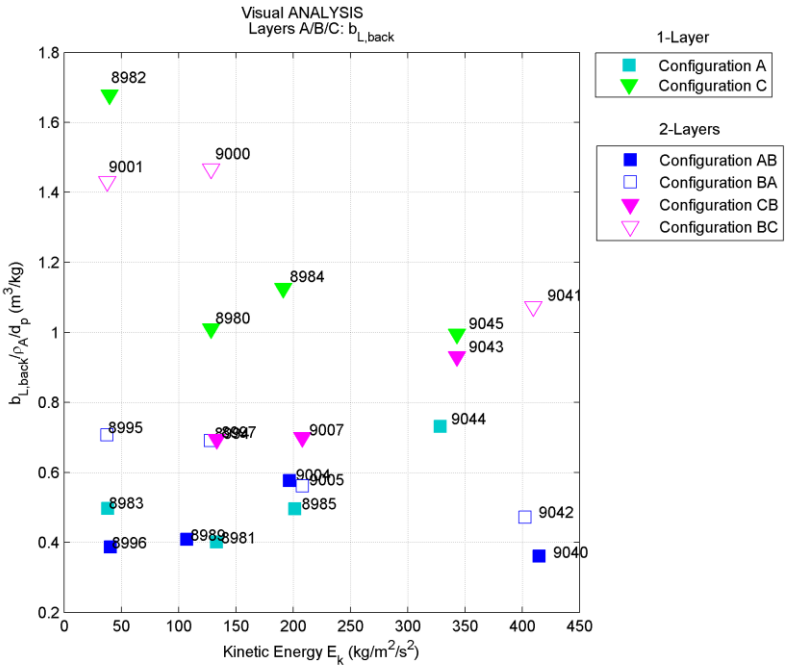

Figure 4.41 Values of $d_{b,back}/(d_p\rho_A)$ for panels A and C in one-layer and two-layer configurations.

4.4.5. Self-healing results

Herein the results of the ionomer self-healing in the performed impact tests are reported. For each test, the ionomer layer was checked visually to see if a hole was present. The results are reported in Table 4-6. The configurations in which it was not possible to assess the self-healing visually are omitted from the table. Initially a more rigorous self-healing assessment, based the application of a pressure gradient between the sample top and bottom faces, was planned but time restrictions made it impossible.

Table 4-6 Impact conditions and self-healing results.

Shot number	Target	Parts	Projectile diameter - d_p (mm)	Projectile velocity - v_p (m/s)	Target areal density (kg/m^2)	Perforation (Yes/No)	Hole sealing (Yes/No)
8989	CFRP-05/I-01	AB	3.5	1878	7.49	Yes	Yes
8992	I-02	B	2.3	2102	1.90	Yes	No
8994	I-03/CFRP-06	BA	3.5	2049	7.49	Yes	Yes
8995	I-04/CFRP-07	BA	2.3	2085	7.49	No	Yes
8996	CFRP-08/I-05-01	AB	2.3	2170	7.49	No	-
8997	KCK-05/I-05-02	CB	3.5	2096	6.85	Yes	No
8999	KCK-06/I-06	CB	2.3	2102	6.85	No	-
9000	I-08-01/KCK-07	BC	3.5	2055	6.85	Yes	No
9001	I-08-02/KCK-08	BC	2.3	2096	6.85	No	Yes
9004	CFRP-09/I-09	AB	3.5	2543	7.49	Yes	Yes
9005	I-10-01/CFRP-10	BA	3.5	2615	7.49	Yes	Yes
9006	I-10-02/KCK-10	BC	3.5	2615	6.85	Yes	Yes
9007	KCK-11/I-11	CB	3.5	2615	6.85	Yes	No
9009	CFRP-13/I-14/CFRP-14	ABA	3.5	2534	13.09	No	Yes
9010	KCK-12/I-15/CFRP-15	CBA	3.5	2569	12.44	No	Yes
9011	KCK-13/I-16/CFRP-16	CBA	3.5	1984	12.44	No	Yes
9016	KCK-16/I-19/CFRP-19	CBA	4.5	2467	12.44	Yes	No
9017	CFRP-20/I-20/CFRP-21	ABA	4.5	2508	13.09	Yes	No
9018	CFRP-22/I-21/KCK-17	ABC	4.5	2327	12.44	Yes	No
9019	KCK-18/I-22/KCK-19	CBC	4.5	2403	11.79	Yes	No
9034	KCK-I-01	CB*	3.5	2022	6.85	Yes	Yes
9040	CFRP-24/I-24	AB	4.5	2533	7.49	Yes	No
9041	I-25/KCK-21	BC	4.5	2518	6.85	Yes	No
9042	I-27/CFRP-26	BA	4.5	2495	7.49	Yes	No
9043	KCK-20/I-26	CB	4.5	2304	6.85	Yes	No
9044	CFRP-25	A	4.5	2254	5.59	Yes	No
9045	KCK-22	C	4.5	2304	4.95	Yes	No
9046	I-28	B	3.5	2382	1.90	Yes	No
9047	I-29	B	4.5	2336	1.90	Yes	No

In order to get a better overview, the results for the two-layers configurations are also summarized in Figure 4.42. In the figure 'x' refers to the case when the ionomer layer was not perforated, while empty markers indicate no sealing of the hole and full markers indicate a sealed hole. For the configurations AB and BA self-repair of the hole was successful for projectiles with diameter of 2.3 mm and 3.5 mm, and both for ~2.0 km/s and ~2.5 km/s impact velocities. When a projectile of 4.5 mm was used, no self-healing occurred. Since sealing of the hole depends on the ratio of projectile diameter to ionomer target thickness, this ratio was probably too high in shots 9040 and 9042 for self-healing of the hole to occur.

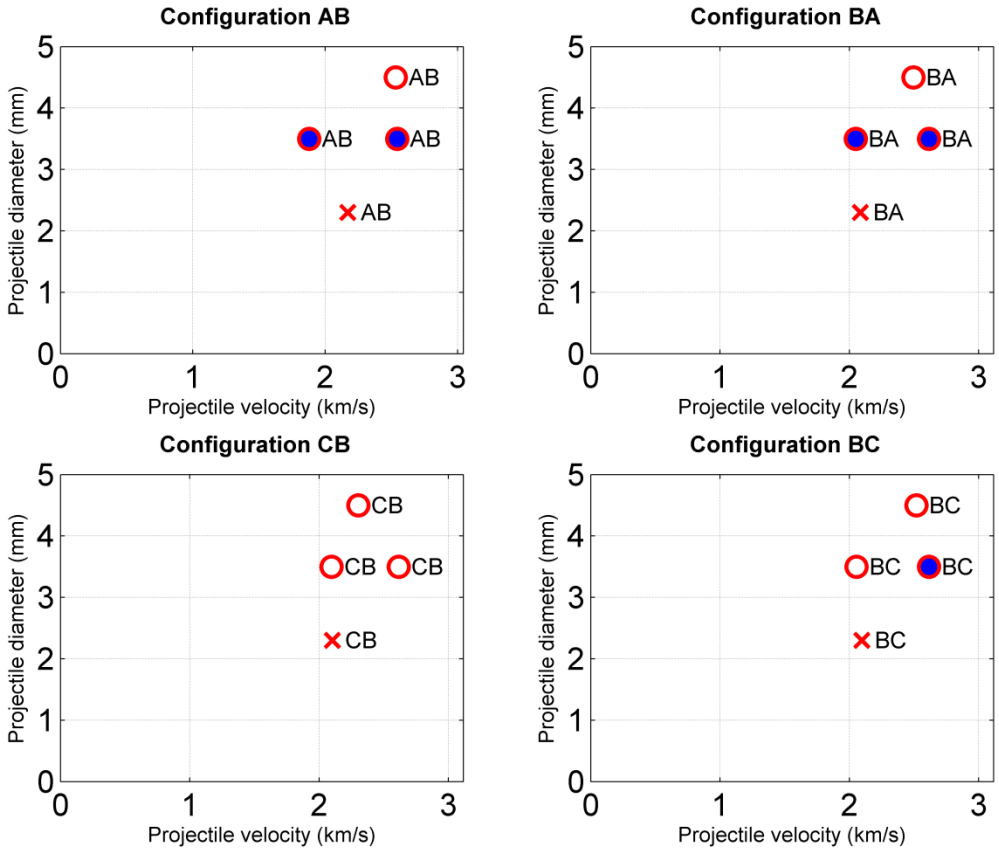

Figure 4.42 Two-layers configurations self-healing results overview. Empty markers refer to unsuccessful self-healing, full marker refer to successful self-healing, and 'x' indicates no perforation of the ionomer layer.

A worse performance of the ionomer was found when it was used with panel C. For the panel CB, a hole was present through the ionomer layer for all tests, except for 8999. In panels C, when tested alone, fibres were often sticking out in the impact area, see Figure 4.43. Even if in configurations CB and BC fibres were not found to stick out through the ionomer hole, this response could have obstructed the self-healing process. The results for configurations AB and BA in Figure 4.42 and Table 4-6 indicate that the ionomer can be used in combination with a structural layer. At the same time, the different results obtained in the two-layers configurations between the cases when panel A and panel C were used as structural layer, indicate that not only the presence of the structural layer influences the self-healing capability, but so does also its behaviour under impact loading.

The three-layers configurations were impacted with either a projectile with diameter of 3.5 mm and 4.5 mm. In the case of 4.5 mm projectile diameter, the samples were completely perforated by the projectile and the hole was not sealed. For the smaller diameter (3.5 mm) the impacted samples were not perforated, instead the projectile perforated the ionomer and stopped at the last layer. In those cases the ionomer successfully sealed the hole. Such situations where the projectile didn't pass through the entire target should not be underestimated, since spallation caused by stress wave

reflections from the back face and cracks propagating in the material could cause an opening through the structure, and therefore the healing of the hole is indeed necessary. Anyway, further tests of the three-layers configurations with different projectile diameters, ionomer thickness and impact velocity are necessary, in order to test the self-healing in such configurations more thoroughly.

Figure 4.43 Aramid fibres sticking out normally from the panel C surface after impact.

In Table 4-6 several tests performed on the ionomer alone are presented. In all those tests the hole was not sealed, but only partial self-repair of the hole did occur. A photo of the ionomer sample after shot 9047 is given in Figure 4.44.

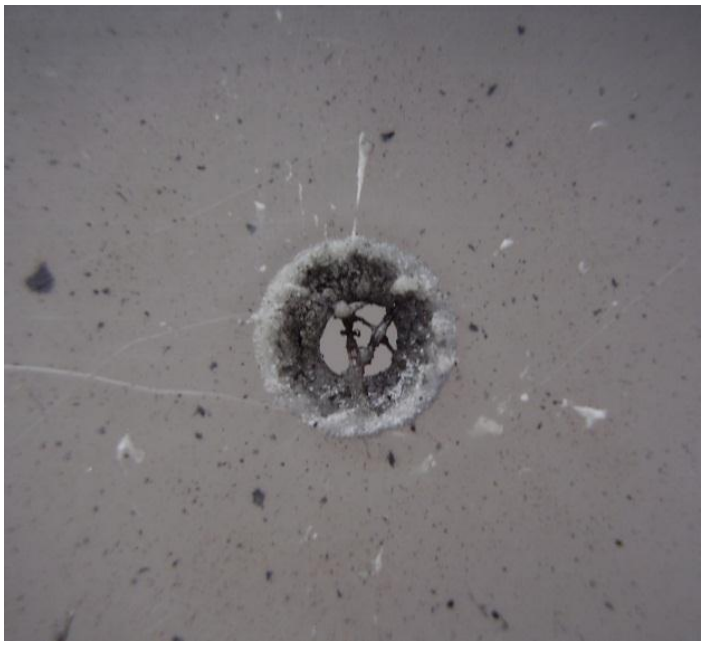

Figure 4.44 Photo of the impact area on the ionomer after shot 9047.

In shot 8992 the high speed camera was zoomed in the impact area on the back side of the target. Images of the impact at various time instants are shown in Figure 4.45. It can be seen that the material undergoes phase transition from solid to liquid. Material gets removed from the impact zone, which consequently causes a negative effect on the self-healing response, as the material itself is the healing agent. The material removal is more clearly visible for shot 9047, shown Figure 4.46. Therefore it is concluded that the material removal in hypervelocity impacts hinders the self-healing capability of the ionomer targets, leading to the need of applying much thicker samples with respect to the projectile diameter in order to achieve successful hole sealing.

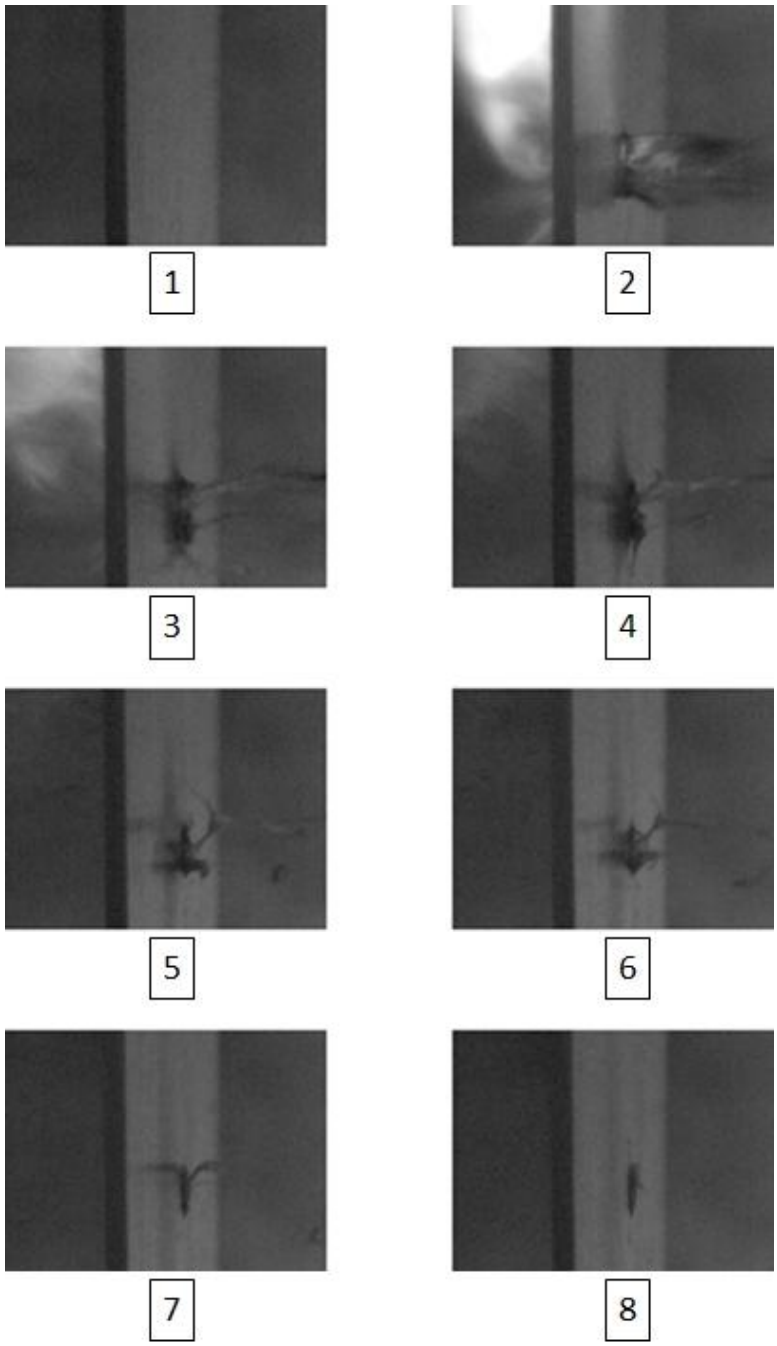

Figure 4.45 High-speed video camera time frames of shot 8992.

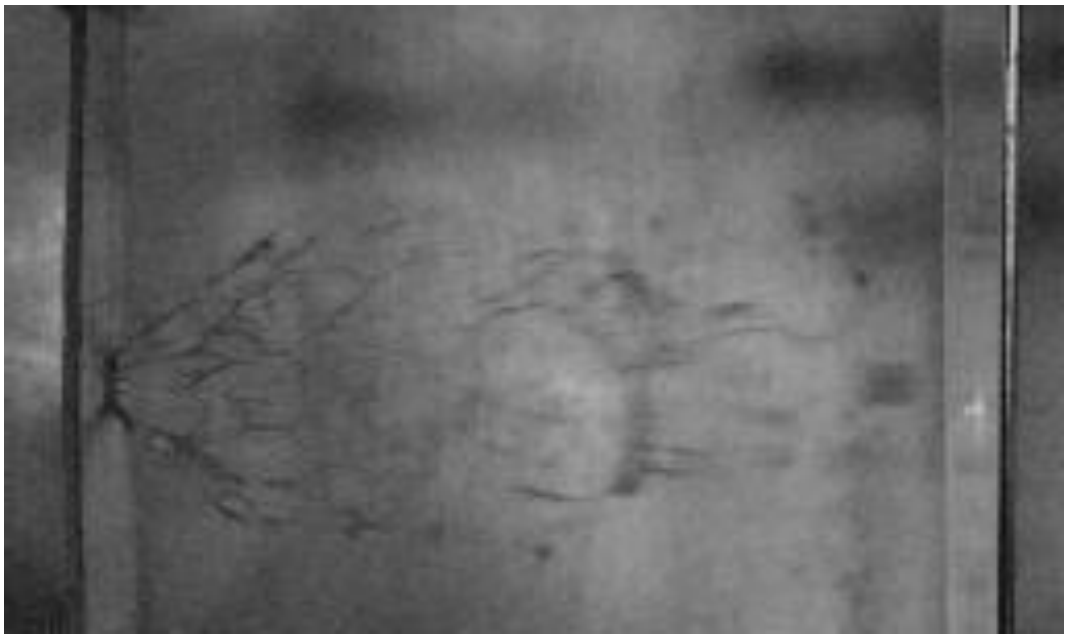

Figure 4.46 High-speed video camera image of shot 9047.

5. Numerical modelling

5.1. Introduction

Due to the high cost of experimental tests on one side, and improvement of numerical codes capabilities for non-linear dynamics simulations on the other side, there is a tendency to use simulations whenever possible. The main advantage of the numerical codes is the possibility to investigate a large number of impact conditions, like various velocities, geometries of the target and projectile, materials, and so on, which is often not possible or available in experimental tests. Therefore, numerical simulations are becoming an important and attractive approach for the solution of complex practical problems in science and engineering.

In this chapter numerical models for the single panels are presented and the simulations of the tests on single layer panels were performed. In order to validate the models, the numerical results were compared to the experiments. Damage on the targets and velocity of the projectile remnant after perforation were used for the comparison.

The numerical simulations were performed using ANSYS AUTDYN. The AUTODYN program is a general-purpose engineering software package for solving a wide variety of non-linear problems in solid, fluid and gas dynamics [55]. Such numerical codes are also known as ‘‘hydrocodes’’ [56]. The Smoothed Particle Hydrodynamics (SPH) method available in AUTODYN was used for the simulations. The SPH is a mesh free particle method used for solving problems of continuum solid and fluid mechanics [[57]-[61]]. The SPH method does not suffer from mesh tangling problems, since it is a meshless method, and it does not require unphysical erosion algorithm to obtain efficient solutions when extremely large deformations occur, such as in impact dynamics.

5.2. Governing equations

In high- and hyper-velocity problems shockwaves (see chapter 2) propagate through the colliding bodies, which often behave like fluids. Material strength becomes significant only at later stages. The governing equations for hydrodynamics with material strength are the conservation equations of continuum mechanics [62]:

$$\frac{D\rho}{Dt} = -\rho \frac{\partial v^{\beta}}{\partial x^{\beta}} \tag{5.1}$$

$$\frac{Dv^{\alpha}}{Dt} = \frac{1}{\rho}\frac{\partial \sigma^{\alpha\beta}}{\partial x^{\beta}} \tag{5.2}$$

$$\frac{De}{Dt} = \frac{\sigma^{\alpha\beta}}{\rho}\frac{\partial v^{\alpha}}{\partial x^{\beta}} \tag{5.3}$$

where ρ is the scalar density, e the internal energy, v^{α} the velocity component, $\sigma^{\alpha\beta}$ the total stress tensor, x^{α} the spatial coordinates and t the time. In equations (5.1)-(5.3) the Greek superscripts α and β denote the coordinate directions and summation is taken over repeated indices, while the total time derivatives are taken in the moving Lagrangian frame. Equations (5.1), (5.2) and (5.3) are the continuity equation, momentum equation and energy equation, respectively. These, together with a material model and a set of initial and boundary conditions, define the complete solution of the problem. The derivation of equations (5.1)-(5.3) can be found in [62].

5.3. Smoothed particle hydrodynamics

A brief description of the SPH method is given in the following, more details can be found in [[57]-[59],[62]]. The basis of the SPH method is an interpolation method which allows any function to be expressed in terms of its values at a set of disordered points, called the particles [59].
The integral interpolant of any function *f(x)* is defined by

$$f(x) = \int_{\Omega} f(x')W(x - x', h)dx' \tag{5.4}$$

where f is a function of the three-dimensional position vector x, W is the smoothing kernel function (or simply kernel), Ω is the volume of the integral that contains x, and h is the smoothing length defining the influence area of the smoothing function W.
The kernel function has the following two properties:

$$\int_{\Omega} W(x - x', h)dx' = 1 \tag{5.5}$$

$$\lim_{h \to 0} W(x - x', h) = \delta(x - x') \tag{5.6}$$

where $\delta(x\text{-}x')$ is the Dirac delta function:

$$\delta(x-x') = \begin{cases} 1 & x = x' \\ 0 & x \neq x' \end{cases} \tag{5.7}$$

The gradient of equation (5.4) can be obtained as

$$\nabla f(x) = \int_{\Omega} f(x') \nabla W(x-x', h) dx' \tag{5.8}$$

The continuous integral representations concerning the SPH kernel approximation (equations (5.4) and (5.8)) can be expressed in discretized forms of summation over all the particles in the support domain shown in Figure 5.1.

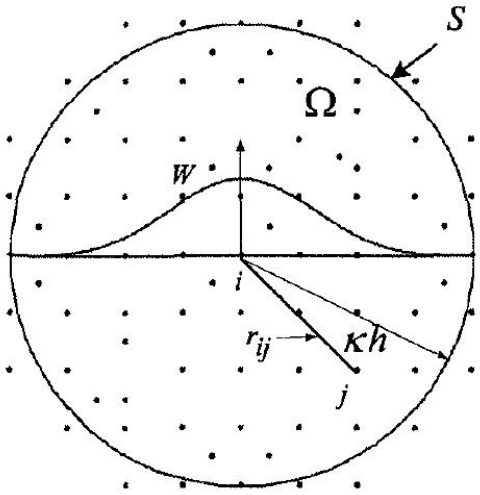

Figure 5.1 Particle approximations using particles within the support domain of the smoothing function *W* for particle *i*. The support domain is circular radius *κh* [62].

For a given particle *i*, the value of a function and its derivative for particle *i* are approximated as

$$f(x_i) = \sum_{j=1}^{N} \frac{m_j}{\rho_j} f\left(x_j\right) W_{ij} \tag{5.9}$$

$$\nabla f(x_i) = \sum_{j=1}^{N} \frac{m_j}{\rho_j} f\left(x_j\right) \nabla_i W_{ij} \tag{5.10}$$

$$W_{ij} = W\left(x_i - x_j, h\right) = W\left(\left|x_i - x_j\right|, h\right) \tag{5.11}$$

$$\nabla_i W_{ij} = \frac{x_i - x_j}{r_{ij}} \frac{\partial W_{ij}}{\partial r_{ij}} = \frac{x_{ij}}{r_{ij}} \frac{\partial W_{ij}}{\partial r_{ij}} \tag{5.12}$$

where r_{ij} is the distance between particle i and j.

The SPH formulation for hydrodynamics with material strength can be written as:

$$\frac{D\rho_i}{Dt} = \sum_{j=1}^{N} m_j \left(v_i^\beta - v_j^\beta\right) \frac{\partial W_{ij}}{\partial x_i^\beta} \tag{5.13}$$

$$\frac{Dv_i^\alpha}{Dt} = -\sum_{j=1}^{N} m_j \left(\frac{\sigma_i^{\alpha\beta}}{\rho_i^2} + \frac{\sigma_j^{\alpha\beta}}{\rho_j^2} + \Pi_{ij} \right) \frac{\partial W_{ij}}{\partial x_i^\beta} \tag{5.14}$$

$$\frac{De_i}{Dt} = \frac{1}{2} \sum_{j=1}^{N} m_j \left(\frac{p_i}{\rho_i^2} + \frac{p_j}{\rho_j^2} + \Pi_{ij} \right) \left(v_i^\beta - v_j^\beta\right) \frac{\partial W_{ij}}{\partial x_i^\beta} + \frac{1}{\rho_i} \tau_i^{\alpha\beta} \varepsilon_i^{\alpha\beta} + H_i \tag{5.15}$$

where Π_{ij} is the artificial viscosity and H_i is the artificial heating [[56],[62],[63]].

In Figure 5.2, the basic steps used in each computation cycle in the AUTODYN SPH solver are shown [64].

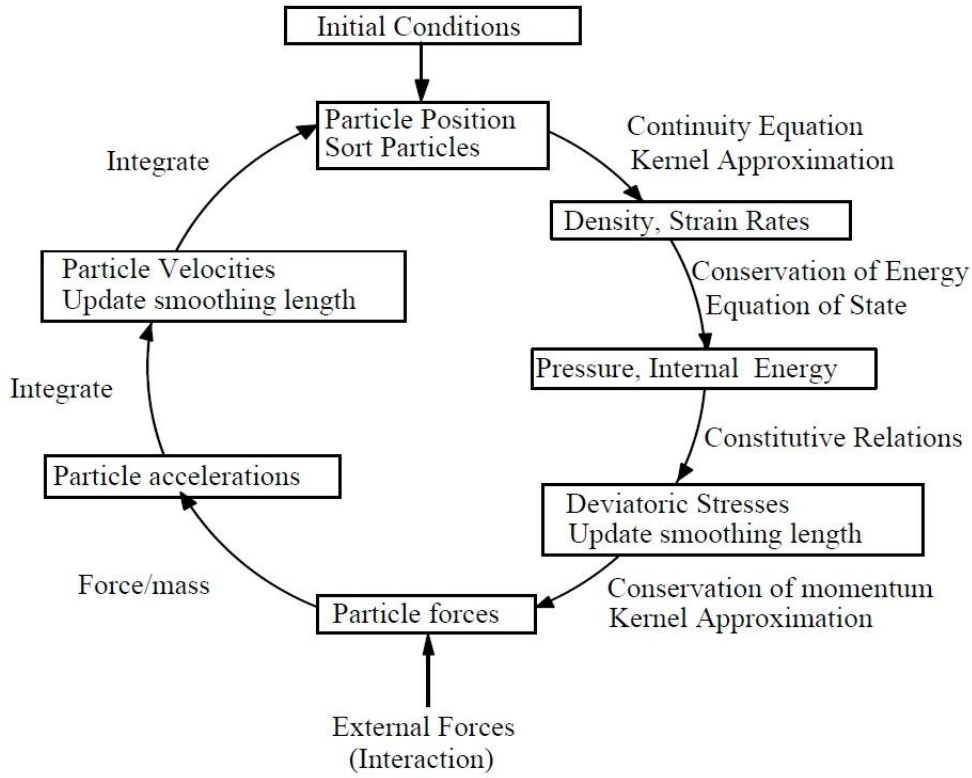

Figure 5.2 Computational cycle for the SPH in AUTODYN [64].

5.4. Material modelling

In this section the models used for the volumetric response (equation of state, see chapter 2) and the resistance to distortion (constitutive equation) in the numerical simulations are briefly described.

The composite material was modelled using the AMMHIS (advanced material model for hypervelocity impact simulation) material model available in ANSYS AUTODYN [[65],[66]].

Composite materials used in this work are orthotropic materials, and thus have three orthogonal planes of symmetry. Directions normal to the planes of symmetry correspond to the three principal directions of an orthotropic material. For homogenous materials the volumetric response and the ability to carry shear loads are dealt separately by separating the strain into volumetric and deviatoric components. But, for anisotropic materials this is not appropriate, because for hydrostatic pressure strain is not uniform in all three directions and the deviatoric strain produces volumetric dilatation. In [67] an equation of state that couples deviatoric and volumetric response was derived.

The stress-strain relation for a linearly elastic orthotropic material is given as [50]:

$$\begin{bmatrix} \sigma_{11} \\ \sigma_{22} \\ \sigma_{33} \\ \sigma_{23} \\ \sigma_{31} \\ \sigma_{12} \end{bmatrix} = \begin{bmatrix} C_{11} & C_{12} & C_{13} & 0 & 0 & 0 \\ C_{21} & C_{22} & C_{23} & 0 & 0 & 0 \\ C_{31} & C_{32} & C_{33} & 0 & 0 & 0 \\ 0 & 0 & 0 & C_{44} & 0 & 0 \\ 0 & 0 & 0 & 0 & C_{55} & 0 \\ 0 & 0 & 0 & 0 & 0 & C_{66} \end{bmatrix} \begin{bmatrix} \varepsilon_{11} \\ \varepsilon_{22} \\ \varepsilon_{33} \\ \varepsilon_{23} \\ \varepsilon_{31} \\ \varepsilon_{12} \end{bmatrix} \tag{5.16}$$

where σ_{ij} are the stress components, ε_{ij} are the strain components, and C_{ij} are the stiffness matrix components. Components of the stiffness matrix can be calculated from the elastic material constants, E_i, v_{ij} and G_{ij}.

In order to include non-linear shock effects in the above linear relations, it is desirable to separate the volumetric (thermodynamic) response of the material from its ability to carry shear loads (strength). To this purpose it is necessary to split the total strain into volumetric (ε_v) and deviatoric (ε_{ij}^d) components. The volumetric strain is defined as:

$$\varepsilon_{vol} = \varepsilon_{11} + \varepsilon_{22} + \varepsilon_{33} \tag{5.17}$$

Using equations (5.16) and (5.17), the linear elastic stress-strain relation for an orthotropic material can be expressed as

$$\begin{bmatrix}\sigma_{11}\\ \sigma_{22}\\ \sigma_{33}\\ \sigma_{23}\\ \sigma_{31}\\ \sigma_{12}\end{bmatrix}=\begin{bmatrix}C_{11} & C_{12} & C_{13} & 0 & 0 & 0\\ C_{21} & C_{22} & C_{23} & 0 & 0 & 0\\ C_{31} & C_{32} & C_{33} & 0 & 0 & 0\\ 0 & 0 & 0 & C_{44} & 0 & 0\\ 0 & 0 & 0 & 0 & C_{55} & 0\\ 0 & 0 & 0 & 0 & 0 & C_{66}\end{bmatrix}\begin{bmatrix}\frac{1}{3}\varepsilon_{vol}+\varepsilon_{11}^{d}\\ \frac{1}{3}\varepsilon_{vol}+\varepsilon_{22}^{d}\\ \frac{1}{3}\varepsilon_{vol}+\varepsilon_{33}^{d}\\ \varepsilon_{23}^{d}\\ \varepsilon_{31}^{d}\\ \varepsilon_{12}^{d}\end{bmatrix} \tag{5.18}$$

Using the definition of the pressure as the average of the direct stresses:

$$P=-\frac{1}{3}\left(\sigma_{11}+\sigma_{22}+\sigma_{33}\right) \tag{5.19}$$

and substituting the direct stresses from (5.18) into equation (5.19) the following expression for the pressure is obtained

$$\begin{aligned}P=&-\frac{1}{9}\left[C_{11}+C_{22}+C_{33}+2\left(C_{12}+C_{23}+C_{31}\right)\right]\varepsilon_{vol}-\frac{1}{3}\left[C_{12}+C_{23}+C_{31}\right]\varepsilon_{11}^{d}\\ &-\frac{1}{3}\left[C_{21}+C_{22}+C_{23}\right]\varepsilon_{22}^{d}-\frac{1}{3}\left[C_{31}+C_{32}+C_{33}\right]\varepsilon_{33}^{d}\end{aligned} \tag{5.20}$$

From equation (5.20) the contribution to the pressure of volumetric and deviatoric components of strain can be clearly identified. The first term on the right hand side of (5.20) can be used to define the volumetric (thermodynamic) response of an orthotropic material in which the effective bulk modulus of the material *K'* is given as:

$$K'=\frac{1}{9}\left[C_{11}+C_{22}+C_{33}+2\left(C_{12}+C_{23}+C_{31}\right)\right] \tag{5.21}$$

The first term on the right hand side of (5.20) represents the linear relationship between the pressure and the volumetric strain. In order to account for the non-linear relationship between pressure and volumetric strain, the first term on the right hand side of (5.20) is replaced by a non-linear relation between the pressure and volumetric strain. To this end the following polynomial equation of state is used instead of the first term on the right hand side of equation (5.20):

$$P=K'\varepsilon_{vol}+A_2\left(\varepsilon_{vol}\right)^2+A_3\left(\varepsilon_{vol}\right)^3+\left(B_0+B_1\varepsilon_{vol}\right)\rho_0 e \tag{5.22}$$

where A_2, A_3, B_0 and B_1 are material constants obtainable from inverse flyer plate tests, ρ_0 is the initial density and e is the specific internal energy.

Both for the Surlyn® 8940 ionomer and for the aluminium the volumetric response was described by a ‘‘Shock’’ equation of state of the following form [55]:

$$p = p_H + \Gamma\rho\left(e - e_H\right) \tag{5.23}$$

In equation (5.23) is assumed that $\Gamma\rho = \Gamma_0\rho_0 = constant$ and

$$p_H = \frac{\rho_0 C_0^2\left(1+\mu\right)}{\left[1-\left(s-1\right)\mu\right]^2} \tag{5.24}$$

$$e_H = \frac{1}{2}\frac{p_H}{\rho_0}\left(\frac{\mu}{1+\mu}\right) \tag{5.25}$$

In (5.23), (5.24) and (5.25) Γ is the Gruneisen Gamma, ρ is the current density, C_0 is the bulk sound speed, μ is the compression ($\mu = (\rho/\rho_0) - 1$) and s is the slope of the $u_p - U_s$ curve (u_p – particle velocity, U_s – shock velocity).

The strength response of aluminium is modelled using the Johnson-Cook strength model [68]. In this model the yield stress is defined as:

$$Y = \left[A + B\varepsilon_p^n\right]\left[1 + C\log\varepsilon_p^*\right]\left[1 - T_H^m\right] \tag{5.26}$$

where A, B, C, n and m are material constants, ε_p is the effective plastic strain, ε_p* is the normalized effective plastic strain rate, and T_H is the homologous temperature [$T_H=(T-T_{room})/(T_{melt}-T_{room})$]. The Johnson-Cook model is suitable for materials subjected to large strains, high strain rates and high temperatures.

The ionomer strength response of the ionomer is modelled through the isotropic hardening plasticity model.

5.5. Description of the numerical models

Numerical simulations of tests on single panels were performed. Therefore, four simulations for panel A and panel C were done, while two simulations were performed for panel B. For panel C shots 8980, 8982, 8984 and 9045 were reproduced. For panel A the simulated tests were 8981, 8983, 8985 and 9044. The ionomer tests modelled were 8992, 9046 and 9047.

The simulations were carried out in AUTODYN-2D, and an axisymmetric approximation was used for all simulations. The radius for the target in the numerical model was chosen to obtain a target with the area that corresponds to the experimental target (the area of the target between the support plates). This resulted in a radius of 61 mm for all targets in the numerical models. All other parameters correspond to the experiment conditions defined in the previous chapters.

The projectile was given an initial velocity corresponding to that of the test that was simulated, and can be found for each test in Table 4-3.

For models involving panel A 0.15 mm diameter SPH particles were used. When panels C were modelled the SPH particle size used was 0.12 mm to accommodate the Twaron® layers, and Figure 5.3 shows a detail of the numerical model for panel C. Panels B were discretized with a particle size of 0.1 mm.

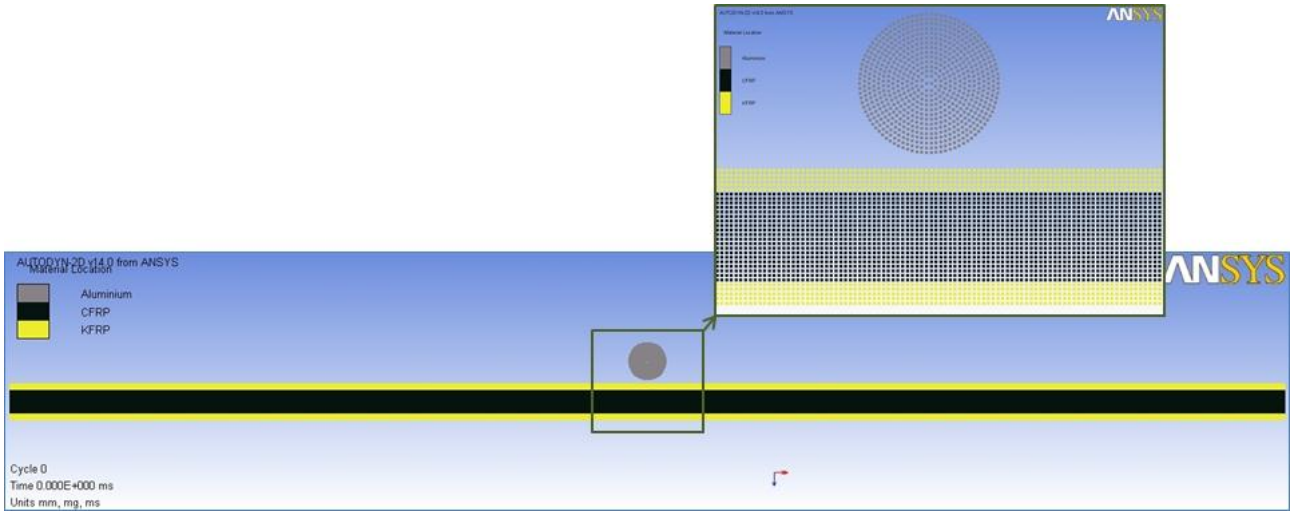

Figure 5.3 Numerical model of panel C in AUTODYN ANSYS.

In AUTODYN the laminas in the composite laminate are not modelled individually, instead they are smeared out in through-the-thickness direction, which results in a homogenous orthotropic material.

For the composite materials used in this study (CFRP and Twaron®) there were almost no material properties available, or just a few of them. Therefore, for Twaron® the material data set for Kevlar® [69], which is also an aramid fibre composite material, available in the AUTODYN material library was used.

For CFRP the elastic properties of the laminate and the unidirectional lamina strengths were predicted from the constituent material properties following the guidelines and procedures given in [[70]-[73]]. But, since few data for the fibres and matrix were available from the manufacturer,

most of the unknown properties were assumed from similar materials found in the literature, and are given in Table 5-1.

Table 5-1 CFRP laminate constituent properties.

Property	Value
Fiber	
Fiber type: T600	
Density (g/cm^3)	1.79
Longitudinal tensile modulus (GPa)	230
Transverse tensile modulus (GPa)	15
Poisson's ratio	0.2
Transverse Poisson's ratio	0.0714
Shear modulus (GPa)	15
Transverse shear modulus (GPa)	7
Longitudinal tensile strength (MPa)	4136.4
Longitudinal compressive strength (MPa)	3000
Resin	
Resin type: REM epoxy resin	
Density (g/cm^3)	1.20
Tensile modulus (GPa)	3.36
Poisson's ratio	0.35
Shear modulus (GPa)	1.244
Tensile strength (MPa)	60
Compression strength (MPa)	150
Shear strength (MPa)	55
Fracture energy (J/m^2)	240

From the data in Table 5-1 the elastic properties of the composite material were derived by a micromechanics theory. The bridging micromechanics model described in [[71],[72]] was used for this purpose. Then, classical laminate theory (CLT) and Hooke's law for an orthotropic composite [[50],[74]] were used to derive the CFRP laminate stiffness properties form the lamina elastic properties.

After determining the laminate stiffness properties, the data for the equation of state had to be derived. This was done following the procedure in [70], where a generalised *Us-Up* relationship for CFRP laminates is given. For this relationship a *p*-wave sound of speed of the laminate was needed, and it was measured with the ultrasound system as 3050 m/s for the laminate used in this study.

Finally, the strengths of the laminate were estimated from the strengths of the CFRP unidirectional lamina, which were predicted using the data in Table 5-1 and the strength of materials equations, see [73]. The failure stress in the thickness direction of the laminate was calculated as the stress at 2% deformation in the thickness direction.

The above procedure was coded in a MATLAB script file in order to predict the CFRP laminate stiffness properties and the single lamina strengths. The script file is given in Appendix 1 together with the input file. The predicted data used in the simulations is given in Table 5-2.

Table 5-2 Material properties for the CFRP laminates used in the numerical models.

Parameter	Value
Equation of state: Orthotropic	
Reference density (g/cm^3)	1.554
Young modulus 11 (kPa)	9.531E+006
Young modulus 22 (kPa)	7.425E+007
Young modulus 33 (kPa)	7.425E+007
Poisson ratio 12	0.042500
Poisson ratio 23	0.030000
Poisson ratio 31	0.331000
Shear modulus 12 (kPa)	3.878E+006
Shear modulus 23 (kPa)	4.791E+006
Shear modulus 31 (kPa)	3.878E+006
Volumetric response: Polynomial	
Bulk modulus A_1 (kPa)	2.010E+007
Parameter A_2 (kPa)	1.769E+007
Parameter A_3 (kPa)	2.769E+007
Parameter B_0	2.808
Parameter B_1	2.808
Parameter T_1 (kPa)	2.010E+007
Parameter T_2 (kPa)	1.769E+007
Reference temperature (K)	293.0
Strength: Elastic	
Shear modulus (kPa)	4.791E+006
Failure: Material Stress	
Tensile failure stress 11 (kPa)	1.900E+005
Tensile failure stress 22 (kPa)	1.120E+006
Tensile failure stress 33 (kPa)	1.120E+006
Maximum shear stress 12 (kPa)	4.280E+004
Maximum shear stress 23 (kPa)	4.600E+004
Maximum shear stress 31 (kPa)	4.280E+004
Post Failure Option: Orthotropic	
Residual shear stiffness fraction	0.2
Maximum Residual Shear Stress (kPa)	4.000E+004
Failed in 11, failure mode	11 only
Failed in 22, failure mode	22 only
Failed in 33, failure mode	33 only
Failed in 12, failure mode	12 & 22 only
Failed in 23, failure mode	Bulk
Failed in 31, failure mode	31 & 33 only

The data set for the ionomer used in the simulations is given in Table 5-3. As could be seen in chapter 4 the ionomer undergoes phase transition when used alone in the impact tests in this study (e.g. test no. 8992, 9046, and 9047). This makes the Mie-Gruneisen (‘‘Shock’’) equation of state inappropriate, since this equation is only valid for solids. But, as only data for the ‘‘Shock’’ equation of state could be obtained, whether calculated, measured, or taken from similar materials, it was decided to use the ‘‘Shock’’ equation of state, as the only possibility. The material properties for the equation of state were obtained as follows. The Gruneisen constant (Γ) was computed through the following equation [8]:

$$\Gamma = \frac{3KV\alpha}{C_v} \tag{5.27}$$

where K is the bulk modulus computed from the Young's modulus (E) and the Poisson's ratio (v) ($K=E/(3\cdot(1-2v))$, $V=1/\rho$ is the specific volume, α is thermal expansion coefficient, and Cv the specific heat. The values of E, ρ and α were taken from manufacturer data sheet as 350 MPa, 950 kg/m^3 and 0.0001 μm/m°C, respectively. The values of Cv and v were taken from the representative values for polymers, and equal 1600 J/kgK and 0.4, respectively.

Table 5-3 Material properties for Surlyn8940 used in the numerical models.

Parameter	Value
Equation of state: Shock	
Reference density (g/cm^3)	0.950
Gruneisen coefficient	0.613
Parameter C1 (m/s)	2.050e+003
Parameter S1	1.5394
Reference temperature (K)	293.0
Specific heat (J/kgK)	1.600E+03
Strength: Multilinear Hardening	
Shear modulus (kPa)	1.250E+05
Eff. plastic strain #1	0.000000
Eff. plastic strain #2	0.0303
Eff. plastic strain #3	0.1026
Eff. plastic strain #4	0.1234
Eff. plastic strain #5	0.1716
Eff. plastic strain #6	0.3302
Eff. plastic strain #7	0.5302
Eff. plastic strain #8	0.6968
Eff. plastic strain #9	0.8072
Eff. plastic strain #10	0.8678
Stress #1 (kPa)	2.7000E+04
Stress #2 (kPa)	2.9885E+04

Stress #3 (kPa)	2.9885E+04
Stress #4 (kPa)	3.1034E+04
Stress #5 (kPa)	3.1034E+04
Stress #6 (kPa)	3.7931E+04
Stress #7 (kPa)	5.0575E+04
Stress #8 (kPa)	5.8046E+04
Stress #9 (kPa)	6.4942E+04
Stress #10 (kPa)	7.2414E+04
Failure: Plastic Strain	
Plastic strain	0.8678

In Table 5-3 the bulk sound speed C_0 was measured with the ultrasound system, while the slope *S1* is set equal to the values regarding polymers in [75], more specifically Polyethylene.

The plastic strain vs. stress data for strength modelling was taken from [76], where Surlyn 8940 stress strain curves up to the strain rate of 500 mm/s were obtained through mechanical testing. Anyway, it has to be noted that this strain rate is not representative for hypervelocity impacts, but the data was used because no other data was available.

The material data used for the aluminium projectile is given in Table 5-4 and is provided in [[77],[78]].

Table 5-4 Material properties for Aluminium 1100 used in the numerical models.

Parameter	Value
Equation of state: Shock	
Reference density (g/cm^3)	2.710
Gruneisen coefficient	1.970
Parameter C1 (m/s)	5.386E+03
Parameter S1	1.339
Reference temperature (K)	293.0
Specific heat (J/kgK)	920.0
Strength: Johnson Cook	
Shear modulus (kPa)	2.52930E+07
Yield stress, A (kPa)	1.48361E+05
Hardening constant, B (kPa)	3.45513E+05
Hardening exponent, n	0.183
Strain rate constant, C	0.001
Thermal softening exponent, m (K)	0.859
Melting temperature	893.0
Ref. strain rate (s^{-1})	1.000
Failure: Johnson Cook	
Damage constant, D1	0.0710
Damage constant, D2	1.2480

Damage constant, D3	-1.1420
Damage constant, D4	0.0097
Damage constant, D5	0.0000
Melting temperature (K)	893.00
Ref. strain rate (s^{-1})	1.0000

5.6. Numerical results

In order to validate the numerical models, results obtained numerically are compared to the experimental values. The comparison is based on the damage of the samples and the velocity of the projectile residue after the perforation of the target.

The quantities used for the comparison between the numerical models and the experiments are the following:

- The diameter of the hole through the thickness of the sample shown in Figure 5.4 is compared to the external hole measured on the tested sample (see section 4.4.4.) for the composite materials (panels A and C)
- The numerically obtained maximal damage extension in the material (see Figure 5.4 and Figure 5.5) is compared to the damage detected with the ultrasound system for the composite panels, and to the external hole diameter for the ionomer
- The velocity of the projectile residue after the perforation of the target obtained with the simulation is compared to the velocity of the biggest fragment measured from the high speed camera video footage

It has to be noted that the extended damage in the fibre direction observed in the top and bottom surfaces of panels A cannot be reproduced with the numerical models presented here. This is because such damage is strictly related to the unidirectional superficial lamina and to its orientation, and it is propagating in the direction of the fibres of that lamina, while in AUTODYN the laminas in the composite laminate are not modelled individually (they are smeared out in through-the-thickness direction which results in a homogenous orthotropic material), which makes it impossible to represent such damage.

The scope of numerically modelling the ionomer was not to reproduce the self-healing process, since no model is available to do so, but rather to simulate only the initial deformation preceding the self-healing response. From the micrograph of shot 8813 (see Figure 4.12) it is visible that around the sealed hole there are no signs of any damage or plastic deformation. So from the micrograph the damaged region (any region that has undergone significant changes, whether through melting and re-solidification or plastic deformation) is clearly distinguished from the undamaged region.

Therefore it is concluded that the external hole for the ionomer defined in chapter 4 can be considered as the maximum damage extension, and the aim of simulating the impacts on the ionomer was to see if this damage could be predicted. The value of the external hole taken from the simulations is shown in Figure 5.5. Furthermore, the velocity of the projectile remnant measured experimentally was compared to the value obtained numerically.

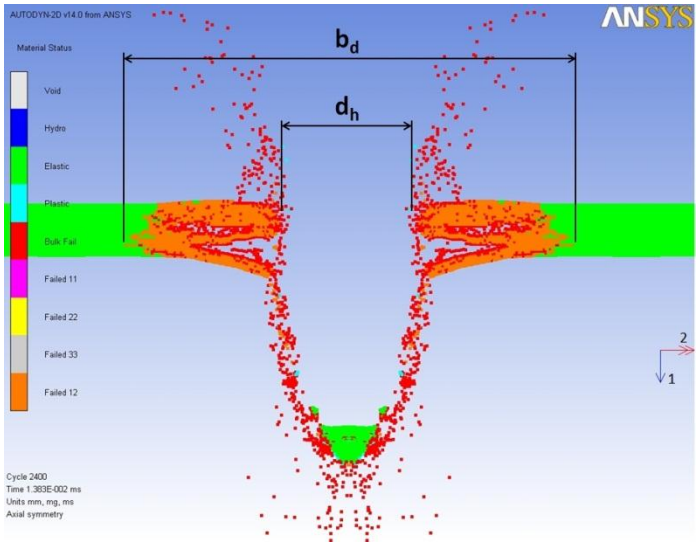

Figure 5.4 Numerical simulation of impact on panel A and definition of numerical damage measures b_d and d_h in the numerical models for the structural layers.

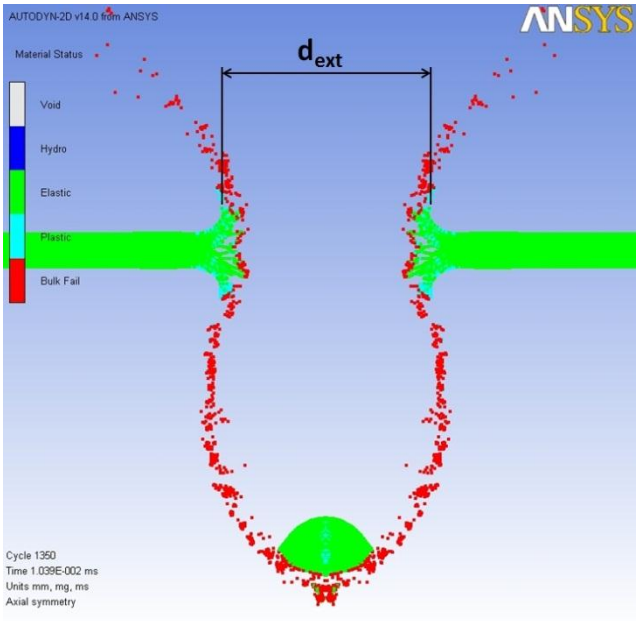

Figure 5.5 Numerical simulation of impact on ionomer and definition of the numerically measured external hole.

In Figure 5.6 the residual velocity of the projectile obtained numerically and experimentally for shots on the panels A is shown. Good results are obtained from the simulations for more energetic impacts, where the difference is within 10%, while for shot 8983 a larger disagreement of the

numerical value with respect to the experimental is obtained. Anyway it seems that the numerical data trend follows the experimental data trend.

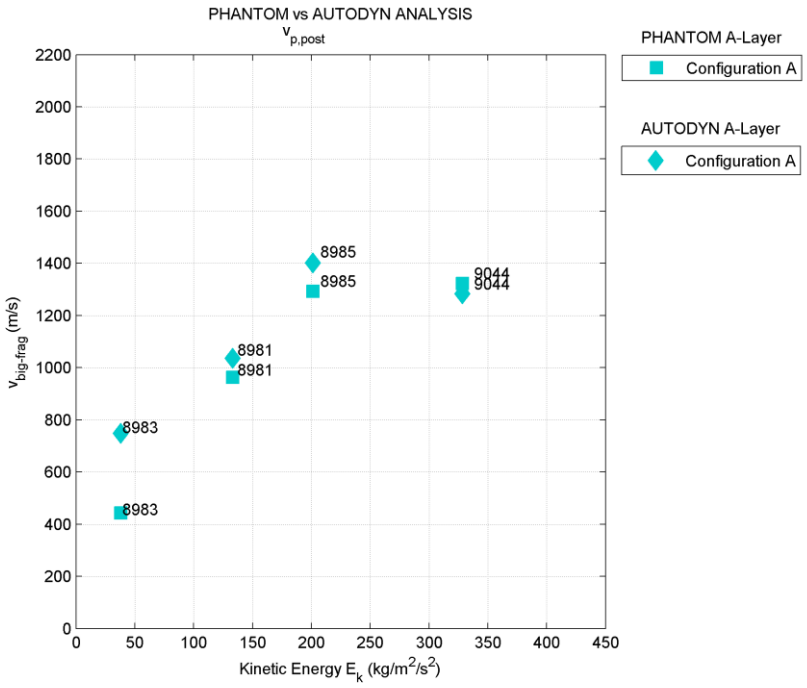

Figure 5.6 Projectile residual velocity: experiments vs. simulations for panels A.

In Figure 5.7 the projectile residual velocity for shots on panels C is shown. Only for shot 8982 very similar results to the experiments are obtained, while for the other cases almost a constant difference is of ~200m/s is observed. Also for panels C the experimental trend seems to be reproduced relatively well, especially considering the uncertainties in the material properties.

For tests on panel B, only for two shots the velocity of the projectile fragment was available. In both of those shots the velocity obtained numerically is very similar to the experimentally measured velocity (see Figure 5.8).

The maximal damage extension detected and measured with the ultrasound system is compared to the maximal damage obtained numerically in Figure 5.9 for panel A and in Figure 5.10 for panel C. The hole diameters defined in Figure 4.34, Figure 4.35 and Figure 5.4 are compared in Figure 5.11 and Figure 5.12 for panels A and C, respectively. The damage comparison for panel A shows somewhat more discrepancy than the velocity results. In Figure 5.9 the difference goes up to ~30% for shot 8981, and for shot 8985 the results vary only 10%. While the damage extension is underestimated by the numerical simulations, values for d_h are overestimated (see Figure 5.11). Beside the discrepancies between the numerical and experimental results, the trend reproduced with the numerical models appears to follow fairly well the experimental trend. As far as the damage in Figure 5.10 and Figure 5.12 for the panels C is concerned, similar observations can be made as for

the panel A with regard to comparison of simulations and experiments. It is noted that good agreement between numerical and experimental values for dh in Figure 5.12 are found.

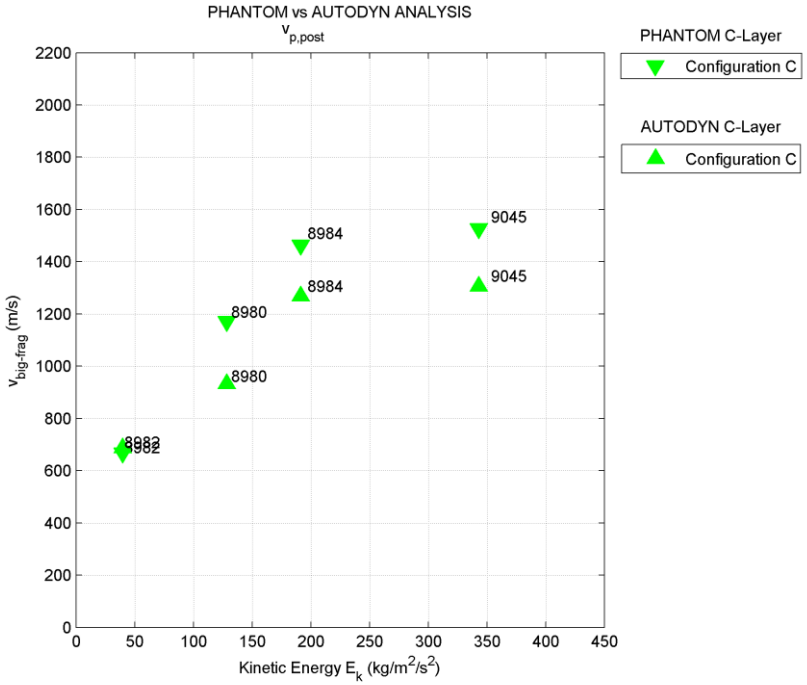

Figure 5.7 Projectile residual velocity: experiments vs. simulations for panels C.

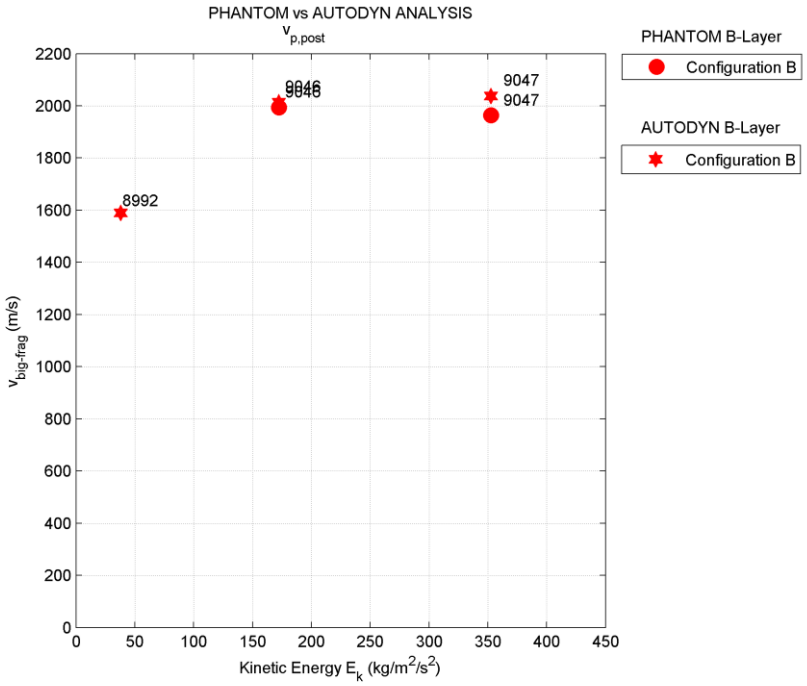

Figure 5.8 Projectile residual velocity: experiments vs. simulations for panels B.

The external hole for the ionomer (which is equal to the maximal damage extension) plotted in Figure 5.13 is largely overestimated. Values three times bigger than those found in experimental tests were predicted by the simulations. This is probably caused by the limitations of the material models used, as well by the material properties applied. Mechanical properties from high strain-rate tests, and also a more appropriate equation of state (e.g. Tillotson EOS) with the accompanying material data, could be used to provide better results.

With very limited material data obtained through mechanical testing, fairly good results are obtained for the composite materials, which can be used for preliminary studies, for example as an aid to test matrix definition, before going on to experiment execution. For the ionomer, the velocity comparisons were very similar between experiments and simulations, but the damage was grossly overestimated.

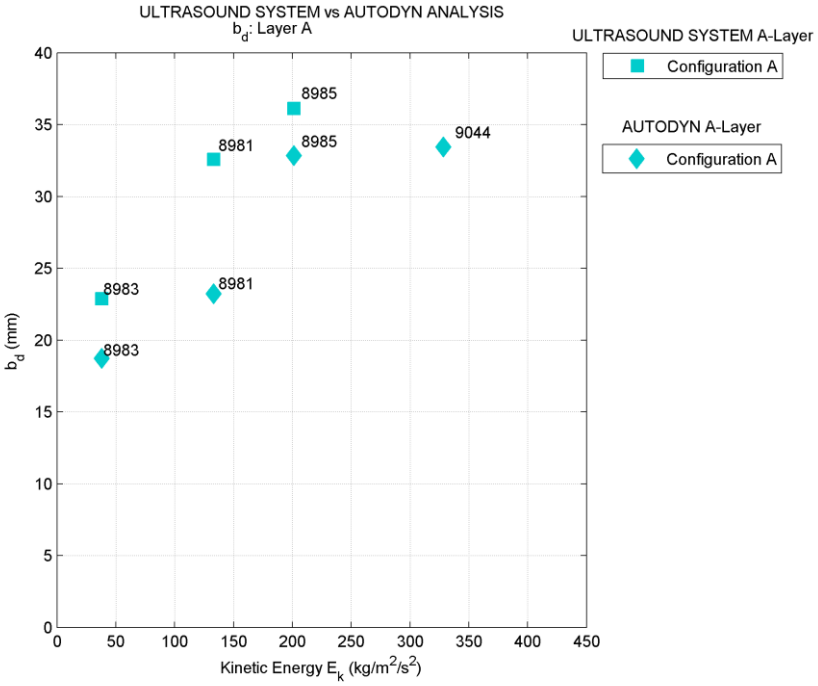

Figure 5.9 Comparison of damage extension (b_d) measured with the ultrasound system with the numerically obtained values for panels A.

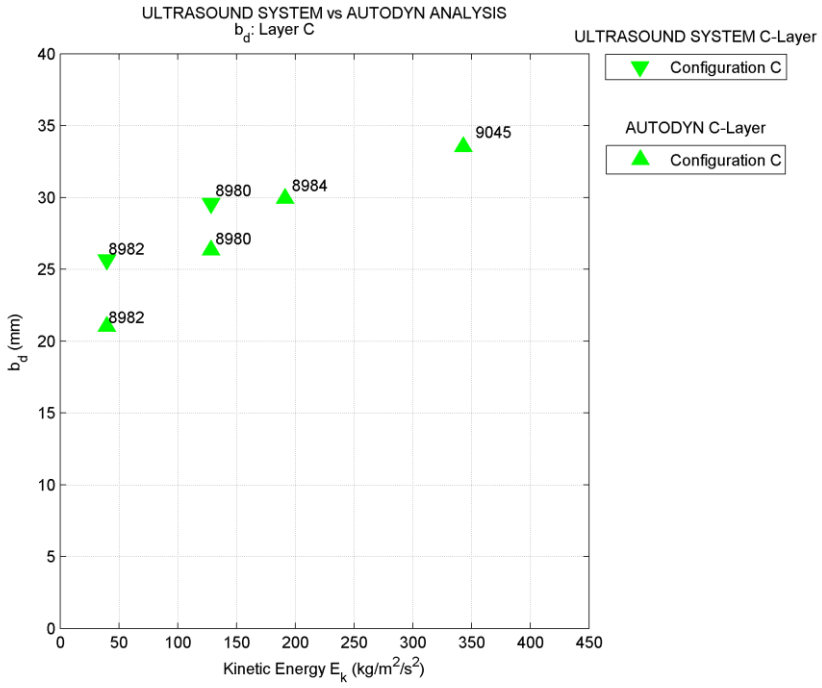

Figure 5.10 Comparison of damage extension (b_d) measured with the ultrasound system with the numerically obtained values for panels C.

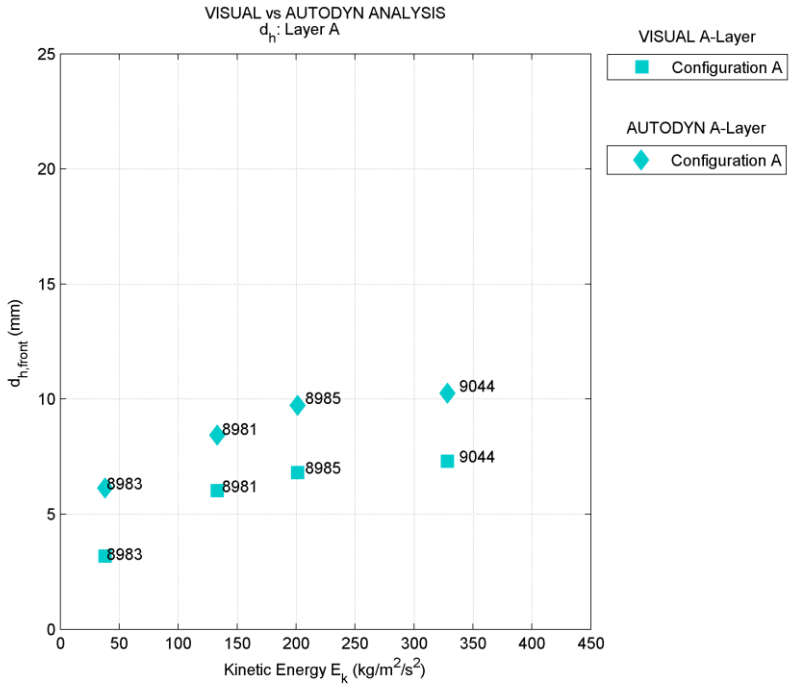

Figure 5.11 External hole diameter ($d_{h,front}$) comparison for panels A: experiments vs. simulations.

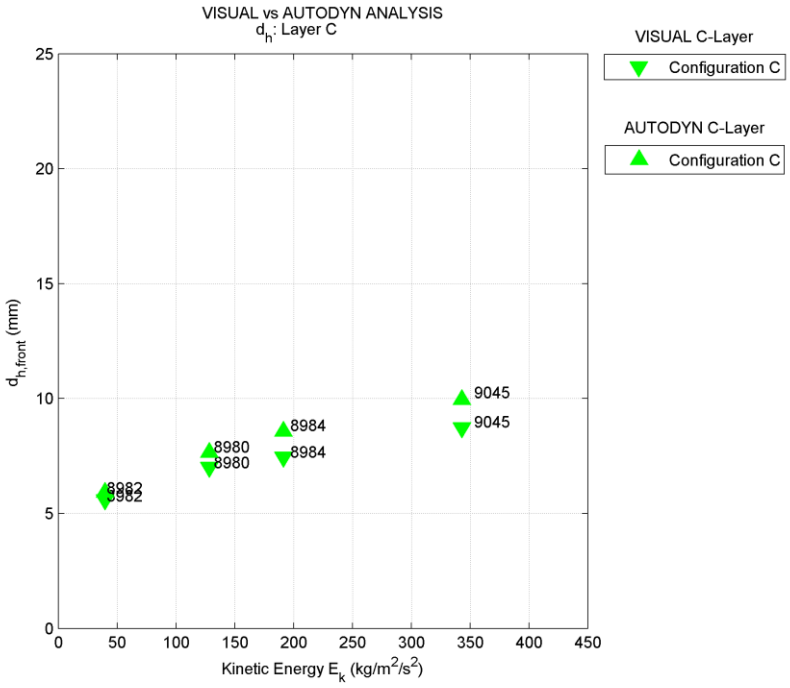

Figure 5.12 External hole diameter ($d_{h,front}$) comparison for panels C: experiments vs. simulations.

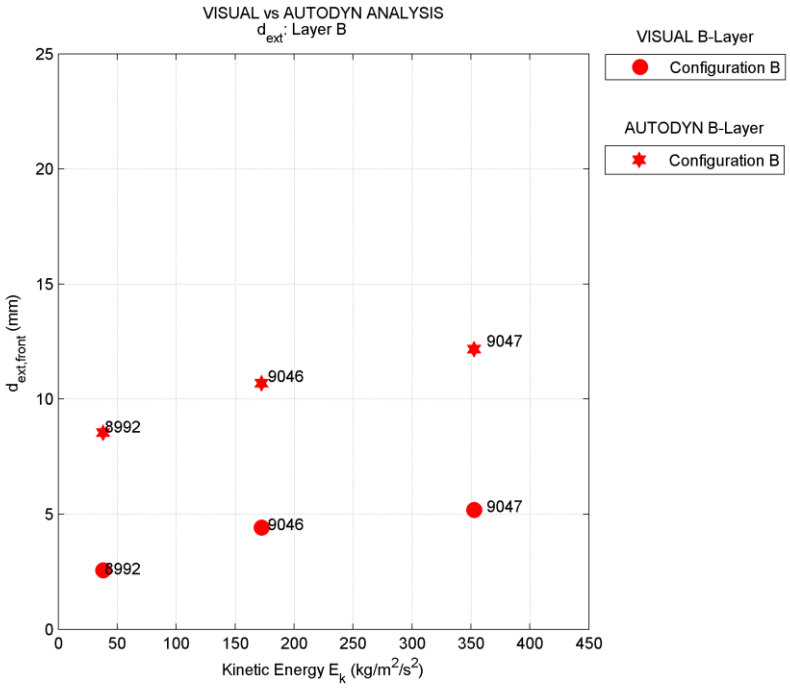

Figure 5.13 External hole diameter ($d_{ext,front}$) comparison for panels B: experiments vs. simulations.

6. Conclusions

In this work the impact behaviour of a multifunctional panel, when impacted by aluminium spheres at velocities ranging from 1 km/s to 4 km/s, has been studied. Anyway, throughout the study most impacts were in the range of 2 km/s to 2.5 km/s. The studied multifunctional panels consisted of one or two structural layers made of composite materials and a self-healing layer made of ethylene-co-methacrylic acid ionomer (panel B). One structural layer was a CFRP laminate (panel A), while the other was a CFRP laminate covered on front and back faces with aramid fibre fabric / epoxy composite (panel C). The structural and self-healing layers were tested alone, and then they were coupled together in various two-layers and three-layers configurations. In this way a variety of samples was tested and compared. The impact behaviour was characterized by evaluating the momentum transfer to the witness plate mounted on a ballistic pendulum placed behind the target, the velocity of the biggest and fastest fragment in the debris cloud, the damage distribution on the witness plate, the damage size, and the self-healing performance.

The ionomer was compared to the aluminium for bumper applications. It was concluded that it may be unsuitable for such application due to low projectile fragmentation capability.

Both the ionomer and composite panels protection capabilities were observed to be very low in terms of projectile fragmentation. Very similar behaviour of panels A and C for momentum transfer and fragments velocity was found.

For two-layers configurations, it was observed that less momentum is transferred if the ionomer is on the back side of the assembly (with respect to the projectile path). It was further noted that this response varies for different structural layers used in front of the ionomer.

Among all tested configurations it was found that the three-layers sandwich configurations (with the ionomer layer between two structural layers) transfer the least amount of momentum to the backing witness plate, and also the fragments velocities are lower than in the other configurations per unit areal density. Similar behaviour of the two structural elements analysed for momentum transfer and fragments velocity was found.

Regarding the damage of the panels, it was observed that only a small area slightly bigger than the projectile was damaged by the impact (considering also the self-healed region as damaged, due to the changes it undergoes). A high tendency of damage propagation in the fibres direction, mainly through matrix fracture, is observed for the composite panels. This suggests that for impact applications a woven composite is much better with respect to unidirectional laminas if superficial damage is to be kept as small as possible.

The self-healing effectiveness varied a lot, and inconclusive results were obtained. Panels AB and BA both sealed the hole successfully for impact of spheres with a diametr of 3.5 mm and for impact velocity in the range from 2 km/s to 2.5 km/s. Instead for larger diameters the self-healing was ineffective. The effect of structural layer is evidenced as panels CB and BC performance was poorer than for panels AB and BA, for the configurations used herein. More experiments should be performed to further test the self-healing with different ionomer layer thicknesses in the unrepaired samples.

Numerical models of the tests on single layers were set up in ANSYS AUTODYN and numerical simulations were performed. Furthermore, the numerical results were compared to the experimental results, in order to validate the numerical models. No self-healing was modelled, since such material models were not available. The mechanical properties of the target materials were mainly assumed from similar materials in the literature. Fairly good results were obtained for the projectile fragment velocity when compared to the experiments. For the damage comparison between simulations and experiments more discrepancy was present, which varied from 30% to smaller values for the composite materials. For the ionomer the numerical simulations grossly overestimated the damage, due to inadequate material models.

References

[1] Zukas J.A., Nicholas T., Swift H.F., Greszczuk L.B., Curran D.R.: *Impact Dynamics*, John Wiley & Sons, New York, (1982).

[2] Kolsky H.: *Stress Waves in Solids*, Dover, New York, (1963).

[3] Achenbach J.D.: *Wave Propagation in Elastic Solids*, North-Holland, Amsterdam, (1973).

[4] Zukas J.A. (ed): *High Velocity Impact Dynamics*, John Wiley & Sons, New York, (1990).

[5] Meyers M.A. *Dynamic Behavior of Materials*, John Wiley & Sons, New York, (1994).

[6] Drumheller D.S.: *Introduction to Wave Propagation in Nonlinear Fluids and Solids*, Cambridge U. Press, Cambridge, (1998).

[7] Wasley R.J.: *Stress Wave Propagation in Solids: An Introduction*, Marcel Dekker, New York, (1973).

[8] Zukas J.A.: *Introduction to Hydrocodes*, Elsevier Ltd, Oxford, (2004).

[9] Cooper P.W.: *Explosives Engineering*, VCH-Wiley, New York, (1996).

[10] Nemat-Nasser S., Nemat-Nasser S.,Plaisted T., Starr A., Amirkhizi A.V. ‘‘Multifunctional Materials’’, in Bar-Cohen Y. (ed.), *Biomimetics*, CRC Press, Boca Raton, pp. 309-340, (2006).

[11] Gibson R.F. ‘‘A review of recent research on mechanics of multifunctional composite materials and structures’’, *Composite Structures*, vol. 92, pp. 2793-2810, (2010).

[12] Elzey D.M., Sofla A.Y.N., Wadley H.N.G. ‘‘A shape memory-based multifunctional structural actuator panel’’, *Int J of Solids and Structures*, vol. 42, pp. 1943-1955, (2005).

[13] Williams H.R., Trask R.S., Bond I.P. ‘‘Self-healing sandwich panels: Restoration of compressive strength after impact’’, *Composite Science and Technology*, vol. 66, pp. 3171-3177, (2008).

[14] Roberts S.C., Aglietti G.S. ‘‘Structural performance of a multifunctional spacecraft structure based on plastic lithium-ion batteries’’, *Acta Astronautica*, vol. 67, pp. 424-439, (2010).

[15] Lin Y., Sodano H.A. ‘‘Fabrication and Electromechanical Characterization of a Piezoelectric Structural Fiber for Multifunctional Composites’’, *Advanced Functional Materials*, vol.19, pp. 592-598, (2009).

[16] Ghosh S.K. ‘‘Self-healing Materials: Fundamentals, Design Strategies, and Applications’’, in Ghosh S.K. (ed.), *Self-healing Materials*, Wiley-VCH Verlag GmbH & Co. KGaA, Weinheim, pp. 1-28, (2009).

[17] White S.R., Sottos N.R., Geubell P.H., Moore J.S., Kessler M.R., Sriram S.R., Brown E.N., Viswanathan S. ‘‘Autonomic healing of polymer composites’’, *Nature*, vol.409, pp. 794-797, (2001).

[18] Pang J.W.C., Bond I.P. ‘‘‘Bleeding composites’-damage detection and self-repair using a biomimetic approach’’, *Composites Part A: Applied Science and Manufacturing*, vol. 36, pp. 183-188, (2005).

[19] Trask R.S., Bond I.P. ‘‘Biomimetic self-healing of advanced composite structures using hollow glass fibres’’, *Smart Materials and Structures*, vol. 15, pp. 704-710, (2006).

[20] Toohey, K.S., Hansen, C., Sottos, N.R., Lewis, J.A. and White, S.R. ‘‘Delivery of two-part self-healing chemistry via microvascular networks’’, *Advanced Funcional Materials*, vol. 19, pp. 1399-1405, (2009).

[21] Hamilton A.R., Sottos N.R., White S.R. ‘‘Self-healing of Internal Damage in Synthetic Vascular Materials’’, *Advance Materials*, vol. 22, pp. 5159-5163, (2010).

[22] Chen X., Matheus A.D., Kanji O., Mal A., Shen H., Nutt S.R., Sheran K., Wudl F. ‘‘A Thermally Re-mendable Cross-Linked Polymeric Material’’, *Science*, vol. 295, pp. 1698-1702, (2002).

[23] Park J.S., Takahashi K., Guo Z., Wang Y., Bolanos E., Hamman-Schaffner C., Murphy E., Wudl F.,Hahn H.T. ‘‘Towards Development of Self-Healing Composite using a Mendable Polymer and Resistive Heating’’, *Journal of Composite Materials*, vol. 42, pp. 2853-2867, (2008).

[24] Cordier P., Tournilhac F., Soulié-Ziakovic C., Leibler L. ‘‘Self-healing and thermoreversible rubber from supramolecular assembly’’, *Nature*, vol. 451, pp. 977-980, (2008).

[25] Otsuka K., Wayman C.M.: *Shape Memory Materials*, Cambridge University Press, Cambridge, 1998.

[26] Rahmathullah M.A.M., Palmese G.R. ‘‘Crack-healing behavior of epoxy-amine thermosets’’, *Journal of Applied Polymer Science*, vol. 113, pp. 2191-2201, (2009).

[27] Wu D.Y., Meure S., Solomon D. ‘‘Self-healing polymeric materials: A review of recent developments’’, *Progress in Polymer Science*, vol. 33, pp. 479-522, (2008).

[28] Fall R. ‘‘Puncture reversal of ethylene ionomers-mechanistic studies’’, Master thesis, Virginia Polytechnic Institute and State University, Blacksburg, USA, (2003).

[29] Kalista S.J. ‘‘Self-healing of thermoplastic poly(ethylene-*co*-methacrylic acid) copolymers following projectile puncture’’, Master thesis, Virginia Polytechnic Institute and State University, Blacksburg, USA, (2003).

[30] Kalista S.J., Ward T.C., Oyetnuji Z. ‘‘Self-Healing Behaviour of Ethylene-Based Ionomers’’, *Proceedings of the 26th Annual Meeting of the Adhesion Society, Inc.*, pp 176-178, (2003).

[31] Kalista Jr S.J., Ward T.C., Oyetunji Z. ‘‘Self-Healing of Poly (Ethylene-co-Methacrylic Acid) Copolymers Following Projectile Puncture’’, *Mechanics of Advanced Materials and Structures*, vol. 14, pp. 391-397, (2007).

[32] Tant, M.R., Wilkes G.L. ‘‘Viscoelastic Behavior of Ionomers in Bulk and Solution’’, *Structure and Properties of Ionomers*, vol. 198, pp 191-226, (1987).

[33] Eisenberg A., Rinaudo M. ‘‘Polyelectrolytes and ionomers’’, *Polymer Bulletin*, vol. 24 (6), p 671, (1990).

[34] Eisenberg A., Hird B., Moore R. B., ‘‘A New Multiplet-Cluster Model for the Morphology of Random Ionomers’’, *Macromolecules*, vol. 23 (18), pp 4098-4107, (1990).

[35] Bellinger M., Sauer J.A., Hara M. ‘‘Tensile Fracture Properties of Sulfonated Polystyrene Ionomers. 1. Effect of Ion Content’’, *Macromolecules*, vol. 27, pp. 1407-1412, (1994).

[36] Rees R., ‘‘Ionomeric Thermoplastic Elastomers Early Research-Surlyn and Related Polymers’’ in Legge N.R., Holden G., Schroeder H.E. (eds.), *Thermoplastic Elastomers: a Comprehensive Review*, Carl Hanser Verlag, Munich, pp. 231-243, (1987).

[37] Tadano K., Hirasawa E., Yamamoto H., Yano S. ‘‘Order-Disorder Transition of Ionic Clusters in Ionomers’’, *Macromolecules*, vol. 22, pp. 226-233, (1989).

[38] Kalista Jr S.J. ‘‘Self-healing Ionomers’’, in Ghosh S.K. (ed.), *Self-healing Materials*, Wiley-VCH Verlag GmbH & Co. KGaA, Weinheim, pp. 73-100, (2009).

[39] Kalista S.J., Ward, T.C. “Thermal characteristics of the self-healing response in poly(ethylene-co methacrylic acid) copolymers”, *J. R. Soc. Interf.*, vol. 4, pp. 405–411, (2007).

[40] Angrilli F., Pavarin D., De Cecco M., Francesconi A. ‘‘Impact facility based upon high frequency two-stage light-gas gun’’, *Acta Astronautica*, vol. 53, pp. 185-189, (2003).

[41] Pavarin D., Francesconi A., Angrilli F. ‘‘A system to damp the free piston oscillations in a two-stage light-gas gun used for hypervelocity impact experiments’’, *Review of Scientific Instruments*, vol. 75, pp. 245-252, (2004).

[42] Francesconi A., Pavarin D., Bettella A., Angrilli F. ‘‘A special design condition to increase the performance of two-stage light-gas guns’’, *Int J of Imp Engng*, vol. 35, pp. 1510-1515, (2008).

[43] Denardo B.P. ‘‘Measurements Of Momentum Transfer From Plastic Projectiles To Massive Aluminum Targets At Speeds Up To 25,600 Feet Per Second’’, NASA (1962).

[44] Nysmith C.R:, Denardo B.P. ‘‘Experimental Investigation of the Momentum Transfer Associated With Impact into Thin Aluminum Targets’’, NASA tn-d-5492, A139253, (1969).

[45] Cipparone G., Bourne B., Orphal D., Goldsmith W. ‘‘Momentum exchange alteration in projectile/target impact’’, *Int J of Imp Engng*, vol. 27, pp. 691-707, (2002).

[46] Francesconi A., Pavarin D. ‘‘Spacecraft disturbances from HVI-TN3 evaluation of the impact tests results’’, ESA Contract no. 17854/03/NL/CH, (2006).

[47] Olympus NDT: *Phased Array Testing: Basic Theory for Industrial Applications*, Second Edition, Olympus NDT, Waltham, USA, (2012).

[48] Olympus NDT: *Introduction to Phased Array Ultrasonic Technology Applications: R/D Tech Guideline*, Olympus NDT, Waltham, USA, (2004.

[49] Olympus NDT: *Advances in Phased Array Ultrasonic Technology Applications*, Olympus NDT, Waltham, USA, (2007).

[50] Jones R.M.: *Mechanics of Composite Materials*, Second Edition, Taylor and Francis Group, New York, (1999).

[51] AMETEK Material Analysis Division: *Phantom Help File*, Vision Research, (2012).

[52] Personal communication, Dr. Cinzia Giacomuzzo.

[53] Personal communication, Alberto Campagnin.

[54] Francesconi A., Giacomuzzo C., Grande A.M., Mudric T., Zaccariotto M., Etemadi E., Di Landro L., Galvanetto U., ‘‘Comparison of self-healing ionomer to aluminium-alloy bumpers for protecting spacecraft equipment from space debris impacts’’, *Advances in Space Research*, vol. 51, pp. 930-940, (2013).

[55] Century Dynamics: *AUTODYN Theory manual*. Revision 4.3, Century Dynamics Int., Concord, USA, 2005.

[56] Anderson Jr C.E., ‘‘An overview of the theory of hydrocodes’’, *Int J of Imp Engng*, vol. 5, pp. 33-59, (1987).

[57] Lucy L.B., ‘‘A numerical approach to the testing of the fision hypothesis’’, *Astron J* , vol. 82, pp. 103-1024, (1977).

[58] Gingold R.A., Monaghan J.J., ‘‘Smoothed particle hydrodynamics’’, *Mon Not R Astron Soc*, vol. 181, pp. 375-389, (1977).

[59] Monaghan J.J., ‘‘Smoothed particle hydrodynamics’’, *Annu. Rev. Astron. Astrophys.*, vol. 30, pp. 543-574, (1992).

[60] Monaghan J.J., ‘‘Smoothed particle hydrodynamics and its diverse applications’’, *Annu. Rev. Fluid. Mech.*, vol. 44, pp. 323-346, (2012).

[61] Liu M.B., Liu G.R., ‘‘Smoothed particle hydrodynamics (SPH): an overview and recent developments’’, *Arch Comput Methods Eng*, vol. 17, pp. 25-76, (2010).

[62] Liu G.R., Liu M.B.: *Smoothed Particle Hydrodynamics: a meshfree particle method*, World Scientific Publishing Co. Pte. Ltd., Singapore, (2003).

[63] Von Neumann J., Richtmyer R.D., ‘‘A method for the numerical calculation of hydrodynamic shocks’’, *Journal of Applied Physics*, vol. 21, pp. 232-237, (1950).

[64] Century Dynamics: *AUTODYN Explicit Software for Nonlinear Dynamics: SPH User Manual & Tutorial*, Revision 4.3, Century Dynamics Inc., Concord, USA, 2005.

[65] Hiermaier S., Riedel W., Hayhurst C., Clegg R.A., Wentzel C. AMMHIS – advanced material models for hypervelocity impact simulations. Final report, EMI report. E 43/98, ESA CR(P) 4305, Freiburg; July 30, 1999.

[66] Century Dynamics: *AUTODYN Explicit Software for Nonlinear Dynamics: Composite Modelling in AUTODYN*, Revision 1.0, Century Dynamics Inc., Concord, USA, 2005.

[67] Anderson Jr Ch.E., Cox P.A., Johnson G.R., Maudlin P.J., ‘‘A constitutive formulation for anisotropic materials suitable for wave propagation computer programs - II’’, *Computational Mechanics*, vol. 15, pp. 201-223, (1994).

[68] Johnson G.R., Cook W.H. ‘‘A Constitutive Model and Data for Metals Subjected to Large Strains, High Strain Rates and High Temperatures’’. *Proceedings of the seventh international symposium on ballistics*, The Hague, Netherlands, (1983).

[69] Clegg R.A., White D.M., Riedel W., Harwick W., ‘‘Hypervelocity impact damage prediction in composites: Part I – material model and characterisation’’. *Int J of Imp Engng*, vol. 33, pp. 190-200, (2006).

[70] Ryan S., Wicklein M., Mouritz A., Riedel W., Schäfer F., Thoma K.. ‘‘Theoretical prediction of dynamic composite material properties for hypervelocity impact simulation’’. *Int J Impact Eng*, vol. 36, pp. 899-912, (2009).

[71] Huang Z.M., ‘‘A bridging model prediction of the ultimate strength of composite laminates subjected to biaxial loads’’, *Composite Science and Technology*, vol. 64, pp. 395-448, (2004).

[72] Zhou Y.X., Huang Z.M., ‘‘A bridging model prediction of the ultimate strength of composite laminates subjected to triaxial loads’’, *Journal of Composite Materials*, vol. 46, pp. 2343-2378, (2012).

[73] Chamis C.C., ‘‘Simplified composite micromechanics equations for strength, fracture toughness, impact resistance and environmental effects’’, *SAMPE Quart*, (1984).

[74] Daniel I.M., Ishai O.: *Engineering Mechanics of Composite Materials*, Oxsford University Press Inc., New York, (1994).

[75] Carter W.J. & Marsh S.P. ‘‘Hugoniot Equation of Polymers’’. Los Alamos National Laboratory, Los Alamos, NM, 1995.

[76] Grande A.M., Castelnovo L., Di Landro L., Giacomuzzo C., Francesconi A., Rahman, Md.A., “Rate dependent self-healing behavior of an ethylene-co-methacrylic acid ionomer under high energy impact conditions”, *Journal of Applied Polymer Science*, vol. 130, pp. 1949-1958, (2013).

[77] Steinberg D.J. ‘‘Equation of State and Strength Properties of Selected Materials’’. Report No. UCRL-MA-106439, Lawrence Livermore National Laboratory, Livermore, CA, (1991).

[78] Gupta N.K., Iqbal M.A., Sekhon G.S., ‘‘Experimental and numerical studies on the behavior of thin aluminum plates subjected to impact by blunt- and hemispherical-nosed projectiles’’. *Int J Impact Eng*, vol. 32, pp. 1921-44, (2006).

Appendix 1: MATLAB script file for the prediction of CFRP laminate stiffness properties and the corresponding input file

A script file written in MATLAB for the prediction of CFRP laminate stiffness properties and unidirectional lamina strength properties is given below.

```
clear all
disp(' ')
disp('--------------------------------------------------------------------')
disp(' This program calculates laminate properties')
disp(' from the properties of the constituent materials.')
disp(' ')
disp(' The x and y co-ordinates are in the plane of the composite')
disp(' and z is through the thickness.')
disp('--------------------------------------------------------------------')
disp(' ')
disp(' Select in which units the material properties will be displayed:')
disp(' 1=Pa ')
disp(' 2=kPa ')
disp(' 3=MPa ')
disp(' 4=GPa ')
disp(' ')
units_choice=input(' ');
disp(' ')
disp('--------------------------------------------------------------------')
disp(' ')
disp(' Enter the name of the text file containing the constituent ');
disp(' properties and data for the laminate (e.g. FileName.txt): ');
disp(' ')
file_name=input(' ','s');
diary_filename=['diary_',file_name];
if(exist(diary_filename)>0)
    delete(diary_filename)
end
diary(diary_filename)
disp(' ')
disp([' Loading file: ',file_name])
disp(' ')
disp('--------------------------------------------------------------------')
fid1=fopen(file_name,'r');
all_data_cell=textscan(fid1,'%f','CommentStyle','*');
all_data=[all_data_cell{1}];

% Fiber density
Rf=all_data(1);
% Fiber longitudinal tensile modulus (Ef1)
Ef11=all_data(2);
% Fiber transverse tensile modulus (Ef2)
Ef22=all_data(3);
% Fiber Poisson's ratio (v12)
vf12=all_data(4);
% Fiber transverse Poisson's ratio (v23)
vf23=all_data(5);
% Fiber shear modulus (Gf12)
Gf12=all_data(6);
% Fiber transverse shear modulus (Gf23)
```

```
Gf23=all_data(7);
% Fiber longitudinal tensile strength
Xft=all_data(8);
% Fiber longitudinal compression strength
Xfc=all_data(9);

% Resin density
Rm=all_data(10);
% Resin tensile modulus (Em)
Em=all_data(11);
% Resin Poisson's ratio (vm)
vm=all_data(12);
% Resin shear modulus (Gm)
Gm=all_data(13);
% Resin tensile strength
Xmt=all_data(14);
% Resin compression strength
Xmc=all_data(15);
% Resin shear strength
Smxy=all_data(16);
% Resin fracture energy
Gfm=all_data(17);

% LAMINATE DATA
% Fiber volume content
Vf=all_data(18);
% Resin volume content
Vm=1-Vf;
% Total number of laminas in the laminate
N=all_data(19);
% Total thickness of the laminate in meters
h=all_data(20);

% Vector containing the thickness of each lamina. The i-th vector element
% corresponds to the thickness of the i-th lamina.
for i=1:N;
    t(i)=all_data(20+i);
end

% Vector containing the angle of each lamina material directions with
% regards to the laminate principal material axes. The i-th vector element
% corresponds to the angle of the i-th lamina.
for i=1:N;
    theta(i)=all_data(20+N+i);
end

% Beta coefficient used for the calculation of the bridging matrix elements
% (0<=beta<=1, usually from 0.35 to 0.5)
beta=all_data(20+2*N+1);

% Alfa coefficient used for the calculation of the bridging matrix elements
% (0<=alfa<=1, usually from 0.35 to 0.5)
alfa=all_data(20+2*N+2);

% Assumed volume content of voids in the matrix of the laminate
Vv=all_data(20+2*N+3);

% p-wave sound speed of the laminate used for the calculation of the
% equation of state properties
cp=all_data(20+2*N+4);
```

```
% Elastic compliance matrix for the fiber material (valid only if the fiber
% is transversely isotropic)
Sf=[1/Ef11 -vf12/Ef11 -vf12/Ef11 0 0 0;...
    -vf12/Ef11 1/Ef22 -vf23/Ef22 0 0 0;...
    -vf12/Ef11 -vf23/Ef22 1/Ef22 0 0 0;...
    0 0 0 1/Gf23 0 0 ; 0 0 0 0 1/Gf12 0; 0 0 0 0 0 1/Gf12];

% Elastic compliance matrix of the resin material
Sm=[1/Em -vm/Em -vm/Em 0 0 0;...
    -vm/Em 1/Em -vm/Em 0 0 0;...
    -vm/Em -vm/Em 1/Em 0 0 0;...
    0 0 0 1/Gm 0 0; 0 0 0 0 1/Gm 0; 0 0 0 0 0 1/Gm];

% Calculating the bridging matrix elements
a11=Em/Ef11;
a22=beta+(1-beta)*Em/Ef22;
a33=a22;
a44=a22;
a55=alfa+(1-alfa)*Gm/Gf12;
a66=a55;
a32=0;

a13=((Sf(1,2)-Sm(1,2))*(a11-a22))/(Sf(1,1)-Sm(1,1));
a12=a13;

% Calculating the elastic properties of a lamina
E11=Vf*Ef11+Vm*Em;
v12=Vf*vf12+Vm*vm;
E22=((Vf+Vm*a11)*(Vf+Vm*a22))/((Vf+Vm*a11)*(Vf*Sf(2,2)+a22*Vm*Sm(2,2))+Vf*Vm*(Sm
(2,1)-Sf(2,1))*a12);
G12=(Vf+Vm*a66)/(Vf/Gf12+Vm*a66/Gm);
G12_2=((Vf+Vm*a66)*Gf12*Gm)/(Vf*Gm+Vm*a66*Gf12);
G13=G12;
G23=(0.5*(Vf+Vm*a44))/(Vf*(Sf(2,2)-Sf(2,3))+Vm*a44*(Sm(2,2)-Sm(2,3)));
v13=v12;
v23=((E22/(2*G23))-1);

% Lamina and laminate density
R0=Vf*Rf+Vm*Rm;

% Lamina properties
Ex=E11;
Ey=E22;
Ez=E22;
Vxy=v12;
Vyz=v23;
Vxz=v13;
Gxy=G12;
Gxz=G13;
Gyz=G23;

% Units

if (units_choice==1)
    units='Pa';
    units_tr=1;
end

if (units_choice==2)
    units='kPa';
    units_tr=0.001;
```

```
end

if (units_choice==3)
    units='MPa';
    units_tr=0.000001;
end

if (units_choice==4)
    units='GPa';
    units_tr=0.000000001;
end

% Calculating Poisson's coefficients
Vyx=(Ey/Ex)*Vxy;
Vzy=(Ez/Ey)*Vyz;
Vzx=(Ez/Ex)*Vxz;

% Calculating the volume fraction of each lamina in the laminate
for k=1:N;
    v(k)=(t(k))/h;
end

% Calculating the stiffness matrix coefficients of the lamina

delta=(1-Vxy*Vyx-Vyz*Vzy-Vzx*Vxz-2*Vyx*Vzy*Vxz)/(Ex*Ey*Ez);

c(1,1)=(1-Vyz*Vzy)/(Ey*Ez*delta);
c(1,2)=(Vyx+Vzx*Vyz)/(Ey*Ez*delta);
c(1,3)=(Vzx+Vyx*Vzy)/(Ey*Ez*delta);
c(1,4)=0;
c(1,5)=0;
c(1,6)=0;
c(2,1)=(Vyx+Vzx*Vyz)/(Ey*Ez*delta);
c(2,2)=(1-Vxz*Vzx)/(Ex*Ez*delta);
c(2,3)=(Vzy+Vxy*Vzx)/(Ex*Ez*delta);
c(2,4)=0;
c(2,5)=0;
c(2,6)=0;
c(3,1)=(Vzx+Vyx*Vzy)/(Ey*Ez*delta);
c(3,2)=(Vzy+Vxy*Vzx)/(Ex*Ez*delta);
c(3,3)=(1-Vxy*Vyx)/(Ex*Ey*delta);
c(3,4)=0;
c(3,5)=0;
c(3,6)=0;
c(4,1)=0;
c(4,2)=0;
c(4,3)=0;
c(4,4)=Gyz;
c(4,5)=0;
c(4,6)=0;
c(5,1)=0;
c(5,2)=0;
c(5,3)=0;
c(5,4)=0;
c(5,5)=Gxz;
c(5,6)=0;
c(6,1)=0;
c(6,2)=0;
c(6,3)=0;
c(6,4)=0;
c(6,5)=0;
```

```
c(6,6)=Gxy;

% Calculating the transformation matrix T for each lamina
for k=1:N;
    T(1,1,k)=(cosd(theta(k)))^2;
    T(1,2,k)=(sind(theta(k)))^2;
    T(1,3,k)=0;
    T(1,4,k)=0;
    T(1,5,k)=0;
    T(1,6,k)=sind(2*(theta(k)));
    T(2,1,k)=(sind(theta(k)))^2;
    T(2,2,k)=(cosd(theta(k)))^2;
    T(2,3,k)=0;
    T(2,4,k)=0;
    T(2,5,k)=0;
    T(2,6,k)=-(sind(2*(theta(k))));
    T(3,1,k)=0;
    T(3,2,k)=0;
    T(3,3,k)=1;
    T(3,4,k)=0;
    T(3,5,k)=0;
    T(3,6,k)=0;
    T(4,1,k)=0;
    T(4,2,k)=0;
    T(4,3,k)=0;
    T(4,4,k)=cosd(theta(k));
    T(4,5,k)=-(sind(theta(k)));
    T(4,6,k)=0;
    T(5,1,k)=0;
    T(5,2,k)=0;
    T(5,3,k)=0;
    T(5,4,k)=sind(theta(k));
    T(5,5,k)=cosd(theta(k));
    T(5,6,k)=0;
    T(6,1,k)=-(sind(2*(theta(k))))/2;
    T(6,2,k)=sind(2*(theta(k)))/2;
    T(6,3,k)=0;
    T(6,4,k)=0;
    T(6,5,k)=0;
    T(6,6,k)=cosd(2*(theta(k)));
end

% Transforming each lamina stiffness matrix in the laminate material axes
for k=1:N;
    ct(:,:,k)=(inv(T(:,:,k)))*c(:,:)*((inv(T(:,:,k)))');
end

% CALCULATING LAMINATE PROPERTIES FROM UNI-DIRECTIONAL DATA

% - calculating a(k)
for k=1:N;
    a(k)=ct(4,4,k)*ct(5,5,k)-((ct(4,5,k))^2);
end

% - calculating A
for k=1:N;
    A1(k)=(v(k)*ct(4,4,k))/(a(k));
    A2(k)=(v(k)*ct(5,5,k))/(a(k));
    A3(k)=(v(k)*ct(4,5,k))/(a(k));
end

A1s=sum(A1);
```

```
A2s=sum(A2);
A3s=sum(A3);

A=A1s*A2s-(A3s*A3s);

% - calculating the stiffness matrix coefficients of the laminate

% - calculating C33
for k=1:N;
    C33_1(k)=v(k)/ct(3,3,k);
end

C33_1s=sum(C33_1);

C(3,3)=1/(C33_1s);

% - calculating C23
for k=1:N;
    C23_1(k)=v(k)*ct(2,3,k);
    C23_2(k)=((ct(3,3,k)-C(3,3))*v(k)*(ct(2,3,1)-ct(2,3,k)))/(ct(3,3,k));
end

C23_1s=sum(C23_1);
C23_2s=sum(C23_2);

C(2,3)=C23_1s+C23_2s;

% - calculating C22
for k=1:N;
    C22_1(k)=v(k)*ct(2,2,k);
    C22_2(k)=((ct(2,3,k)-C(2,3))*v(k)*(ct(2,3,1)-ct(2,3,k)))/(ct(3,3,k));
end

C22_1s=sum(C22_1);
C22_2s=sum(C22_2);

C(2,2)=C22_1s+C22_2s;

% - calculating C13
for k=1:N;
    C13_1(k)=v(k)*ct(1,3,k);
    C13_2(k)=((ct(3,3,k)-C(3,3))*v(k)*(ct(1,3,1)-ct(1,3,k)))/(ct(3,3,k));
end

C13_1s=sum(C13_1);
C13_2s=sum(C13_2);

C(1,3)=C13_1s+C13_2s;

% - calculating C12
for k=1:N;
    C12_1(k)=v(k)*ct(1,2,k);
    C12_2(k)=((ct(1,3,k)-C(1,3))*v(k)*(ct(2,3,1)-ct(2,3,k)))/(ct(3,3,k));
end

C12_1s=sum(C12_1);
C12_2s=sum(C12_2);

C(1,2)=C12_1s+C12_2s;
```

```
% - calculating C11
for k=1:N;
    C11_1(k)=v(k)*ct(1,1,k);
    C11_2(k)=((ct(1,3,k)-C(1,3))*v(k)*(ct(1,3,1)-ct(1,3,k)))/(ct(3,3,k));
end

C11_1s=sum(C11_1);
C11_2s=sum(C11_2);

C(1,1)=C11_1s+C11_2s;

% - calculating C16
for k=1:N;
    C16_1(k)=v(k)*ct(1,6,k);
    C16_2(k)=((ct(1,3,k)-C(1,3))*v(k)*(ct(3,6,1)-ct(3,6,k)))/(ct(3,3,k));
end

C16_1s=sum(C16_1);
C16_2s=sum(C16_2);

C(1,6)=C16_1s+C16_2s;

% - calculating C26
for k=1:N;
    C26_1(k)=v(k)*ct(2,6,k);
    C26_2(k)=((ct(2,3,k)-C(2,3))*v(k)*(ct(3,6,1)-ct(3,6,k)))/(ct(3,3,k));
end

C26_1s=sum(C26_1);
C26_2s=sum(C26_2);

C(2,6)=C26_1s+C26_2s;

% - calculating C36
for k=1:N;
    C36_1(k)=v(k)*ct(3,6,k);
    C36_2(k)=((ct(3,3,k)-C(3,3))*v(k)*(ct(3,6,1)-ct(3,6,k)))/(ct(3,3,k));
end

C36_1s=sum(C36_1);
C36_2s=sum(C36_2);

C(3,6)=C36_1s+C36_2s;

% - calculating C66
for k=1:N;
    C66_1(k)=v(k)*ct(6,6,k);
    C66_2(k)=((ct(3,6,k)-C(3,6))*v(k)*(ct(3,6,1)-ct(3,6,k)))/(ct(3,3,k));
end

C66_1s=sum(C66_1);
C66_2s=sum(C66_2);

C(6,6)=C66_1s+C66_2s;

% - calculating C44
for k=1:N;
    C44_1(k)=(v(k)*ct(4,4,k))/(a(k));
```

```
end

C44_1s=sum(C44_1);

C(4,4)=C44_1s/A;

% - calculating C45
for k=1:N;
    C45_1(k)=(v(k)*ct(4,5,k))/(a(k));
end

C45_1s=sum(C45_1);

C(4,5)=C45_1s/A;

% - calculating C55
for k=1:N;
    C55_1(k)=(v(k)*ct(5,5,k))/(a(k));
end

C55_1s=sum(C55_1);

C(5,5)=C55_1s/A;

% - calculating C21
C(2,1)=C(1,2);

% - calculating C31
C(3,1)=C(1,3);

% - calculating C32
C(3,2)=C(2,3);

% - calculating C54
C(5,4)=C(4,5);

% - calculating C61
C(6,1)=C(1,6);

% - calculating C62
C(6,2)=C(2,6);

% - calculating C63
C(6,3)=C(3,6);


% Laminate stiffness matrix
CL=C;

% Calculating the effective compliance matrix of the laminate
SL=inv(CL);

% Claculating the effective elastic properties of the laminate
ELxx=1/(SL(1,1));
ELyy=1/(SL(2,2));
ELzz=1/(SL(3,3));
VLyz=-((SL(2,3))/(SL(2,2)));
VLxz=-((SL(3,1))/(SL(1,1)));
VLxy=-((SL(2,1))/(SL(1,1)));
```

```
GLyz=1/(SL(4,4));
GLxz=1/(SL(5,5));
GLxy=1/(SL(6,6));

VLzx=VLxz*(ELzz/ELxx);

% Writing the stiffness properties data to the command window

str1=sprintf('  Exx (%s) = %f ', units, ELxx*units_tr);
str2=sprintf('  Eyy (%s) = %f ', units, ELyy*units_tr);
str3=sprintf('  Ezz (%s) = %f ', units, ELzz*units_tr);
str4=sprintf('  Vyz       = %f ', VLyz);
str5=sprintf('  Vxz       = %f ', VLxz);
str6=sprintf('  Vxy       = %f ', VLxy);
str7=sprintf('  Gyz (%s) = %f ', units, GLyz*units_tr);
str8=sprintf('  Gxz (%s) = %f ', units, GLxz*units_tr);
str9=sprintf('  Gxy (%s) = %f ', units, GLxy*units_tr);
str51=sprintf('  Vzx       = %f ', VLzx);

str11=sprintf('  E11 (%s) = %f ', units, Ex*units_tr);
str22=sprintf('  E22 (%s) = %f ', units, Ey*units_tr);
str33=sprintf('  E33 (%s) = %f ', units, Ez*units_tr);
str44=sprintf('  V23       = %f ', Vyz);
str55=sprintf('  V13       = %f ', Vxz);
str66=sprintf('  V12       = %f ', Vxy);
str77=sprintf('  G23 (%s) = %f ', units, Gyz*units_tr);
str88=sprintf('  G13 (%s) = %f ', units, Gxz*units_tr);
str99=sprintf('  G12 (%s) = %f ', units, Gxy*units_tr);

str_density=sprintf(' Laminate reference density (kg/m^3): %f ', R0);

disp(' ')
disp(' Uni-directional lamina stiffness properties')
disp(' ')
disp(str11)
disp(str22)
disp(str33)
disp(str44)
disp(str55)
disp(str66)
disp(str77)
disp(str88)
disp(str99)
disp(' ')
disp('-------------------------------------------------------------------')
disp(' ')
disp(' Laminate stiffness properties')
disp(' ')
disp(str1)
disp(str2)
disp(str3)
disp(str4)
disp(str5)
disp(str6)
disp(str7)
disp(str8)
disp(str9)
disp(' ')
disp(str51)
disp(' ')
disp('-------------------------------------------------------------------')
```

```
disp(' ')
disp(str_density)
disp(' ')
disp('-------------------------------------------------------------------')

% EQUATION OF STATE PROPERTIES OF THE LAMINATE

%delta=(1-nu12*nu21-nu23*nu32-nu31*nu13-2*nu21*nu32*nu13)/(E1*E2*E3);

VLyx=(ELyy/ELxx)*VLxy;
VLzy=(ELzz/ELyy)*VLyz;

delta_laminate=(1-VLxy*VLyx-VLyz*VLzy-VLzx*VLxz-
2*VLyx*VLzy*VLxz)/(ELxx*ELyy*ELzz);

C11=(1-VLyz*VLzy)/(ELyy*ELzz*delta_laminate);
stiff_matrix_laminate=CL(1,1);

A1=(1/9)*(CL(1,1)+CL(2,2)+CL(3,3)+2*(CL(1,2)+CL(2,3)+CL(1,3)));

C0=0.6707*cp;

S=0.0006242*cp;

K1_1=R0*C0*C0;
A2=R0*C0*C0*(1+S*(S-1));
A3=R0*C0*C0*(2*(S-1)+3*(S-1)*(S-1));

B0=2*S-1;
B1=B0;

T1=A1;
T2=A2;

str_A1=sprintf('  A1 (%s) = %f ', units, A1*units_tr);
str_A2=sprintf('  A2 (%s) = %f ', units, A2*units_tr);
str_A3=sprintf('  A3 (%s) = %f ', units, A3*units_tr);
str_B0=sprintf('  B0       = %f ', B0);
str_B1=sprintf('  B1       = %f ', B1);
str_T1=sprintf('  T1 (%s) = %f ', units, T1*units_tr);
str_T2=sprintf('  T2 (%s) = %f ', units, T2*units_tr);

disp(' ')
disp(' Estimated equation of state properties for the laminate')
disp(' ')
disp(str_A1)
disp(str_A2)
disp(str_A3)
disp(str_B0)
disp(str_B1)
disp(str_T1)
disp(str_T2)
disp(' ')
disp('-------------------------------------------------------------------')

% Calculating the in-plane strength properties of a single unidirectional lamina

% Longitudinal tension strength
Xt=Vf*Xft;
% Lamina transverse tension strength
```

```
S22t=(1-(sqrt(Vf)-Vf)*(1-Em/Ef22))*Xmt;
% Lamina transverse compression strength
S22c=(1-(sqrt(Vf)-Vf)*(1-Em/Ef22))*Xmc;
% Intralaminar shear strength
S12s=(1-(sqrt(Vf)-Vf)*(1-Gm/Gf12))*Smxy;
% Longitudinal compression strength
Xc_1=Vf*Xfc;  % Fiber compression
Xc_2=10*S12s+2.5*Xmt;  % Delamination/shear
Xc_3=Gm/(1-Vf*(1-Gm/Gf12));  % Microbuckling

Xc_all=[Xc_1 Xc_2 Xc_3];

Xc=min(Xc_all); % Longitudinal compression strength

% Matrix properties if voids presence is assumed
% Matrix transverse tensile strength if voids presence is assumed
Xmt_voids=(1-sqrt(4*Vv/((1-Vf)*pi)))*Xmt;
% Matrix transverse compressive strength if voids presence is assumed
Xmc_voids=(1-sqrt(4*Vv/((1-Vf)*pi)))*Xmc;
% Matrix shear strength if voids presence is assumed
Smxy_voids=(1-sqrt(4*Vv/((1-Vf)*pi)))*Smxy;

% Calculating certain strength properties of a single lamina if voids
% presence is assumed
S22t_voids=(1-(sqrt(Vf)-Vf)*(1-Em/Ef22))*Xmt_voids;
S22c_voids=(1-(sqrt(Vf)-Vf)*(1-Em/Ef22))*Xmc_voids;
S12s_voids=(1-(sqrt(Vf)-Vf)*(1-Gm/Gf12))*Smxy_voids;
% Longitudinal compression strength (delamination/shear) if voids are
% present
Xc_2_voids=10*S12s_voids+2.5*Xmt_voids;


% Calculating through-the-thickness strengths of a lamina

% Interlaminar shear strengths of unidirectional laminate
S13s=(1-(sqrt(Vf)-Vf)*(1-Gm/Gf12))*Smxy;  % Longitudinal
S23s=((1-(sqrt(Vf))*(1-Gm/Gf23))/(1-Vf*(1-Gm/Gf23)))*Smxy;  % Transverse

% Interlaminar shear strengths of unidirectional laminate if void presence
% is assumed
S13s_voids=(1-(sqrt(Vf)-Vf)*(1-Gm/Gf12))*Smxy_voids;  % Longitudinal
S23s_voids=((1-(sqrt(Vf))*(1-Gm/Gf23))/(1-Vf*(1-Gm/Gf23)))*Smxy_voids; %Transverse

diary off
```

The input file for the above script file is given next.

```
*-----------------------------------------------------------------------
*All data shoud be in koligrams (kg), meters (m) and seconds (s)
*-----------------------------------------------------------------------

*CONSTITUENT PROPERTIES AND DATA FOR THE LAMINATE

*Constituent properties

*Fiber properties
*Fibre type: T600
*Density (kg/m^3):
1790
*Longitudinal tensile modulus (Ef11):
```

```
230000000000
*Transverse tensile modulus (Ef22):
15000000000
*Poisson's ratio (vf12):
0.2
*Transverse Poisson's ratio (vf23):
0.0714
*Shear modulus (Gf12):
15000000000
*Transverse shear modulus (Gf23):
7000000000
*Longitudinal tensile strength (Xft):
4136400000
*Longitudinal compression strength (Xfc):
3000000000

*Resin
*Matrix name: REM
*Density (kg/m^3):
1200
*Tensile modulus (Em):
3360000000
*Poisson's ratio (vm):
0.35
*Shear modulus (Gm):
1244000000
*Tensile strength (Xmt):
60000000
*Compression strength (Xmc):
150000000
*Shear strength (Smxy):
55000000
*Fracture energy - Gfm (J/m^2):
240

*Laminate data
*Fibre volume content:
0.6
*Number of laminas in the laminate:
12
*Thickness of the laminate in meters:
0.0036
*Thickness of each lamina individually in milimeters, e.g.:
*t(1)
*t(2)
*...
*t(n)
*where t(i) is the thickness of the i-th lamina:
0.0003
0.0003
0.0003
0.0003
0.0003
0.0003
0.0003
0.0003
0.0003
0.0003
0.0003
0.0003
```

```
*Angle of each lamina material directions with regards to the laminate principal
*material axes (e.g. theta(1) theta(2) ... theta(n), where theta(i) is the angle
*of the i-th lamina in degrees):
0
90
0
90
0
90
90
0
90
0
90
0
*Value of the beta coefficient that is used for the calculation of the bridging
matrix elements (usually from 0.35 to 0.5):
0.35
*Value of the alfa coefficient that is used for the calculation of the bridging
matrix elements (usually from 0.35 to 0.5):
0.3
*Assumed volume content of voids in the matrix of the composite laminate (if no
voids are present write zero (0))
0.00
*p-wave sound speed of the laminate
3050
```